# Cavity-enhanced direct frequency comb spectroscopy

by

**Michael J. Thorpe**

B.S., Western Washington University, 2001

A thesis submitted to the

Faculty of the Graduate School of the

University of Colorado in partial fulfillment

of the requirements for the degree of

Doctor of Philosophy

Department of Physics

2009

This thesis entitled:
Cavity-enhanced direct frequency comb spectroscopy
written by Michael J. Thorpe
has been approved for the Department of Physics

_____

Jun Ye

_____

Eric A. Cornell

Date _____

The final copy of this thesis has been examined by the signatories, and we find that both the content and the form meet acceptable presentation standards of scholarly work in the above mentioned discipline.

Thorpe, Michael J. (Ph.D., Physics)

Cavity-enhanced direct frequency comb spectroscopy

Thesis directed by Professor Adjoint Jun Ye

Cavity-enhanced direct frequency comb spectroscopy (CE-DFCS) combines broad spectral bandwidth, high spectral resolution, precise frequency calibration, and ultra-high detection sensitivity, all in one experimental platform based on an optical frequency comb interacting with a high-finesse optical cavity. Precise control of the optical frequency comb allows highly efficient, coherent coupling of individual comb components with corresponding resonant modes of the high-finesse cavity. The use of low dispersion mirrors permits almost the entire spectral bandwidth of the frequency comb to be employed for detection, covering a range of $> 10\%$ of the actual optical frequency. The long cavity lifetime dramatically enhances the effective interaction between the light field and intra-cavity matter, increasing the sensitivity for measurement of optical losses by a factor that is on the order of the cavity finesse. Finally, the light transmitted from the cavity is spectrally resolved to provide a multitude of detection channels with spectral resolutions ranging from several gigahertz to hundreds of kilohertz.

We begin with a discussion of the principles of cavity-enhanced direct frequency comb spectroscopy including the properties of frequency combs and optical cavities that are relevant to CE-DFCS systems. Methods for characterizing cavity-comb interactions and achieving simultaneous broad bandwidth and high resolution detection of the cavity transmitted beam are discussed. Measurements are presented that fully characterize the detection sensitivity, resolution, and spectral coverage of several CE-DFCS systems. We also outline several types of UV, optical, and IR frequency comb sources and optical cavity designs that can be

used for specific spectroscopic applications. Finally, we present a series of experimental measurements on trace gas detections, human breath analysis, and characterization of cold molecular beams. These results demonstrate clearly that the wide bandwidth and ultrasensitive nature of the femtosecond enhancement cavity enables powerful real-time detection and identification of many molecular species including their quantum state distributions in a massively parallel fashion.

**Dedication**

To my parents and grandparents who always emphasized

the importance of education.

For Mariah Palmer, the love of my life.

## Acknowledgements

If you would have asked me at the beginning of my freshman year of college,"where will you be in 12 years?", I think that "preparing to defend a PhD thesis in physics," would have been an unlikely answer. When I entered Western Washington University in the fall of 1996, I was very interested in philosophy and under the impression that philosophers were somehow the best suited to tackle the complicated problems facing society. However, after my first quarter of philosophy classes, I found myself dissatisfied with the process of formulating arguments about topics that clearly had no definitive answer. I also sensed that philosophers purposely avoided topics where answers could be reached because such questions had already been, or would likely be, answered by the various fields of science. It was this thinking that led me to enroll in my first physics class freshman year. I was immediately impressed by the rigorous development of the topics of physics, and how a few well constructed fundamental principles could describe such a wide variety of phenomena. Needless to say, I was hooked!

During my time at Western, I had many instructors to whom I'm greatly indebted. Most notably were Richard Atneosen and Brad Johnson. Over the course of several optics, lasers, and holography courses, Rich Atneosen helped me develop a love for the field of optics that remains at the heart of my research interests today. Brad Johnson provided me with my first glimpses of the incredible breadth, complexity and beauty of physics. His courses on quantum mechanics,

solids, and general relativity always left me dreaming about the solutions to great problems.

After my undergraduate studies I had the pleasure of experiencing the commercial world for the first time as a technician working for a small optics start-up company called Orca Photonic Systems. The company had nine employees, most of which held masters degrees or higher, and two of the three founders received their PhD's from JILA. A bit of foreshadowing I guess! At Orca, I learned a great deal of practical skills that are essential in any technical pursuit, academic or commercial. Steve Moody and Doug Donaldson taught me about circuit design. Matt Moore patiently helped me learn the basics of computer programming. Dave Cunningham taught me how to design optical systems and more importantly, how to troubleshoot them. Finally, Bill Pence introduced me to the art of machining, a skill that has been incredibly useful for designing experiments throughout my PhD studies. After a couple of years at Orca, their guidance also helped me realize that I wanted to pursue a PhD in physics.

During college and my time at Orca, my love for physics was always slightly overshadowed by my love of the outdoors, in particular the mountains, skiing, and climbing. So when it was time to apply for graduate school, the University of Colorado was on a short list of schools that could satisfy both my interest in physics and my love of the outdoors. At the time, I wasn't aware that CU had a tendency to attract outdoor enthusiasts. However, after arriving, I quickly realized that many of the students shared my motivation for choosing CU. Over the course of the last five years I was privileged to spend so many weekends with great friends like Dave Hume, Paul Parazzoli, Ben Egbers, Chris Ticknor, Patrick Maletinski, David James, Darren Hudson, Eric Hudson, Jason Brietbarth, Paul Kuntz, Ron Pepino, and Evan Salim, climbing, skiing, biking, rafting, and hiking in the outdoor playgrounds of Colorado. These times were essential for rejuvenat-

ing my spirits and recharging my interest and curiosity for the next week in the lab. Since most of these guys are also physicists, we spent much of these times discussing physics ideas and experiments, which only heightened the outdoor experience.

I think that I was blessed with good timing when I applied to the graduate program at CU. In the spring of 2003, the Optical Science and Engineering Program, started by Dana Anderson, was still young and growing rapidly. This education program, funded by NSF/IGERT, was designed to train physics, chemistry, and engineering graduate students in the field of optics. It was the perfect opportunity for a student with my background to secure funding for my PhD studies. I attribute a large portion of my success at CU to having received an OSEP fellowship. In particular, I think Jun's decision to hire me was in large part due to my OSEP funding. I still remember the day that I asked Jun if I could work in his lab. I could tell that he was reluctant, and since I didn't have a research background to speak of, I could offer no good reason why he should hire me. In the end he agreed to give me a chance, and I set out to prove to him that he made the right choice. I hope that, over the course of the last five years, I have succeeded in that goal. Jun has truly been an incredible advisor. He has taught me how to be an experimental physicist, and has given me extraordinary opportunities to explore my own creativity that will certainly prove invaluable in my future endeavors.

It has been a great pleasure working in Jun's lab. The atmosphere is one of hard work, ingenuity, and collaboration. I am especially grateful to Kevin Moll, Thomas Schibli, Jan Hall, Matt Stowe, Jason Jones, and Eric Hudson for their sage-like advice and undying willingness to help me find answers to my questions. I'm also indebted to the many people who helped develop the cavity-enhanced frequency comb spectroscopy project: Kevin Moll, Jason Jones, David Balslev-

Clausen, Darren Hudson, Ben Safdi, Matt Kirchner, Kevin Cossel, and Florian Adler. Probably the best aspect of Jun's lab is that there is such a wide variety of different experiments being conducted in such a small lab space. The result is that the collective Ye labs team has a huge amount of technical expertise covering a wide range of topics. If you have a question, chances are that someone within 50 feet of you knows the answer. Aside from the scientific resource, the ability to learn about, and track the progress of, so many different experiments was a great experience. Fortunately people like Thomas Schibli, Brian Sawyer, Seth Foreman, Marty Boyd, Dylan Yost, Matt Stowe, Gretchen Campbell, Sebastian Blatt, and Dajun Wang were consistently willing to spend time telling me about their experiments.

The high quality of the experiments at JILA is in large part due to the excellent technical support staff. I'd like to thank Terry Brown, James Fung-a-Fat, Mike Whitmore, Carl Sauer, and Dave Tegart for their help with the many custom electronics used in my experiments. Also, thanks to Blaine Horner, Tom Foote, Todd Asnicar, Hans Greene, and David Alchenberger for their help with the mechanical design and fabrication of experimental components. Finally, the people in computing department, the scientific reports office, and the many administrative staff members all contributed to making my time at JILA both productive and rewarding.

Of course, nothing good gets done at work without a whole bunch of support at home. I am fortunate that I have inherited a strong work ethic and sense of integrity that was first shown to me by my parents Jim and Brenda. During my time growing up in Idaho they not only taught me how to carry my own weight in society, but they also provided me with endless opportunities to explore all of the richness that life has to offer. I can't begin to express how grateful I am for their love and support. Similarly, my grandparents, Ruth, Cecil, Evelyn, and Bill

always took a very active role in my life and I deeply appreciate all they have given me. While I've been consumed with school for the last five years, it has been a pleasure to watch my sister, Heather, start a family of her own. I hope to soon follow in her footsteps. Finally, it was especially nice to have relatives in the Boulder area during graduate school. A big thanks to John and Marsha for all of the great meals and good times.

Over the years, many of my friends have helped me find my course in life. The most notable influence came from Seth Rigles. During my high school years, Seth helped me develop virtues such as patience and critical curiosity that have served me well to this day. I deeply appreciate the time we spent discussing issues and forming our adult perspectives of the world. I am also grateful for the freindship of Ben Egbers. By chance and good fortune, our paths have kept us in close contact over the past decade. Ben's good nature and easy going temperament always remind me to try and be a better person.

Finally, I'd like to thank my lovely fiancée Mariah Palmer for her unwavering love, support, patience, and encouragement. Her many great qualities are everything that I could hope for in a life partner. I am so excited about our future together.

## Contents

**Chapter**

# Tables

**Table**

## Figures

**Figure**

# Chapter 1

# Introduction

## 1.1 Spectroscopy before the laser

It has been known for more than one hundred years that electromagnetic radiation is an excellent vehicle for studying the properties of matter. Already in the early 1800s scientists such as Wollaston and Fraunhofer were observing dark lines in the spectrum of light emitted from the sun that led future generations of scientist to determine the composition of the Sun's gaseous outer layers. Fraunhofer's invention of the grating spectrograph, in 1814, allowed for precise wavelength measurements of optical absorption and emission spectra with accuracies of up to seven significant digits. By the second half of the $19^{th}$ century, many scientists were using this device to record the spectra of several atomic vapors, providing our first glimpses of atomic structure. This spectral data was studied extensively by Johannes Rydberg who, in 1888, presented an empirical formula for describing the frequencies of spectral lines of alkali atoms

$$\frac{\nu}{c} = \frac{1}{\lambda_{vac}} = Z^2 R\left(\frac{1}{n_1^2} - \frac{1}{n_2^2}\right). \tag{1.1}$$

Here, $c$ is the speed of light, $\lambda_{vac}$ is the vacuum wavelength of light, $Z$ is the atomic number of the element under study, $R$ is the Rydberg constant for that element, and $n_1$ and $n_2$ are integers where $n_1 < n_2$. In 1913, Niels Bohr used Rydberg's discovery that the frequencies of spectral lines could be described by

the difference of two quantities to formulate a quantum theory of the hydrogen atom. Perhaps the most important aspect of Bohr's work was his postulate that the frequencies of atomic of spectral lines arose for transitions between discrete electronic energy levels. This idea paved the way for modern quantum theory.

The development of modern quantum mechanics in the 1920s, by Schrodinger, Heisenberg, and others, provided a theoretical framework for understanding and predicting the frequencies of light absorbed and emitted by atoms and molecules based on their internal energy level structure. During this time, spectroscopic observations played a crucial role in the development of the theory. The observation of the doublet fine structure in hydrogen led to the incorporation of relativistic effects in atomic structure and the discovery of the electron spin. Pauli's famous exclusion principle stemmed from his observation of many atomic spectra which indicated that no two electrons could occupy the same state. Also, the observation of atomic hyperfine structure led Pauli to postulate that the nucleus had a small magnetic moment. The spectral observations of Stark and Zeeman provided a framework for understanding how atomic energy levels are affected by external electric and magnetic fields. Also, during this time, the work of C. V. Raman led to the discovery of inelastic scattering in molecules resulting in a powerful mechanism for the study of molecular vibrational and rotational structure. The theoretical framework of quantum mechanics combined with the increased precision of spectroscopic measurement, enabled by the ingenuity of spectrometer developers such as Fabry and Perot, led to an enormous growth in our understanding of atomic and molecular structure in the first half of the $20^{th}$ century.

## 1.2 The invention and development of laser spectroscopy

With the invention of the laser in 1960, the field of spectroscopy was revolutionized. Atomic and molecular absorption lines could be probed with precision light sources characterized by high spectral brightness and precisely defined wavelengths. The invention of the dye laser, in 1966, provided a tunable, coherent light source that enabled access to a wide variety atomic and molecular transitions covering large spectral windows. New techniques were invented that dramatically improved the resolution and control of the light-matter interactions in spectroscopic measurements. For example, saturation absorption spectroscopy led to improved resolution and allowed the measurement of energy levels that had previously been obscured by Doppler broadening such as the Hydrogen Lamb shift [1]. The development of laser cooling increased the resolution even further by suppressing many transition broadening effects such as first and second order Doppler shifts as well as transit time broadening [2]. Methods developed for frequency stabilizing lasers led to increased the precision of spectroscopic measurements and the control of light-matter interactions [3] [4]. Finally, external optical cavities were implemented to enhance the signals from weak or dilute resonant absorbers [5][6]. During this string of advances in spectroscopic techniques, a wide variety of laser sources were developed including tunable solid-states lasers, tunable diode lasers, and mode-locked lasers each with unique capabilities that have contributed to the rapid growth of laser spectroscopy.

## 1.3 Modern laser spectroscopy

Today, the breadth and sophistication of the field laser spectroscopy is truly amazing. In the physics community alone, laser spectroscopy is currently enabling

a large number of experiments that are at the forefront of scientific investigation. Examples include: the creation and study of new forms of matter such as Bose-Einstein condensates and degenerate Fermi gases [7], the measurement of the Lamb shift as high precision test of quantum electrodynamics [8], the search for permanent electric dipole moments and the variation of fundamental constants for table-top tests of the standard model [9], and the exploration of entanglement as a resource for quantum information processing and quantum computing [10]. In chemistry, biology, and environmental sciences, lasers spectroscopy has been used to study to structure and properties of a huge variety of molecules ranging from the small few-atom-molecules to large macro molecules. Through these studies, modern society has developed a broad understanding of biological processes, medical treatments, atmospheric chemistry, and chemical engineering processes for industrial applications.

In the commercial world, use of laser spectroscopy is less widespread; however, the number and scope of these applications is rapidly increasing. Already, combustion spectroscopy is used for optimizing the efficiency of fossil fuel power stations and car engines. The 'dosage' of anesthetics administered during surgery can be controlled by real-time monitoring of the ratios of $C0_2$, $O_2$ and $N_2$ exhaled by the patient using Raman spectroscopy [11]. Also, the detection of trace concentrations of molecules has emerged as a powerful tool in a wide range of commercial and industrial settings. Applications include: the detection of contaminants for semiconductor processing [12], human breath analysis for disease detection [13], air quality monitoring [14], and detection of biologically hazardous or explosive materials for security purposes [15]. Each of these applications has been facilitated by the development of new laser sources to access spectral domains of interest, combined with cavity enhancement techniques for increased detection sensitivity. For example, the advent of tunable laser diodes has led to sensitive measurements

of impurity levels in gases such as phosphine used in semiconductor productions [12] and for monitoring ethylene in fruit storage facilities [16]. Subsequently, quantum cascade lasers and optical parametric oscillators operating in the mid-infrared have been applied to human breath analysis for health screening and optical detection of explosives [17] [15]. These innovations represent remarkable advances in our capability to monitor and understand our environment. However, these technologies are currently based on single frequency laser sources that operate in relatively narrow spectral regions and thus the number of different molecules that can be studied or detected with a single system is very small. This severely limits our capability of performing surveyance on a global scale in real time.

## 1.4 The advent of the optical frequency comb

In the late 1990s, the previously disparate fields of mode-locked ultra-fast lasers and precision laser stabilization were merged with the invention of the optical frequency comb [18][19]. By controlling the phase and repetition rate of femtosecond pulses emitted from a mode-locked laser, the frequency spectrum corresponding to the pulse train is comprised of a well defined set of regularly spaced frequencies

$$\nu_n = nf_r + f_o, \tag{1.2}$$

where $n$ is the mode number, $f_r$ is the rate that pulses are emitted from the laser, and $f_o$ is the rate that the phase of the laser evolves with respect to the center of the pulse envelope. The key to producing the well defined set of frequencies in Eq. 1.2 was the measurement of $f_o$. While $f_r$ could easily be measured using a fast photodiode, measuring $f_o$ required the use of nonlinear interferometry [18]. When both $f_r$ and $f_o$ are measured, servos acting on the mode-locked laser cavity

length and dispersion can be used to stabilize the comb frequencies.

The potential applications of the optical frequency comb are considerable. The first, and so far most developed, application is optical frequency metrology [20][21][22]. Before the optical frequency comb, long chains of nonlinear frequency up-conversion were used to provide a coherent link between a microwave frequency, which could be counted by conventional electronics, and the optical frequency that was being measured [23]. Due to the large size, complexity, and limited utility of the frequency chains, only a few of these devices were constructed.

The first demonstration of optical frequency metrology using mode-locked lasers measured the difference between a well known optical frequency (the $4^{th}$ harmonic of a methane stabilized HeNe laser) and ones that were not well known (the D1 lines of cesium) [24]. Because the difference frequency of two comb modes does not depend on $f_o$, only the laser $f_r$ needed to be stabilized for these measurements. After the development of $f_o$ stabilization, the absolute frequency of any laser could be measured by its heterodyne beat with the nearest comb tooth

$$\nu_{CW} = \nu_m + f_{beat}, \tag{1.3}$$

Here, $m$ is the mode number of the nearest comb tooth to the CW laser frequency. Frequency-comb-based optical frequency metrology has lead to an explosion in the field of optical atomic clocks and optical frequency standards [25] [26][27]. Already, optical atomic clockes have enabled some of the highest precision measurements fundamental constant variations and the coupling of the gravitational potential to fundamental constants [28] [29].

Other applications of the optical frequency comb are less developed, but offer equally exciting prospects for the role of frequencies combs in the future of laser-based technologies [30]. Many of these applications require control over the amplitude and phase of individual comb components over broad spectral regions.

For instance, line-by-line pulse shaping can be used to generate arbitrary optical waveforms with the potential for dramatic advances in spread-spectrum lightwave communications, laser ranging and detection, and optical signal processing [31]. Another application is the coherent control of the quantum states of cold atomic and molecular samples [32]. Phase and amplitude control of the comb has already been used to control quantum interference and quantum state populations in atoms [32]. This same approach should also allow precise control of photoassociation and chemical reactions [33]. Finally, precise control of the phase of few-cycle mode-locked lasers has already enabled control of ultra-fast processes such as electron dynamics in atoms and molecules [34]. As a result, it is now possible to generate phase stable attosecond laser pulses in the soft X-ray region that will be used for the next generation of ultrafast experiments [35].

## 1.5 Direct frequency comb spectroscopy

Since optical frequency combs possess a very large number of precisely frequency calibrated laser channels, it is natural to think of using these lasers to perform high precision and broadband spectroscopy over massively parallel detection channels. The first implementation of this idea, called 'direct frequency comb spectroscopy' (DFCS), used a precision scan of $f_r$ to recover a serial detection of high resolution spectral features of $^{87}$Rb across a broad spectral range [36]. More recent approaches to molecular detection that use broad bandwidth frequency combs have indeed created parallel detection schemes that in a single shot record large spectral bandwidths [37][38]. Such detection schemes have allowed the simultaneous measurement of hundreds of transitions from several different molecules.

Since frequency combs have high peak intensities due to their pulsed output,

nonlinear frequency conversion can be implemented for easy access to spectral regions spanning from the UV to the far infrared [39] [40]. Therefore, these lasers can provide broad spectral coverage for probing a wide variety of atomic and molecular transitions. Another nice feature is that the periodic structure of the comb is ideal for efficient coupling to the resonant modes of a high finesse optical cavity. The subject of this thesis, 'Cavity-enhanced direct frequency comb spectroscopy', (CE-DFCS) takes advantage of this fact to combine the previously mentioned features of DFCS with highly sensitive detections of weak or dilute atomic and molecular absorbers that is made possible by cavity enhancement. Because of its combination of high resolution, high detection sensitivity, and broad spectral coverage, CE-DFCS has enormous potential for applications in the scientific and industrial communities.

In the scientific community, sensitive and high resolution spectroscopy over a large spectral window is useful for many areas of research. For instance, studies of atmospheric chemistry, climate change, and pollution can benefit a great deal from the capability to monitor multiple molecules simultaneously [41][42]. Molecular physics investigations of potential energy surfaces, energy level structure, local and eigen-mode dynamics, intramolecular energy redistributions, interaction dynamics, and chemical reactions all desire spectroscopic probes with high spectral resolution and accuracy over a wide range of spectral coverage [43][44]. For the emerging field of ultracold molecules, our ability to photoassociate cold molecules from pairs of free atoms depends on extensive spectroscopic probes to find the most efficient photoassociation pathways [45]. To study a new class of collision and reaction dynamics in the low energy limit [46][47], the need for higher resolution and sensitivity while under a broad spectral coverage is now of more urgent importance [48][49].

In the industrial community, CE-DFCS has the potential to revolutionize

applications that are currently being performed with single frequency laser and open the door to many others that were not previously possible. For example, human breath contains more than 1000 different molecules in trace quantities [50]. Already, many of these molecules, so called 'biomarkers', have been correlated to specific diseases and metabolic processes. While single frequency trace detection systems can determine the presence and quantity of one or a few of these molecules, CE-DFCS has the potential to rapidly determine the entire chemical composition of a breath sample. Such an advance in real-time breath measurement would enable large-scale studies of human breath with the goal of low cost, non-invasive health screening. In the semi-conductor industry, the manufacturing yield and performance of integrated circuits depends strongly on the concentrations of trace impurities in the gases used to make these chips. While single frequency systems have been used to detect one of these impurities, CE-DFCS could be used to monitor a wide variety of detrimental impurities simultaneously. These are only a couple of examples where CE-DFCS enables trace detection applications that were not previously possible. Other potential applications include hazardous materials and explosives detection and environmental quality and pollution monitoring.

## 1.6 Thesis outline

In this thesis we will explore the newly developed technique in laser spectroscopy called cavity-enhanced direct frequency comb spectroscopy (CE-DFCS). Since this is a new technique, developed during the course of my Ph.D. studies, many of the following chapters are devoted to introducing an understanding of the building blocks and the concepts that comprise CE-DFCS systems. In the first chapter, we explore the properties of optical frequency combs. We also discuss the various types of mode-locked laser that can be used to generate frequency combs,

and their potential applications to atomic and molecular spectroscopy. Particular attention will be paid to the erbium-doped fiber comb including guidelines for designing these lasers and the performance that can be achieved.

In Chapter 3, we turn our attention to optical enhancement cavities and the properties that make them useful for CE-DFCS. We develop a mathematical description of a cavity made from two quarter wave stack dielectric mirrors. We then discuss techniques for measuring the dispersion and finesse of these types of cavities. Chapter 4 focuses on methods for coupling a frequency comb to a high finesse optical cavity. This discussion will begin with the fundamental topics of aligning and mode-matching a laser beam to an optical cavity. We will then present several strategies for efficiently coupling the comb frequencies to the optical cavity modes and discuss advantages and disadvantages of each.

In Chapter 5 we introduce several different implementations of cavity-enhanced spectroscopy including cavity ringdown spectroscopy (CRDS), cavity enhanced absorption spectroscopy (CEAS), and transient cavity enhanced absorption spectroscopy (T-CEAS). Evaluations of each measurement technique are given from both a mathematical and practical implementation point of view. In Chapter 6, we present a discussion of detection techniques for reading out the multitude of frequency channels contained in the cavity transmitted beam. Chapter 7 discusses the first set of applications of CE-DFCS. Here, we present a series of experiments using CE-DFCS for trace detection of molecules, human breath analysis, and characterization of supersonically cooled molecular jets. Finally, Chapter 8 concludes with a summary of the current state of the art of CE-DFCS including a discussion of ongoing research and the latest applications of this technique. This chapter ends with an outlook of experiments that are on the horizon and a bit of dreaming about the future of CE-DFCS.

# Chapter 2

# Optical frequency comb properties and sources

In this chapter, we will explore mode-locked laser sources that can be used to generate optical frequency combs for CE-DFCS systems. We begin with a discussion of the general properties of frequency combs by developing mathematical representations for the output of these lasers in both the time and frequency domains. We then discuss methods for measuring and controlling the frequencies of the comb. In the following section, we present an overview of the different kinds of mode-locked lasers that have been developed, and the corresponding atomic and molecular transitions that they can be used to probe. The chapter concludes with a detailed discussion of mode-locked erbium fiber lasers including: the physical mechanisms responsible for their operation, design guidelines, and the performance of these lasers.

## 2.1 Optical frequency comb properties

Many of the same properties that make the frequency comb an excellent tool for counting optical frequencies and transferring coherence across vast spectral regions also make it an ideal light source for broadband, cavity enhanced spectroscopy. Frequency combs are capable of covering very large spectral ranges of hundreds of terahertz, thus enabling investigations of global energy level struc-

ture for multiple atomic and molecular species. At the same time, the spectrally sharp and precisely defined frequency structure of the comb components allow high-resolution and frequency-calibrated spectroscopy across massively parallel detection channels. For the same reason, the frequency comb is ideal for sensitive intra-cavity spectroscopy since it can be efficiently coupled to a corresponding set of resonant modes of a high finesse optical cavity across a wide spectral region.

### 2.1.1 Time and frequency domain properties of the frequency comb

The time and frequency domain representations of a comb are illustrated in Fig. 2.1. In the time domain, the laser emits a train of femtosecond pulses described by the time varying electric field

$$E(t) = \sum_{n=1}^{n_f} A_n(t) e^{i(\omega_c t - n\omega_c t_{rt} + n\Delta\phi_{ce} + \phi_o)}. \tag{2.1}$$

Here, $n$ is the pulse number, $n_f$ is the total number of pulses in the train, $A_n(t)$ is the shape of the $n^{th}$ pulse, and $t_{rt}$ is the time between consecutive pulses. $\omega_c$ is the center frequency of the comb spectrum, $\Delta\phi_{ce}$ is the phase slip between the pulse envelope and the carrier wave for adjacent pulses, and $\phi_o$ is a constant phase-offset between the pulse envelope and the underlying carrier wave. In order to derive specific connections between the time and frequency representations of the comb, a Gaussian pulse shape is assumed

$$A_n(t) = E_p e^{\frac{-(t-nt_{rt})^2}{\tau^2}}. \tag{2.2}$$

Here, $E_p$ is the peak electric field and $\tau$ is the 1/e half-width of the pulse duration. Furthermore, we assume that all frequencies contained in the pulse are perfectly overlapped in time. This condition is equivalent to a 'transform-limited', or 'chirp-free' pulse. The unique property of a transform-limited pulse is that the pulse

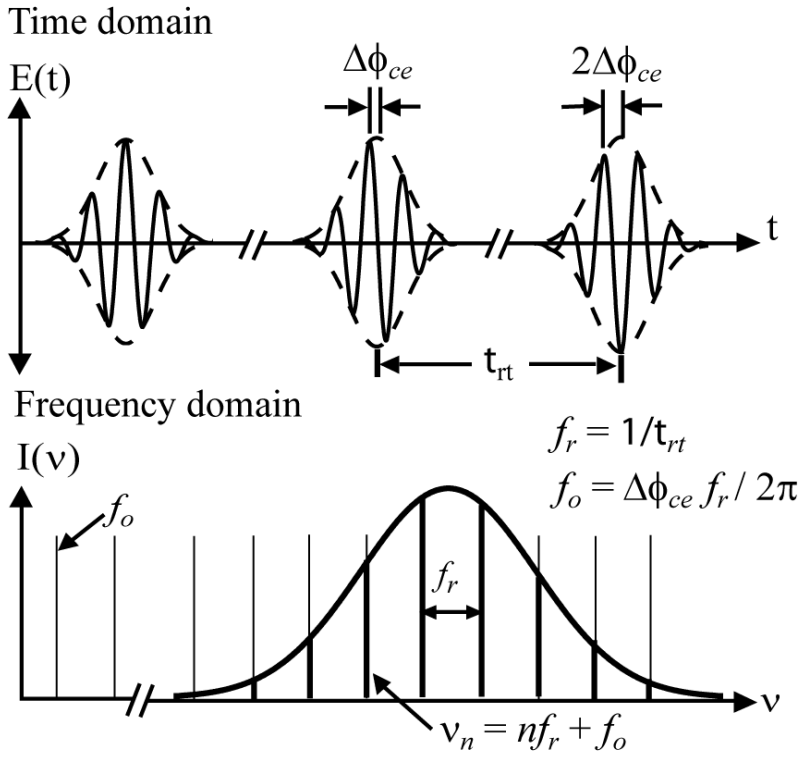


Figure 2.1: The time and frequency domain properties of an optical frequency comb. The top panel shows the time domain representation of a mode-locked pulse train including the temporal spacing between pulses ($t_{rt}$) and the evolution of the carrier envelope phase ($\Delta\phi_{ce}$). The bottom panel shows the frequency domain picture where the evenly spaced comb modes with frequencies $\nu_n$ lie beneath the laser's spectral envelope.

duration is determined only by the width of the frequency comb spectrum. While these assumptions do not affect the frequency comb structure, they are useful for understanding the relationship between the pulse duration and the extent of the comb spectrum.

The frequency domain picture of the comb can be derived by taking the Fourier transform of the pulse train.

$$E(\omega) = E_p e^{i\phi} \sum_{n=1}^{n_f} e^{i(n\Delta\phi_{ce} - n\omega_c t_{rt})} \int_{-\infty}^{\infty} e^{\frac{-(t-nt_{rt})^2}{\tau^2}} e^{i(\omega_c - \omega)t} dt. \tag{2.3}$$

Evaluating the Fourier integral yields an expression for the frequency spectrum of the comb

$$E(\omega) = E_p e^{i\phi}\tau\sqrt{\pi}\sum_{n=1}^{n_f} e^{\frac{-(\omega-\omega_c)^2\tau^2}{4}} e^{i(n\Delta\phi_{ce}-n\omega_c t_{rt})} e^{int_{rt}(\omega_c-\omega)} \tag{2.4}$$

$$= E_p e^{i\phi}\tau\sqrt{\pi}\sum_{n=1}^{n_f} e^{\frac{-(\omega-\omega_c)^2\tau^2}{4}} e^{i(n\Delta\phi_{ce}-n\omega t_{rt})}. \tag{2.5}$$

Analysis of this Eq. 2.5 reveals several properties of the frequency domain representation of the comb. First, the power spectral envelope ($P \propto |E|^2$) is a Gaussian with a full width at half maximum (FWHM) that is inversely proportional to the pulse duration

$$\delta\omega_{FWHM} = \frac{2\sqrt{2\ln(2)}}{\tau}. \tag{2.6}$$

Also, the spectral envelope has a center frequency of $\omega_c$. From the oscillatory term, we see that the broad spectral envelope is comprised of a comb of sharp peaks occurring at frequencies for which the phase of consecutive pulses adds coherently. This condition can be written as $\Delta\phi_{ce} - \omega t_{rt} = 2\pi m$. Solving for $\omega$ results in an equation for the comb frequencies [19]

$$\omega_m = \frac{2\pi m}{t_{rt}} + \frac{\Delta\phi_{ce}}{t_{rt}}. \tag{2.7}$$

Further analysis of Eq. 2.5 shows that as the total number of pulses $n_f$ becomes large, the individual comb components become narrow in frequency.

By defining the repetition frequency ($f_r = 1/t_{rt}$) and the carrier-envelope-offset frequency ($f_o = \Delta\phi_{ce}/2\pi t_{rt}$) we arrive at the commonly used expression for the comb frequencies $\nu_m = mf_r + f_o$ [51][52]. For optical frequency combs in the visible and near IR, the comb mode index $m$ takes on values ranging from $10^5$ to $10^7$, depending on $f_r$. Typical values for $f_r$ are constrained by the cavity length of the mode-locked laser. Practical lengths for these laser cavities range from 1 cm to 10 m corresponding to an $f_r$ range of 10 MHz $< f_r <$ 10 GHz. $f_o$ can take on

values of $-\frac{f_r}{2}<f_o<\frac{f_r}{2}$ determined by the difference between the group and phase velocity of light inside the laser cavity.

### 2.1.2 Measurement and control of the comb frequencies

Precise control of $f_r$ and $f_o$ establishes the comb as an accurate frequency tool for atomic and molecular spectroscopy and also permits efficient coupling of the comb to the modes of a high finesse passive optical cavity. To implement control, one first needs to measure $f_r$ and $f_o$. $f_r$ can be determined directly from the pulse train incident on a fast photodiode while $f_o$ requires nonlinear interferometry [21][19][53]. The typical nonlinear interferometry involves generating an octave of comb spectrum with the use of highly nonlinear fiber or photonic crystal fiber. The long wavelength edge of the octave spectrum is then frequency doubled to form a heterodyne beat with the short wavelength edge of the spectrum. The frequency of the resulting heterodyne beat provides a measure of the carrier-envelope-offset frequency of the comb. Two stable radio frequency references can be used subsequently to stabilize $f_r$ and $f_o$ via servo transducers acting on the laser cavity length and the intra-cavity dispersion. A frequency comb can also be stabilized directly to a passive optical cavity by detecting the cavity response to the incident comb spectrum in the optical domain [54][55], as discussed later in section 4.2.

## 2.2 Comb sources and their applications to spectroscopy

Many different types of mode-locked laser sources exist to provide coverage for a wide variety of spectral regions from blue to the mid IR spectral regions. When nonlinear frequency conversion and spectral broadening techniques are im-

plemented, the spectral coverage can be extended well into the VUV and the far infrared. The diversity of spectral regions that can be accessed allows frequency comb spectroscopy to be performed on a large variety of atomic and molecular systems. In this section, we will provide an overview of several types of mode-locked laser that can be used to generate frequency combs. Nonlinear frequency conversion to other spectral regions based on these laser sources will also be discussed. A visual guide to the spectral coverage provided by the different kinds of mode-locked lasers is shown in Fig. 2.2. This figure also shows spectral overlaps between various frequency comb sources and relevant regions for useful atomic and molecular spectroscopy.

As the first generation of precisely controlled optical frequency combs were based on Ti:sapphire lasers, it is natural that they played important roles in the first demonstrations of direct frequency comb spectroscopy [36]. Frequency comb-based cavity ring-down spectroscopy (CRDS) was also first performed with a Ti:sapphire comb on molecular overtone transitions in the 750 nm to 850 nm spectral region [37]. This system probed the high overtone transitions of $C_2H_2$, $H_2O$ and $NH_3$ as well as a weak electronic transition in $O_2$.

Many types of nonlinear frequency conversion have been used to shift the Ti:Sapphire comb from the VUV to far infrared spectral regions. Frequency down conversion of Ti:sapphire combs has been used to produce infrared frequency combs via difference frequency generation (DFG) and optical parametric oscillation (OPO) techniques [56][57] [58]. Such infrared combs have been used to probe the strong fundamental vibration transition in molecules [59]. Also, high harmonic generation (HHG) has been used to generate frequency combs in the vacuum ultra-violet regions [60][61], and with improvement in the power [62] they could be used to probe ground state transitions of noble gases [63]. Finally, while the gain bandwidth of Ti:sapphire lasers cover only 700-950 nm, subsequent super-

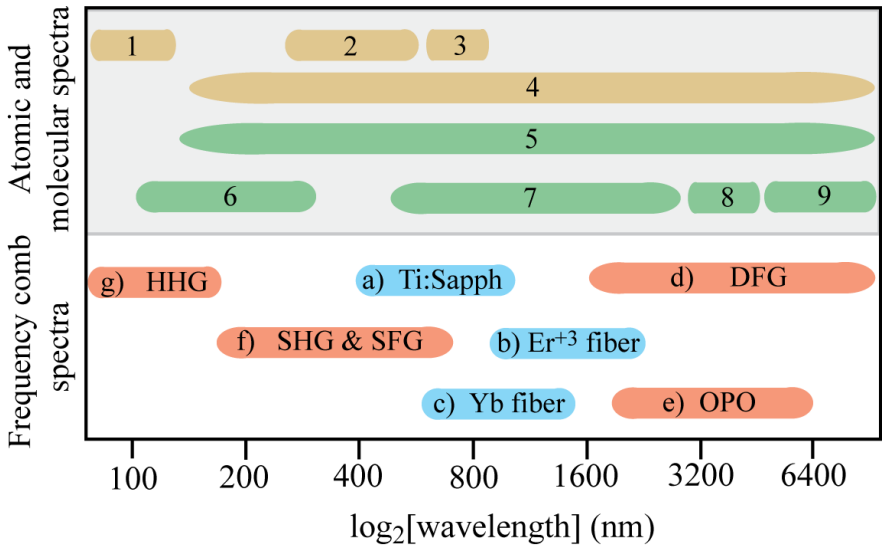


Figure 2.2: Spectral coverage for several types of mode-locked lasers and corresponding atomic and molecular transitions to which they can be applied. 1, transitions from ground states of noble gas; 2 and 3, transitions from ground states of alkaline earth or alkali atoms; 4 and 5, transitions between excited atomic or molecular states; 6, transitions from ground states of molecules; 7, overtones of molecular ro-vibrational transitions; 8 and 9, fundamental vibrations of light-nuclei or heavy-nuclei molecules. a) Ti:sapphire mode-locked lasers, after nonlinear spectral broadening, covers the entire visible range from 400 to 1200 nm; b)Erbium-doped fiber lasers (centered around 1550 nm) can be made to cover 1000 - 2400 nm via spectral broadening; c)Ytterbium-doped fiber lasers (centered around 1030 nm) can cover 600 - 1600 nm via spectral broadening. Each of these lasers can have their spectral coverage further extended via nonlinear frequency conversion using techniques listed in (d), (e), (f), and (g). We thus have the possibility of performing comb spectroscopy for nearly all of the interested atomic and molecular transitions.

continuum generations in photonic crystal and tapered telecommunications fibers [40][64] [18], and the later development of octave-spanning Ti:sapphire lasers via intra-cavity nonlinear phase modulation allow simultaneous spectral coverage extending from the deep blue to the near Infrared (NIR) using a single laser source [65][66] [67]. Due to the spectral overlap of the Ti:Sapphire spectrum with so many atomic and molecular transitions, it is likely that future Ti:Sapphire based CE-DFCS systems will find many important applications in atomic and molecular

physics.

Over the last decade, mode-locked erbium and ytterbium fiber lasers have been developed that generate highly stable frequency combs which are pumped by inexpensive laser diodes [68] [39] [69] [70]. These lasers can conveniently produce super-continuum spectra via coupling to highly nonlinear fibers [71][72]. They have been frequency converted to cover the spectral domain extending from the infrared to ultra-violet, using the same techniques described for Ti:sapphire [73][74]. The fiber lasers are compact, reliable, and robust, with turn-key operations. Thus they have a very promising future for commercial applications. Recent work has used an erbium fiber comb to perform CE-DFCS on low molecular overtones for trace detection of a wide variety of molecules at concentrations approaching 1 part per billion [75][76]. These fiber combs are conveniently located in the 1.0 $\mu$m - 2.3 $\mu$m spectral domain, overlapping with strong first-order vibration overtones of many molecules containing O-H, C-H and N-H bonds. They are also ideal for nonlinear frequency conversion to extend their spectral coverage to the mid and far infrared; an important spectroscopic region where most molecules have unique absorption signatures that can be detected using cavity enhanced spectroscopy at concentrations at or below 1 part per trillion.

More recently, efforts have been made to develop several other types of mode-locked lasers that operate in different spectral regions. The most mature of these efforts is the Cr:forsterite laser. Already these lasers have demonstrated highly stable mode-locking with spectra covering 1.0 $\mu$m-2.1 $\mu$m [77][78]. Another fairly old technology that is receiving renewed attention due to its potential for molecular spectroscopy is the thulium-doped fiber laser [79]. These lasers can already produce sub-200 femtosecond pulses with more than 100 mW of average power and tunable soliton spectra covering the 1.9 $\mu$m-2.1 $\mu$m [80][81]. Thulium fiber lasers are particularly attractive for detecting trace impurities in gases such

as arsine and phosphine used to manufacture semiconductor chips. Both arsine and phosphine have low absorption in this spectral region, while the most common impurities in these gases ($H_2O$, $CO_2$, $CH_4$, $SiH_4$), have strong absorption signatures.

Probably the most exciting prospects are mid-infrared mode-locked lasers based on $Cr^{2+}$:ZnSe and $Cr^{2+}$:CdSe gain media. Already, $Cr^{2+}$:ZnSe lasers have been passively mode-locked generating spectra tens of nanometers wide with pulse durations of several hundred femtoseconds [82]. With further development, $Cr^{2+}$:ZnSe lasers could produce extremely broad spectra due to the 1.9-2.9 $\mu$m gain bandwidth of this crystal [83]. Even more exciting is $Cr^{2+}$:CdSe gain medium [83]. This crystal has a gain spectrum that extends from 2.0 $\mu$m to 3.5 $\mu$m, ideal for the observation of hundreds of molecules via strong fundamental vibrational transitions. To date, no one has succeeded in mode-locking a laser using this gain medium. However, the wide range of applications that would be enabled by mid-IR mode-locked lasers are very enticing, and will certainly motivate future development of these types of lasers.

## 2.3 The mode-locked erbium fiber laser

Currently the most widely used mode-locked fiber laser, and also the easiest to design and construct, is the erbium-doped fiber laser. Due to the huge amount development of erbium fiber components for the telecommunications industry, these lasers are relatively inexpensive and highly reliable. Furthermore, the demonstrated ability to frequency convert their output to a variety of spectral regions from the UV to mid-IR make them extremely useful for CE-DFCS applications.

In this section, we present an overview of mode-locked erbium-doped fiber

laser. We begin by describing physics that enables the operation of these lasers including: the energy level structure of $Er^{3+}$, the absorption spectrum of erbium-doped fibers, and the mechanism responsible for mode-locking. Next, we discuss the crucial design criteria for constructing these lasers. We provide guidelines for choosing values of the intra-cavity dispersion and pulse energy that lead to stable mode-locking. We also discuss how to achieve the correct gain ratio for light at 1530 nm and 1560 nm to initiate passive mode-locking. Finally, we present two specific mode-locked erbium fiber lasers designs along with complete characterizations of the performance of each system.

The reader should note that there are two main types of mode-locked erbium fiber lasers, stretched-pulse lasers and soliton lasers. We will only discuss design considerations for stretched-pulse lasers in this section. The reasons for this are two-fold. First, sideband generation in soliton lasers due to periodic perturbations limit the pulse duration and lead to narrower spectral widths than can be achieved with stretched-pulse lasers. Second, the net positive cavity dispersion and longer average pulse durations in the stretched-pulse laser allow for higher pulse energy and hence higher average laser power. For further information on both types of erbium fiber lasers see references [84] [68].

### 2.3.1 Energy levels and mode-locking physics of the $Er^{3+}$ fiber laser

The $Er^{3+}$ energy level diagram in Fig. 2.3a shows the relevant transitions for the erbium-doped fiber laser. A diode laser at 980 nm is used to pump the erbium from its ground state $|1\rangle$, to excited state $|3\rangle$. This state undergoes rapid, nonradiative decay to metastable state $|2\rangle$ [85]. Lasing occurs on the $|2\rangle \rightarrow |1\rangle$ transition when the transition $|1\rangle \rightarrow |3\rangle$ is pumped sufficiently hard to create a population inversion between levels $|2\rangle$ and $|1\rangle$. There have been several studies

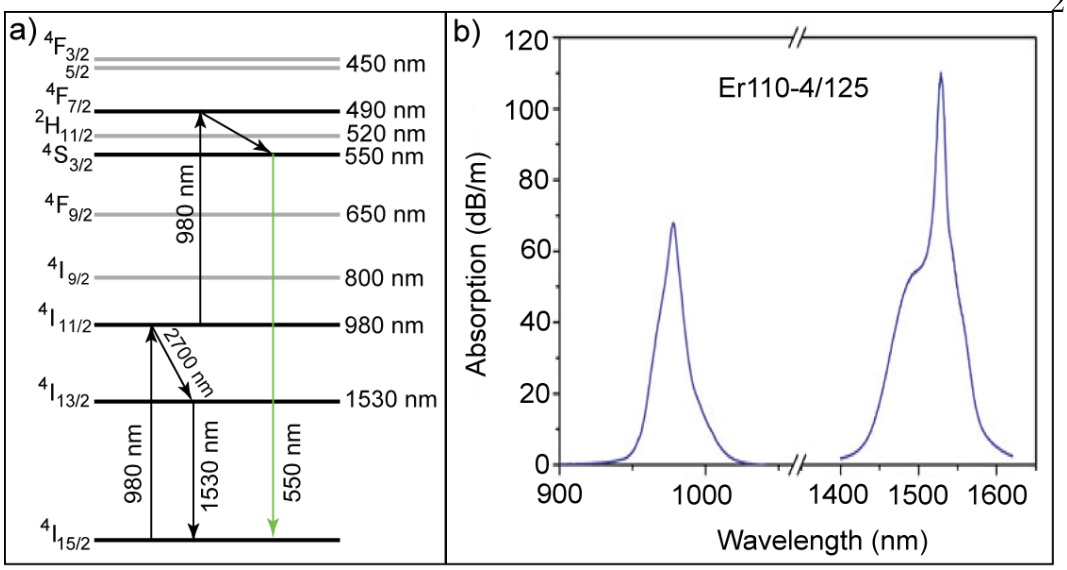


Figure 2.3: a) Energy level diagram of $Er^{3+}$ reproduced from [88]. b) The absorption spectrum for the Leikki Er110-4/125 erbium-doped fiber taken from the Thorlabs website [89].

of the pumping threshold to achieve gain in erbium-doped fibers [86] [87][85]. A particularly useful set of analytical equations for determining the optimal gain fiber length based on $Er^{3+}$ doping concentrations and 980 nm pumping power was presented by Peroni *et al.* [87]. When $Er^{3+}$ is doped into a host glass, a complicated combination of homogeneous and inhomogeneous broadening result in a broad absorption band that arises from 56 unresolved Stark transitions [88]. The absorption bands for the Leikki Er110-4/125 erbium-doped fiber are shown in Fig. 2.3b. The broad emission/absorption spectrum for erbium-doped fibers make them an excellent candidate for mode-locked operation.

Most $Er^{3+}$ fiber lasers are mode-locked using a technique called polarization additive pulse mode locking (P-APM) [84][68]. Here, the optical Kerr effect induces an intensity dependent rotation of the laser polarization that, in conjunction with polarization optics, creates different levels of intra-cavity loss for CW and pulsed operation. The intensity dependent polarization rotation can be

understood by an examination of an elliptically polarized beam propagating in a material with a nonlinear index of refraction. As an optical field $E$ travels through the fiber, it causes a polarization of the medium $\mathcal{P} = \chi_e E$. In the case of strong optical fields, higher order terms of the material susceptibility must be considered

$$\chi_e = \chi^{(1)} + \chi^{(2)}E + \chi^{(3)}E^2 + \dots. \tag{2.8}$$

The materials used to make optical fiber are typically amorphous which implies inversion symmetry such that $\chi^{(2)} = 0$ [90]. In the SI unit system, the material index of refraction is related to the susceptibility by $n^2 = 1 + \chi_e$ [91]. The intensity-dependent index of refraction takes the form

$$n = n_o + n_2 I, \tag{2.9}$$

where $I = 2n_o|E|^2/Z_o$, $Z_o = \sqrt{\mu_o/\epsilon_o}$, $n_o = \sqrt{1+\chi^{(1)}}$, and $n_2 = 3Z_o\chi^{(3)}/(4n_o^2)$. The nonlinear index gives rise to an intensity-dependent phase shift for light propagating through the fiber

$$\phi(z,t) = (n_o + n_2 I(t))kz. \tag{2.10}$$

The phase shift can be viewed as a polarization rotation by writing the nonlinear index of refraction in a circular polarization basis [92]

$$n_\pm \simeq n_o + 4n_o n_2(|E_\pm|^2 + 2|E_\mp|^2), \tag{2.11}$$

where $E_-$ and $E_+$ refer to right-hand and left-hand circular polarized fields. The index difference experienced by fields $E_+$ and $E_-$ leads to a polarization rotation of angle

$$\theta = \frac{\omega}{2c}(n_+ - n_-)z = \frac{2\omega n_o n_2}{c}(|E_-|^2 - |E_+|^2)z. \tag{2.12}$$

Here, the tensor component of $\chi^{(3)}$ responsible for the rotation is $\chi_{xyyx}$ [92]. From Eq. 2.12 we can see that linearly polarized light experiences no rotation since

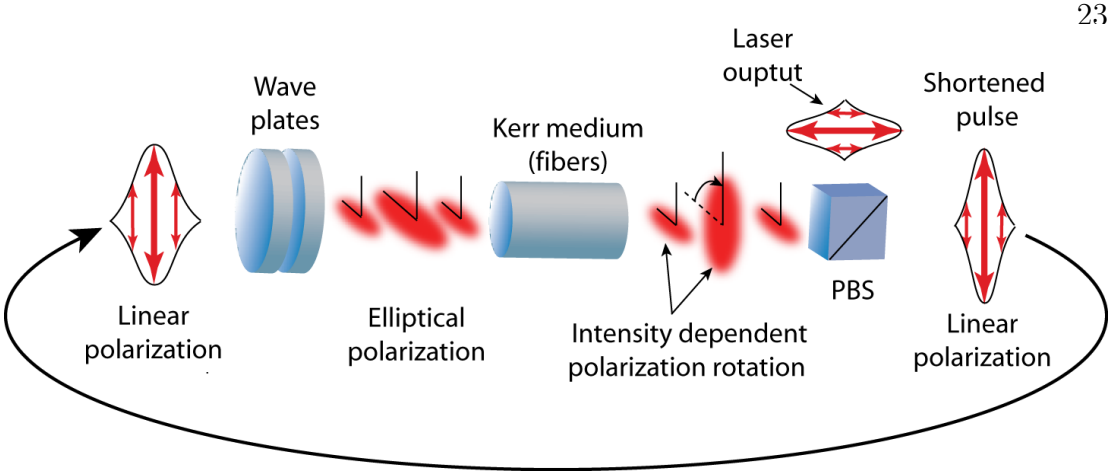


Figure 2.4: Schematic of the polarization additive-pulse mode-locking mechanism. The incident linearly polarized pulse is converted to an arbitrary polarization state by intra-cavity wave plates. In the Kerr medium, the high-intensity pulse center experiences a large rotation of its polarization state while the polarization of the low intensity wings remain unchanged. The intra-cavity wave plates are used to align the polarization of the center of the pulse to be transmitted through the PBS for efficient recoupling to the laser cavity. Due to the intensity-dependent polarization rotation, the recoupled pulse is shortened during each trip around the cavity resulting in passive mode-locking. The rejection port of the PBS is used as the laser output.

$|E_+|^2 = |E_-|^2$. Also, rotations of circularly polarized light produce no measurable effect. Finally, the rotation experienced by elliptically polarized light depend on both the intensity and the ellipticity of the beam.

A schematic illustrating how nonlinear polarization rotation leads to polarization additive pulse mode locking is shown in Fig. 2.4. In this depiction, the laser pulse is broken into three sections representing the low-intensity front and back edges of the pulse and the high-intensity pulse center. First, a linearly polarized pulse is incident from the left on a quarter and a half wave plate to create an arbitrary elliptical polarization state. Next, the pulse enters the Kerr medium where it experiences an intensity-dependent polarization rotation described by Eq. 2.12. This is represented in Fig. 2.4 by a 90° rotation of the intense pulse center while the polarization of the wings of the pulse remain unchanged. Finally,

a polarizing beam splitter (PBS) is used to recouple the center of the pulse into the laser cavity while output-coupling the wings of the pulse. This configuration leads to high intra-cavity loss for CW lasing and low loss for pulsed operation. Therefore, by choosing the correct orientation of the wave plates with respect to the PBS, the laser will passively mode lock. Of course, this is only a qualitative description of P-APM. A more rigourous derivation of the mode-locking dynamics can be found in Ref. [68].

### 2.3.2 $Er^{3+}$ fiber laser design strategies

In the last section, we saw how nonlinear polarization rotation can give rise to passive mode-locking of $Er^{3+}$ fiber lasers. In this section, we will discuss design considerations for achieving an intra-cavity pulse intensity that leads to the appropriate the nonlinear polarization rotation for mode-locking. The first decision to make when designing any mode-locked laser is the repetition rate. Once a repetition rate is chosen, target values for the average power and intra-cavity dispersion can be specified that will lead to stable mode-locking. To date, mode-locked erbium fiber lasers have been constructed with repetition rates ranging from 10 MHz to 250 MHz, though higher repetition rates will likely be achieved in the near future [68][93]. For CE-DFCS applications, frequency combs with high repetition rates in the range of 100 MHz to 250 MHz are preferred since these lasers can be efficiently coupled into reasonably small (0.6 m-1.5 m) optical cavities.

Figure 2.5 shows the dispersion, pulse energy, and total fiber length times pulse energy for several mode-locked erbium fiber lasers. The most notable feature of Fig. 2.5a is the difference in laser performance between laser cavities with net positive versus negative dispersion. As mentioned previously, lasers with neg-

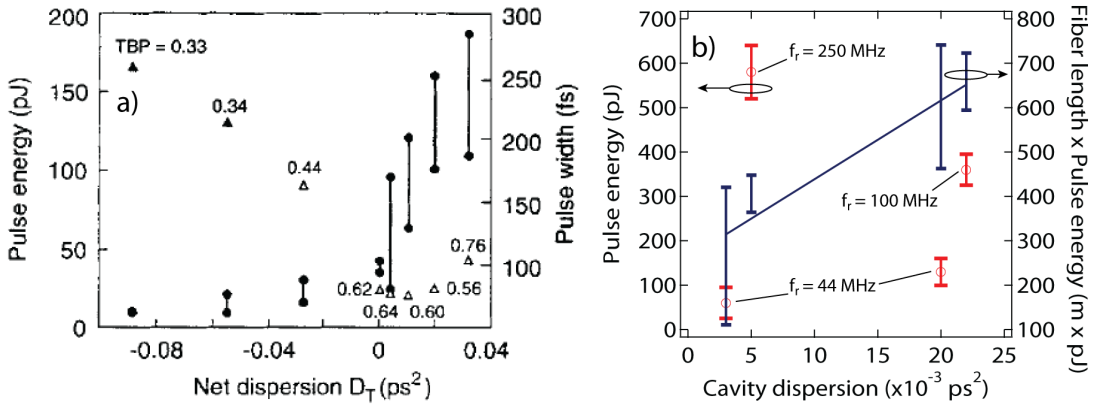


Figure 2.5: a) The observed range of pulse energies (dots) and minimum pulse duration (triangles) versus net cavity dispersion for several mode-locked erbium fiber lasers (figure taken from [84]). The numbers next to the triangles give the time-bandwidth product for each laser. b) The range of pulse energies (red) and pulse energy times fiber length (blue) versus total fiber length for four fiber lasers. Data for the two 44 MHz lasers was from [84] while the 100 MHz and 250 MHz lasers were constructed in Ye labs.

ative cavity dispersion have both lower pulse energy and smaller time-bandwidth products than lasers with positive cavity dispersion. Also shown in Fig. 2.5a is the fact that lasers with larger positive dispersion require higher pulse energies for mode-locking. Generally speaking, the values for the net cavity dispersion shown in Fig. 2.5a provide good guidelines for designing a mode-locked erbium fiber laser. For low repetition rate laser designs, it is wise to choose higher dispersion to achieve longer intra-cavity pulses and hence higher output power. However, for designing a high repetition rate laser, it is better to choose lower dispersion to compensate for the lower energy per pulse and the shorted fiber lengths associated with these lasers.

Figure 2.5b illustrates that the cavity round-trip nonlinear phase shift is an important parameter for stable mode-locking. In Fig. 2.5b both the pulse energy (red) and the pulse energy times the total intra-cavity fiber length (blue) are plotted against the total cavity dispersion for four mode-locked lasers. If only the

pulse energy were plotted, there would be seemingly no trend linking the operation of these four lasers. However, when the pulse energy times the fiber length is plotted, a clear trend can be seen as a function of net cavity dispersion. This indicates that the P-AMP process leads to mode-locking for a specific range of values of the round-trip nonlinear phase shift [68]. In one cavity round-trip, a pulse will experience a nonlinear phase shift given by $\Delta\phi_{nl} = n_2 I L$, where $n_2$ is the nonlinear index of refraction of the fiber, $I$ is the pulse intensity, and $L$ is the total fiber length. The important point here is that pulse intensity is proportional to the average intra-cavity pulse duration which is proportional to the net intra-cavity dispersion. Hence, $I \propto \beta E_p$, where $\beta$ is the intra-cavity dispersion and $E_p$ is the pulse energy. So, if the intra-cavity dispersion is increased, either the pulse energy, or the fiber length need to be increased to maintain the same nonlinear phase shift.

Of course, there are many factors that complicate this general rule including the fact that the pulse is changing duration as it propagates through the cavity so it matters where in the cavity the pulse reaches its shortest duration. Also, different fibers have different mode field diameters which lead to different intensities for the same pulse energy. Finally, different fibers are made with different types of glass and sometimes include dopants which can lead to different values of the nonlinear index $n_2$. Nevertheless, the trend in Fig. 2.5b provides a good estimate for the combinations of pulse energy, fiber length, and cavity dispersion that will lead to mode locking.

The final consideration for designing a mode-locked erbium fiber laser is gain. In the previous paragraphs, we have found that the proper balance of pulse energy and cavity dispersion are required for mode-locking. Accordingly, we must provide enough gain in the laser cavity to reach the required pulse energy. For this, the gain equations from reference [87] and an estimate of the total loss in

the laser cavity can be used to determine the intra-cavity pulse energy.

Besides providing sufficient gain to reach the desired pulse energy, there is also an issue of gain competition. Experience with mode-locking erbium fiber lasers reveals that a newly constructed fiber laser will be likely to mode-lock if it will CW lase at 1560 nm. However, since the peak of the erbium emission spectrum is at 1530 nm (see Fig. 2.3), a laser that is designed with the optimal length of gain fiber will lase strongly at 1530 nm, but probably not at 1560 nm. To remedy this problem, it is common practice to use a length of gain fiber that is ∼20-40% longer than what is suggested by the gain equations. By doing this, the gain for light at 1530 nm will decrease due to reabsorption, while the gain at 1560 nm will increase. The laser will be most likely to mode-lock when the gain fiber length is chosen such that CW lasing is equally likely at 1530 nm and 1560 nm.

Of course, these are only guidelines for successfully designing an erbium fiber mode-locked laser. By staying close to the parameter space outlined here, chances are your design will turn out fine. But beware, even if you get all of the fiber parameters right and have a sound laser design, practical matters such as excessive loss at a fiber splice, or back reflections of either the erbium or pump laser wavelength can easily preclude mode-locking.

### 2.3.3 Practical matters

The basic schematic for a mode-locked erbium fiber laser and amplifier are shown in Fig. 2.6. For the current discussion, we'll focus our attention on only the laser. For more information about erbium fiber amplifiers, see [39]. The laser is pumped with a single commercially available 976-978 nm laser diode [94][95]. The pump laser is coupled into the cavity such that it is counter-propagating with

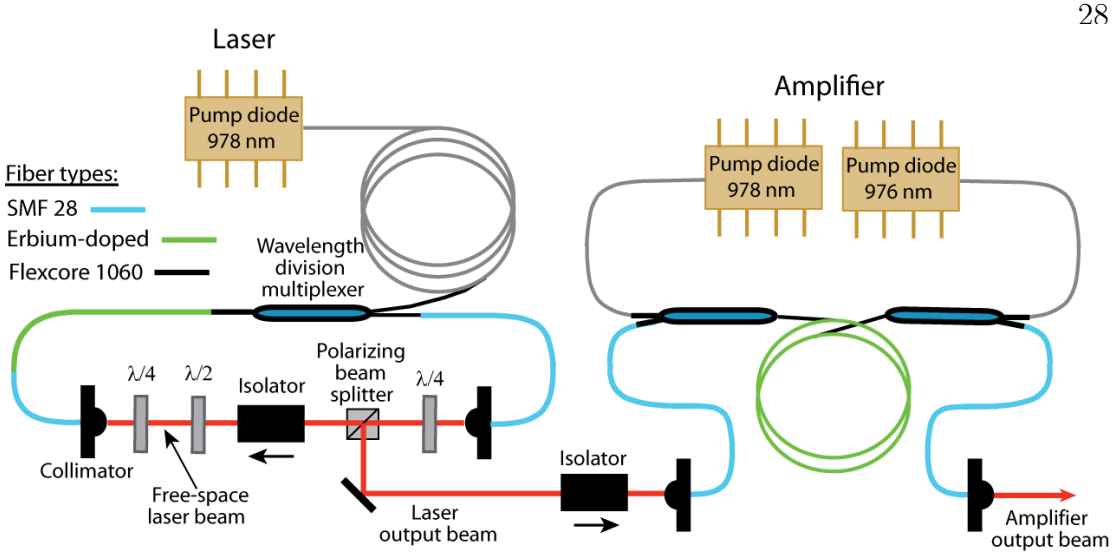


Figure 2.6: A schematic for the erbium-doped fiber comb.

respect to the laser beam. The cavity is constructed this way to extract the maximum gain from the erbium fiber. In this configuration, the laser pulse propagates toward the region of greater gain medium inversion as the pulse energy is amplified, thereby maximizing the gain. Another nice side effect of counter-propagating operation is that there is no pump light present in the laser output due to the free space isolator and the polarizing beam splitter (PBS) used for output coupling.

The laser is constructed from three types of fiber and a free space region that consists of an optical isolator and some polarization optics. The three different fiber types combine to provide the gain, dispersion, and nonlinearity required for the mode-locking mechanism. The dispersions of five common fibers used to construct erbium fiber lasers are given in Table 2.1. Fiber manufacturers will often times quote the fiber dispersion in units of $(ps/nm/km)$. Equation 2.13 provides the conversion to the more familiar units of $(ps^2/m)$.

$$\beta(ps^2/m) = D(ps/nm/km) \times \frac{\lambda(nm)\lambda(km)}{2\pi c(m/ps)} \tag{2.13}$$

Control of the repetition frequency of these lasers is addressed using two intra-cavity actuators. For coarse, manual control of $f_r$, one of the collimators

Table 2.1: Dispersion of fibers used to construct mode-locked erbium fiber lasers.

| Fiber type | Nominal dispersion $\beta(ps^2/m)$ |
|---|---|
| SMF28 | -0.022 |
| Corning Flexcor-7/125 | -0.0115 |
| Lieki ER110-4/125 | 0.0115 |
| Lieki ER80-4/125 | 0.0336 |
| OFS EDF80 | 0.075 |

can be mounted on a translation stage. Fine, albeit slow ($< 500$ Hz), control can then be achieved by placing a piezo-electric transducer (PZT) in the translation stage. For fast servoing of $f_r$ (upwards of 50 kHz), there are several options. If a low profile collimator is chosen, the collimator can be mounted directly in a fast ring PZT. Also, for lower repetition rate lasers ($f_r < 200$ MHz), a PZT fiber stretcher can be used. Finally, a small mirror mounted on a fast PZT can be used in either a sigma cavity or a folded cavity configuration [96][97]. Slow control of $f_o$ can be achieved by adjusting the angle of one of the intra-cavity waveplates. Fast control of $f_o$ is achieved by modulating the power of the 980 nm pump laser.

Table 2.2: Comparison of the performance of the 100 MHz and 250 MHz mode-locked fiber lasers.

| Laser Parameter | 100 MHz Laser | 250 MHz Laser |
|---|---|---|
| Oscillator Pump Power | 500mW | 750 mW |
| Oscillator Power | 35mW | 150 mW |
| Amplifier Pump Power | 1200 mW | 1500 mW |
| Amplified Power | 300 mW | 450 mW |
| Pulse Duration | 95 fs | 81 fs |
| Cavity Dispersion | 0.022 $ps^2$ | 0.005 $ps^2$ |
| Fiber Length | 183 cm | 70 cm |

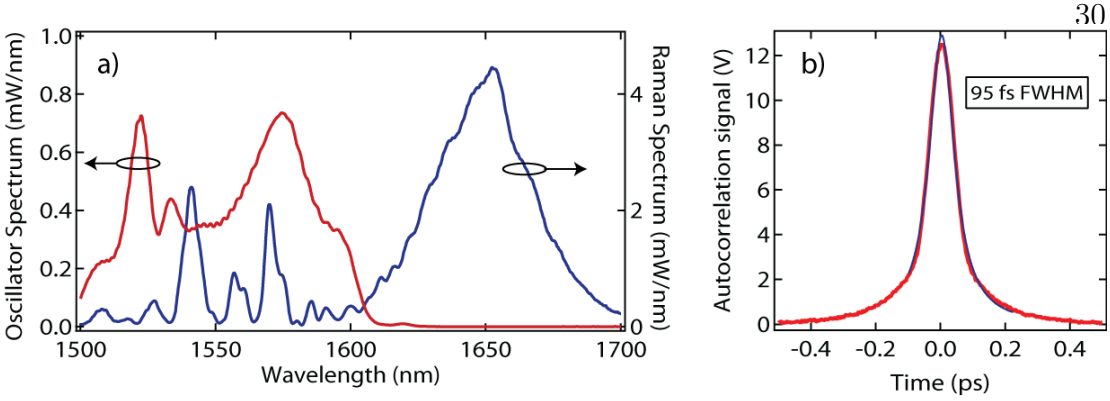


Figure 2.7: a) The spectrum of the 100 MHz $Er^{3+}$ mode-locked fiber laser directly from the oscillator (red) and after the Raman shifting amplifier (blue). b) The autocorrelation of the pulse after the laser showing an 95 fs FWHM pulse duration.

### 2.3.4 Laser performance

In this final section, we present a series of measurements that characterize the performance of a 100 MHz and a 250 MHz erbium fiber laser built in Ye labs. The list of parameters for these two lasers, shown in Table 2.2, illustrate many of the design issues mentioned in the previous sections. For instance, the 100 MHz laser requires a lower pump power, and has a lower output power than the 250 MHz laser due to the higher intra-cavity pulse energy and longer fiber lengths associated with lower repetition rate lasers. Similarly, the 250 MHz laser does not even begin to mode-lock until the output power is above 100 mW due to the short length of fiber available for accumulating nonlinear phase shift.

Figure 2.7a shows the laser spectrum (red) and the spectrum after a Raman shifting amplifier (blue) for the 100 MHz laser. The spectrum from the amplifier has been efficiently frequency shifted via a Raman process for CE-DFCS applications in the 1.6 $\mu$m to 1.7 $\mu$m spectral region. The frequency shift is achieved by pulse amplification followed by a temporal compression of the pulse in a negative dispersion piece of fiber. A Raman soliton forms in the negative dispersion fiber that shifts the spectrum of the pulse through a process known as Raman induced

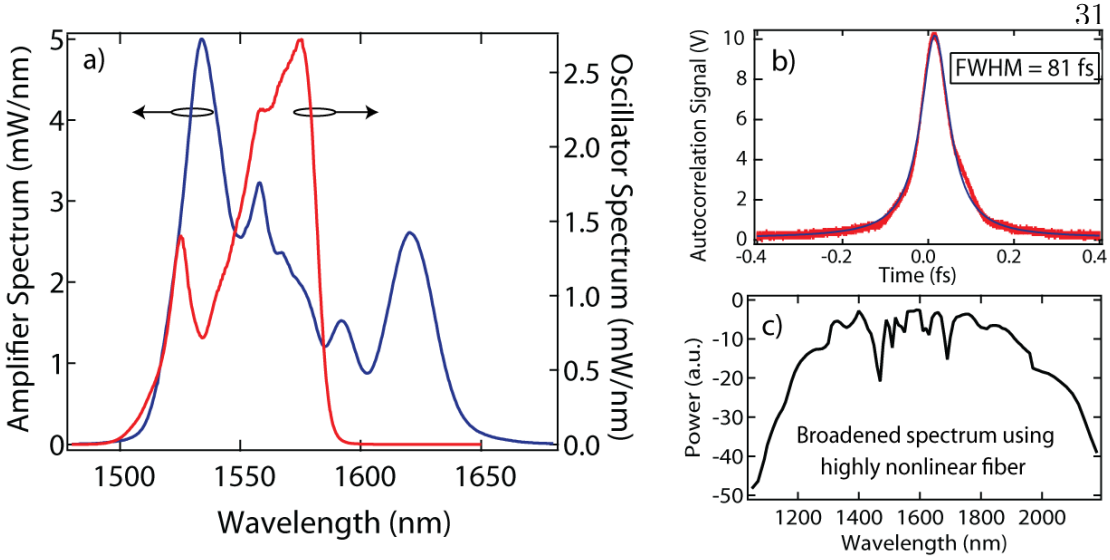


Figure 2.8: a) The spectrum of the 250 MHz $Er^{3+}$ mode-locked fiber laser directly from the oscillator (red) and after the amplifier (blue). b) The autocorrelation of the pulse after the amplifier showing an 81 fs FWHM pulse duration. c) The spectrum after the amplified pulse is passed through 10 cm of OFS highly nonlinear fiber.

frequency shift (RIFS) [98]. An autocorrelation of the laser output, shown in Fig. 2.7b, reveals a 95 fs pulse width.

Fig. 2.8a shows the laser spectrum (red) and the spectrum after the amplifier (blue) for the 250 MHz laser. The amplifier for this laser was designed to compress the pulse to its minimum duration in the positive dispersion erbium gain fiber, resulting spectral broadening due to self phase modulation (SPM) [99]. Due to SPM, the width of the spectrum after the amplifier is increased by roughly 50 nm. An autocorrelation of the pulse after the amplifier, shown in Fig. 2.7b, reveals a pulse duration of 81 fs. Considering the width of the spectrum, it is likely that this pulse could be compressed to roughly 60 fs if a silicon prism compressor were used to compress the pulse rather than the piece of SMF 28 fiber that we used to achieve 81 fs. However, for most CE-DFCS applications, the pulse duration is not important, the spectral coverage is what really matters. When the amplified 81 fs pulse is propagated through 10 cm of OFS highly nonlinear fiber,

the resulting spectrum extends from 1.1 $\mu$m to 2.2 $\mu$m (Fig. 2.8c), providing a very broadband laser source for frequency comb spectroscopy.

In general, mode-locked erbium fibers lasers are highly useful both for their wavelength agility and their ease of operation. Unlike Ti:Sapphire lasers, $Er^{3+}$ lasers will routinely stay mode-locked for months at a time due robustness of P-APM and the lack of alignment issues in fiber based laser systems. These lasers will be the primary frequency comb source used in the most of the CE-DFCS measurements presented in this thesis.

# Chapter 3

## Useful properties of passive optical cavities

In this chapter, we outline the important properties for passive optical cavities used in CE-DFCS. These properties include the finesse for detection sensitivity, the intra-cavity dispersion for comb-cavity coupling, and the spectral bandwidth for useable spectroscopy windows. This chapter is devoted to an analysis of these properties for a cavity constructed from two highly reflective mirrors with quarter-wave stack dielectric coatings. Here, we will illustrate why high finesse, low dispersion, and large spectral bandwidth are desirable qualities for a CE-DFCS cavity.

### 3.1 Mirror reflectivity and spectral bandwidth

The spectral bandwidth of a cavity refers to a spectral window for which the cavity has a high finesse and nearly uniform cavity FSR that are important for CE-DFCS applications. Both the cavity finesse and the spectral bandwidth are determined by reflectors used to construct the cavity. In this section, we will develop the properties for a type of highly reflective mirror used in all of the CE-DFCS experiments presented in this thesis. These mirrors, commonly referred to as quarter wave stack reflectors, are constructed from alternating layers of high ($n_h$) and low ($n_l$) index of refraction dielectric material (Fig. 3.1a). As we will

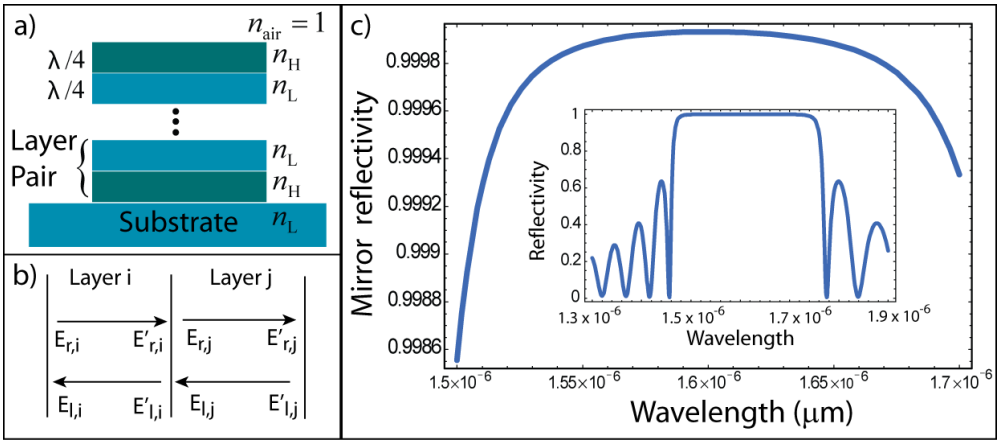


Figure 3.1: a) The quarter wave stack structure used to make ultra-high reflectivity mirrors. b) Schematic of the right and left propagating E-fields inside the $i^{th}$ and the $j^{th}$ layer in the dielectric stack. c) A calculation of the wavelength dependent reflectivity for a quarter wave stack dielectric mirror with a peak reflectivity of 1.6 $\mu$m.

see, a condition of high reflectivity is produced from alternating dielectric layers with an optical thickness of $d = \lambda/4$, where $\lambda$ is the wavelength that the mirror is designed to reflect.

The reflectivity of a quarter wave stack mirror will be developed following the transfer matrix formalism found in Klein [100]. At normal incidence, the reflection coefficient at both the $n_h$ to $n_l$ and the $n_l$ to $n_h$ interfaces can be found using the Fresnel equations

$$r_{hl} = \frac{n_h - n_l}{n_h + n_l}, \tag{3.1}$$

$$r_{lh} = \frac{n_l - n_h}{n_h + n_l}. \tag{3.2}$$

From these equations, we can see that $r_{hl} = -r_{lh}$. We will assume negligible scattering loss in the dielectric material such that the transmission coefficient is defined as $t^2 = 1 - r^2$.

To simplify the mathematical description of the total interference from many dielectric layers, the incident and reflected fields at each dielectric layer will be

represented as column vectors

$$E_i \equiv \begin{pmatrix} E_{li} \\ E_{ri} \end{pmatrix}, \tag{3.3}$$

and

$$E_j \equiv \begin{pmatrix} E_{lj} \\ E_{rj} \end{pmatrix}. \tag{3.4}$$

Here, $E_r$ and $E_l$ denote right and left propagating fields, as depicted in Fig. 3.1b. Also, a prime is used to describe the fields on the right side of the layer while unprimed denotes fields on the left side of the layer. Using these definitions, the fields on either side of an interface between the $i^{th}$ and $j^{th}$ can be determined using a transfer matrix

$$H_{ij} \equiv \frac{1}{t} \begin{pmatrix} 1 & r_{ij} \\ r_{ij} & 1 \end{pmatrix}, \tag{3.5}$$

such that

$$E_i' = H_{ij} E_j, \tag{3.6}$$

When propagating across dielectric layer $j$, the beams pick up a phase factor $e^{-i\beta_j}$ that depends on the layer thickness $d_j$, the index of refraction $n_j$, and the vacuum wavelength of light $\lambda_o$ according to

$$\beta_j = \frac{2\pi n_j d_j}{\lambda_o}. \tag{3.7}$$

The phase shift due to propagation can also be represented as a transfer matrix

$$L_j \equiv \frac{1}{t} \begin{pmatrix} e^{-i\beta} & 0 \\ 0 & e^{i\beta} \end{pmatrix}. \tag{3.8}$$

For example, this matrix can be used to propagate the beam from the right side to the left side of the $j^{th}$

$$E_j = L_j E_j'. \tag{3.9}$$

Using these matrices, we can easily represent the multiple beam interference arising from a stack of $N$ dielectric layers

$$S_{1N} \equiv H_{12}L_2 \ldots L_{N-1}H_{N-1,N} = \begin{pmatrix} S_{11} & S_{12} \\ S_{21} & S_{22} \end{pmatrix}. \tag{3.10}$$

There is one final boundary condition that is needed to make the transfer matrix formalism useful for describing quarter wave stack mirrors. If we assume that light is incident on the stack from the left, then there can be no light incident from the right on the final layer (the $N^{th}$ layer) of the stack and hence

$$E_N = \begin{pmatrix} 0 \\ E_{rN} \end{pmatrix}. \tag{3.11}$$

Using this condition, the reflection and transmission coefficients for the entire stack can be described according to

$$\begin{pmatrix} E'_{l1} \\ E'_{r1} \end{pmatrix} = \begin{pmatrix} S_{11} & S_{12} \\ S_{21} & S_{22} \end{pmatrix} \begin{pmatrix} 0 \\ E_{rN} \end{pmatrix} = \begin{pmatrix} S_{12}E_{rN} \\ S_{22}E_{rN} \end{pmatrix}, \tag{3.12}$$

where

$$r = \frac{E'_{l1}}{E'_{r1}} = \frac{S_{12}}{S_{22}} \tag{3.13}$$

and

$$t = \frac{E_{rN}}{E'_{r1}} = \frac{1}{S_{22}}. \tag{3.14}$$

The peak reflectivity of the stack occurs when

$$\beta_j = \frac{2\pi n_j d_j}{\lambda_o} = \frac{\pi}{2}. \tag{3.15}$$

for both the high and low index layers. Carrying out the matrix multiplications in Eq. 3.10 leads to a reflection coefficient of

$$r = \frac{n_l^{2N} - n_h^{2N}}{n_l^{2N} + n_h^{2N}}. \tag{3.16}$$

Finally, the reflectivity of a stack of $2N$ layers or $N$ layer pairs is

$$R = |r|^2 = \left( \frac{1 - \left(\frac{n_h}{n_l}\right)^{2N}}{1 + \left(\frac{n_h}{n_l}\right)^{2N}} \right)^2 . \tag{3.17}$$

As can be seen from Eq. 3.17, the reflectivity of a quarter wave stack depends on the number of layer pairs in the stack and the ratio $n_h$ to $n_l$. Most of the mirror coatings used for the work in this thesis were made from alternating layers of fused silica ($n_l = 1.45$) and niobium oxide ($n_h = 1.9$). Fig. 3.1c shows the reflectivity versus wavelength for a 20 layer pair mirror constructed from these materials with a center wavelength of 1.6 $\mu$m. The peak reflectivity for this mirror is $R_{peak} = 0.99992$. The wavelength dependence of the reflectivity, shown in Fig. 3.1, is found by changing the wavelength in the phase term $\beta$ and repeating the calculation in Eq. 3.17. From this calculation, we find that the spectral bandwidth of the mirror reflectivity is determined by the ratio $n_h$ to $n_l$. Larger $n_h/n_l$ lead to broader spectral bandwidths of the mirror reflectivity. In Fig. 3.1c, we can see that the combination of fused silica and niobium oxide provide high reflectivity over a spectral range covering 1.5 $\mu$m to 1.7 $\mu$m. Outside of this region, the mirror reflectivity drops very rapidly. Therefore, the useful spectral bandwidth of these mirrors is about 200 nm or $\sim$13% of the center optical frequency of the coating. However, the spectral coverage of modern optical frequency combs can be very large ($\sim$90% of the central frequency). As a result, mirror coating designs currently limit the spectral coverage that can be achieved with CE-DFCS.

In response to this, efforts toward improved designs for low-loss and low-dispersion mirrors have been intense over the past few years including the use of different dielectric materials and specialized coating designs [101]. Recently, new designs for high-finesse cavities that use prism retro-reflectors instead of mirrors have been under development. Since prism retro-reflectors are based on broad bandwidth effects, such as Brewster's angle and total internal reflection, these cav-

ities could provide spectral bandwidths of >80% of the center optical frequency with a finesse of up to 50,000 [102][103]. Recently, Johnston *et al.* coupled a spatially coherent, broadband light source into a prism cavity demonstrating a peak finesse of better than 30,000 at 1.064 $\mu$m [104]. A research effort is currently underway in Jun's lab to couple an erbium fiber comb to a cavity made from fused silica prisms to cover the 1.0 $\mu$m to 2.0 $\mu$m spectral region with a single cavity.

## 3.2 Finesse

So far, we have only discussed the reflectors that are used to construct optical cavities. Now, we turn our attention to the properties of the optical cavities themselves. The finesse is the most important property of an optical cavity because it determines the enhancement factor for the intra-cavity absorption signal that can be recovered from the cavity transmission. As the finesse increases, the cavity resonances become more sensitive to optical loss. As a result, small absorption signals become amplified by the cavity response. Precise knowledge of the cavity finesse is important for making accurate measurements of the intra-cavity absorption. In this section, we will first develop the concept of the cavity finesse and then present techniques for using an optical frequency comb to measure the finesse.

A schematic of a two-mirror cavity with light incident from the left is shown in Fig. 3.2. The amount of light transmitted and reflected from the cavity depends strongly on the frequency of the incident beam and the reflectivity and transmission coefficients of the mirrors. An expression for the transmitted field in Fig. 3.2 can be found by summing all of the intra-cavity fields

$$E_{intra-cavity} = E_0 + E_1 + E_2 + \ldots + E_n, \tag{3.18}$$

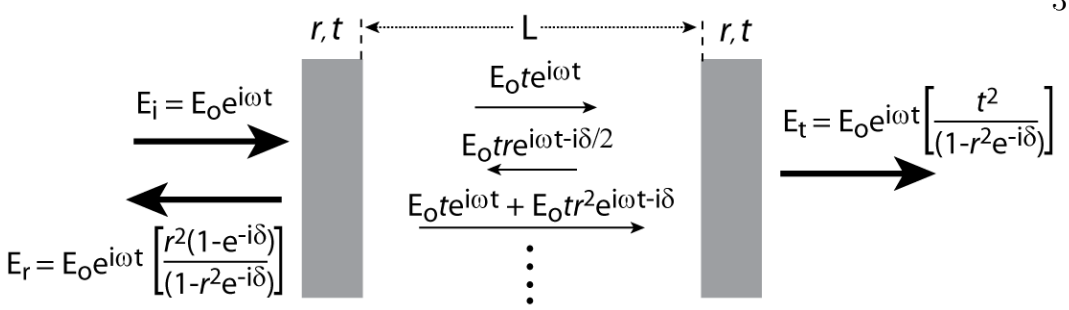


Figure 3.2: Multiple beam interference in an optical cavity with length $L$, mirror reflection coefficients $r$ and and transmission coefficients $t$.

where

$$E_0 = tE_o e^{i\omega t}$$

$$E_1 = tr^2 E_o e^{i(\omega t - 2L|\vec{k}|)}$$

$$E_2 = tr^4 E_o e^{i(\omega t - 4L|\vec{k}|)}$$

$$E_n = tr^{2n} E_o e^{i(\omega t - 2nL|\vec{k}|)}.$$

Summing the geometric series yield the intra-cavity field

$$E_{intra-cavity} = E_0 e^{i\omega t}\left[\frac{t}{1 - r^2 e^{-i\delta}}\right], \tag{3.19}$$

where $\delta = 2L|\vec{k}|$. Specifically, Eq. 3.19 describes the intra-cavity field at the input mirror. The field transmitted from the cavity is found by applying the mirror transmission coefficient to the intra-cavity field at the output mirror

$$E_t = E_0 e^{i\omega t}\left[\frac{t^2 e^{-i\delta}}{1 - r^2 e^{-i\delta}}\right]. \tag{3.20}$$

The ratio of transmitted to incident light intensity from the cavity is given by

$$\frac{I_t}{I_i} = \frac{1}{1 + F\sin^2(\delta/2)}. \tag{3.21}$$

where $F$ is known as the coefficient of finesse and is related to the mirror reflection coefficient according to

$$F = \left(\frac{2r}{1 - r^2}\right)^2. \tag{3.22}$$

The ratio $I_t/I_i$ is plotted as a function of $\delta$ in Fig. 3.4 for three values of $F$. As $F$ increases, the window of frequencies transmitted from the cavity becomes narrower. The most common measure of the width of the cavity resonance is called the finesse $\mathcal{F}$ [105]. The finesse is defined as the ratio of the interval between cavity modes ($2\pi$) to the full width at half maximum phase width of the cavity resonance ($\Delta\delta$) such that

$$\mathcal{F} \;=\; \frac{2\pi}{\Delta\delta} \;=\; \frac{\pi\sqrt{F}}{2}. \tag{3.23}$$

The most common, and perhaps the most useful, expression for the finesse is written in terms the cavity free spectral range (FSR) and linewidth ($\Delta\nu$)

$$\mathcal{F} = \frac{FSR}{\Delta\nu}. \tag{3.24}$$

In Chapter 5, we will quantify the relationship between the cavity finesse and the enhancement of detection sensitivity of intra-cavity absorption measurements. For now, we will discuss how to measure the cavity finesse, an important precursor to quantitative intra-cavity absorption measurements.

For high finesse cavities ($\mathcal{F} > 1000$), the cavity finesse is usually measured via cavity ringdown spectroscopy (CRDS) [5] [6]. CRDS measurements are performed by injecting laser light into a resonant mode of the cavity and then rapidly switching off the incident light. Without input, the intra-cavity power decays at a rate that is determined by the ratio of the total cavity loss and the cavity round-trip time (i.e., the linewidth of a cavity resonance mode). The cavity decay time $\tau_{cavity}$ and finesse $\mathcal{F}$ are thus related by $\mathcal{F} = 2\pi\tau_{cavity}FSR$.

It is straightforward to use a single-frequency CW laser for CRDS measurements [106][107][108]. For fast switching of the light source, the laser frequency can be swept quickly across the cavity resonance such that the time the laser spends on resonance with the cavity is shorter than the cavity lifetime. Another way of switching the incident light is to use an acousto-optic or electro-optic mod-

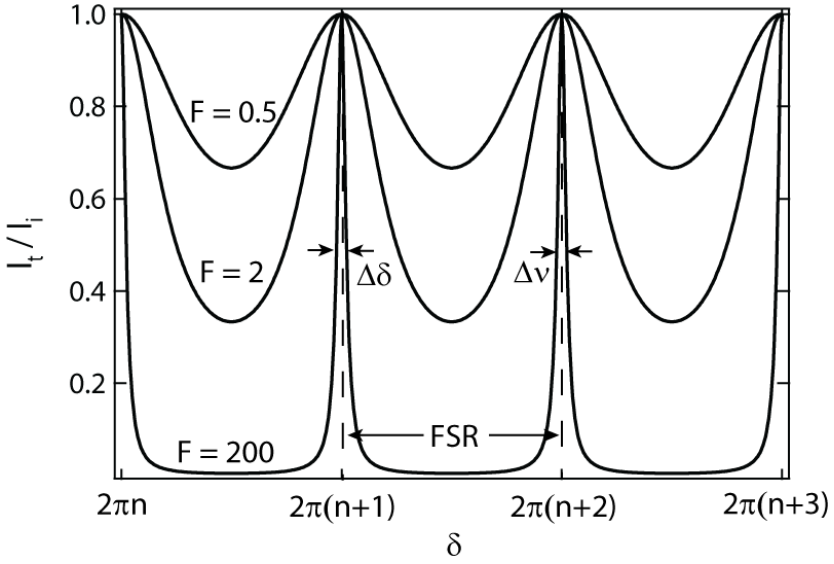


Figure 3.3: The ratio of the incident and transmitted intensity as a function of $\delta$ for $F$ values of 0.5, 2, and 200. As $F$ increases phase interval corresponding to cavity transmission $\Delta\delta$ decreases. When the phase axis is converted to units of frequency, the cavity FSR corresponds to the separation between cavity resonances and $\Delta\nu$ is the full width at half maximum linewidth.

ulator that can provide switching times of less than a few hundred nanoseconds, sufficiently shorter than a typical high-finesse cavity lifetime. CRDS measurements can also be performed with an optical frequency comb if the mode spacings of the cavity and the comb are roughly matched. For a more detailed discussion of techniques for coupling the comb frequencies to an optical cavity, see Chapter 4. The frequency comb components can then be frequency-scanned across the corresponding cavity modes just as in the case for a CW laser. When the cavity transmitted light is frequency resolved using a grating or some other forms of dispersion, the information about the cavity finesse, and thus the intra-cavity loss, is obtained simultaneously across the entire spectrum of the comb [37].

A set of measurements using fast sweeping of the comb frequencies and a grating disperser after the cavity are shown in Fig. 3.4. Here, a frequency comb from a mode-locked erbium fiber laser was used to couple into a cavity constructed

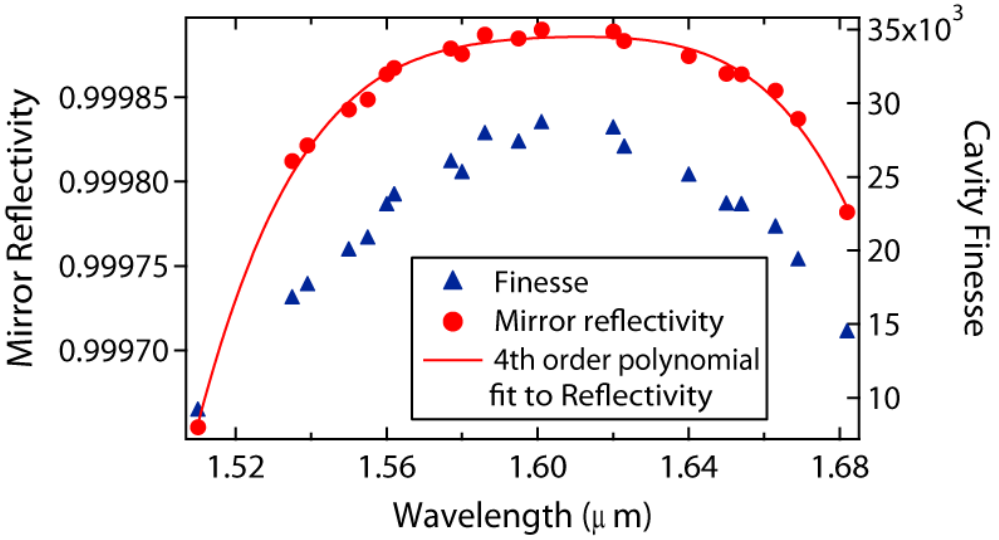


Figure 3.4: The finesse, and the corresponding cavity mirror reflectivity, of an optical enhancement cavity spanning from 1.51 to 1.68 $\mu$m measured by a mode-locked $Er^{+3}$ fiber laser using frequency-resolved cavity ring-down spectroscopy.

from two mirrors with peak reflectivity at 1.6 $\mu$m [76]. A grating was used in cavity transmission to provide a 1-nm spectral resolution. A beam splitter was used to direct a portion of the cavity transmission to an optical spectrum analyzer for wavelength calibration of the ring-down measurements. This cavity, used in the trace detection experiments presented in Chapter 7, has a peak finesse of 28,000 and a spectral bandwidth of nearly 200 nm.

## 3.3 Cavity mode frequencies and dispersion

The dispersion of an optical cavity is important, especially for frequency comb-based spectroscopy, as it determines the spectral bandwidth over which the cavity modes and the comb components can be overlapped simultaneously. While the comb modes are evenly spaced in the frequency domain, $\nu_n = nf_r + f_o$, the cavity mode spacing is frequency-dependent. This is due to a variety of frequency-dependent phase shifts inside an optical cavity. The cavity schematic in

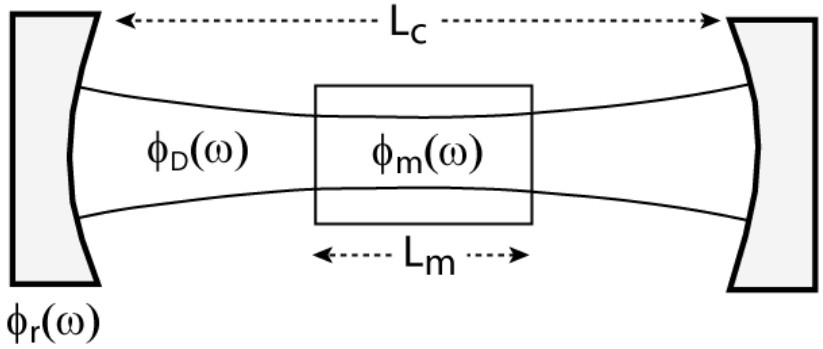


Figure 3.5: The total phase accumulated for a wave with frequency $\omega$ in one round-trip of an optical cavity with contributions from the mirror coatings, the intra-cavity media, free space propagation, and diffraction.

Fig. 3.5 shows several sources of frequency-dependent phase shifts including the mirror phase shift $\phi_r(\omega)$, the diffraction phase shift $\phi_D(\omega)$, and the phase shift due to intra-cavity media $\phi_m(\omega)$ [109]. To derive an expression for the frequency-dependence of the cavity mode spacing, we begin by writing an expression for the phase shift accumulated during one round-trip inside the cavity

$$\phi_{rt}(\omega) = \frac{\omega}{c}(L_c - L_m) + \frac{\omega n_m}{c}(L_m) + \phi_D(\omega) + \phi_{mo}(\omega) + \phi_r(\omega). \tag{3.25}$$

Here, the phase accumulation inside the intra-cavity medium has been separated into a frequency-independent component, $\omega n_m L_m/c$, and a frequency dependent component, $\phi_{mo}(\omega)$. Cavity modes exist at frequencies where the round-trip phase is equal to a multiple of $2\pi$ such that

$$2\pi N = \phi_{rt}(\omega), \tag{3.26}$$

where $N$ is the mode number. The change in mode number as a function of frequency is found by taking the derivative of the mode number with respect to $\omega$

$$\frac{\partial N}{\partial \omega} = \frac{1}{2\pi}\left(\frac{L_c + L_m(n_m - 1)}{c} + \frac{\partial \phi_D}{\partial \omega} + \frac{\partial \phi_{mo}}{\partial \omega} + \frac{\partial \phi_r}{\partial \omega}\right). \tag{3.27}$$

The FSR is defined as the frequency interval between adjacent modes; therefore, setting $\Delta N = 1$ yields an expression for the frequency dependent mode spacing.

$$FSR(\omega) = \frac{c}{2L + c\frac{\partial\phi}{\partial\omega}\big|_{\omega}}, \tag{3.28}$$

where $L = L_c + L_m(n_m - 1)$ and $\partial\phi/\partial\omega$ is the combined derivative of all of the frequency-dependent phase terms inside the cavity. The degree to which the cavity FSR is wavelength (or optical frequency)-dependent is determined by the intra-cavity dispersion term $c(\partial\phi/\partial\omega)|_{\omega}$ [110][111][112][113].

Clearly, low intra-cavity dispersion is important for coupling a broad-bandwidth comb spectrum to respective cavity modes. Furthermore, precise characterizations of the intra-cavity dispersion are essential for the cavity filtered detection scheme described in Section 6.4.1. For now we describe a method of using the frequency comb itself to precisely measure the intra-cavity dispersion. We will discuss the application of these measurements in later sections.

A schematic of the comb-based cavity dispersion measurement is shown in Fig. 3.6. The comb acts as a frequency ruler to determine the cavity mode structure and the wavelength-dependent FSR. First, $f_r$ of the laser is detuned away from the cavity FSR at 800 nm as shown in Fig. 3.6b. A frequency discrimination signal between the cavity modes and frequency combs is recovered and serves to lock the comb to the cavity near the edge of the cavity-comb spectrum (830 nm in this case). We will present a detailed discussion of cavity-comb locking schemes in Chapter 4. For now, we note that an electro-optic modulator was used to generate sidebands on the comb and a Pound-Drever-Hall error signal was used to lock the comb to the cavity [4]. The locking wavelength becomes a reference from which the cavity FSR is compared to the laser $f_r$. As one gradually moves away from 830 nm to other parts of the comb spectrum, the corresponding comb components will spectrally walk away from their respective cavity resonance modes. However,

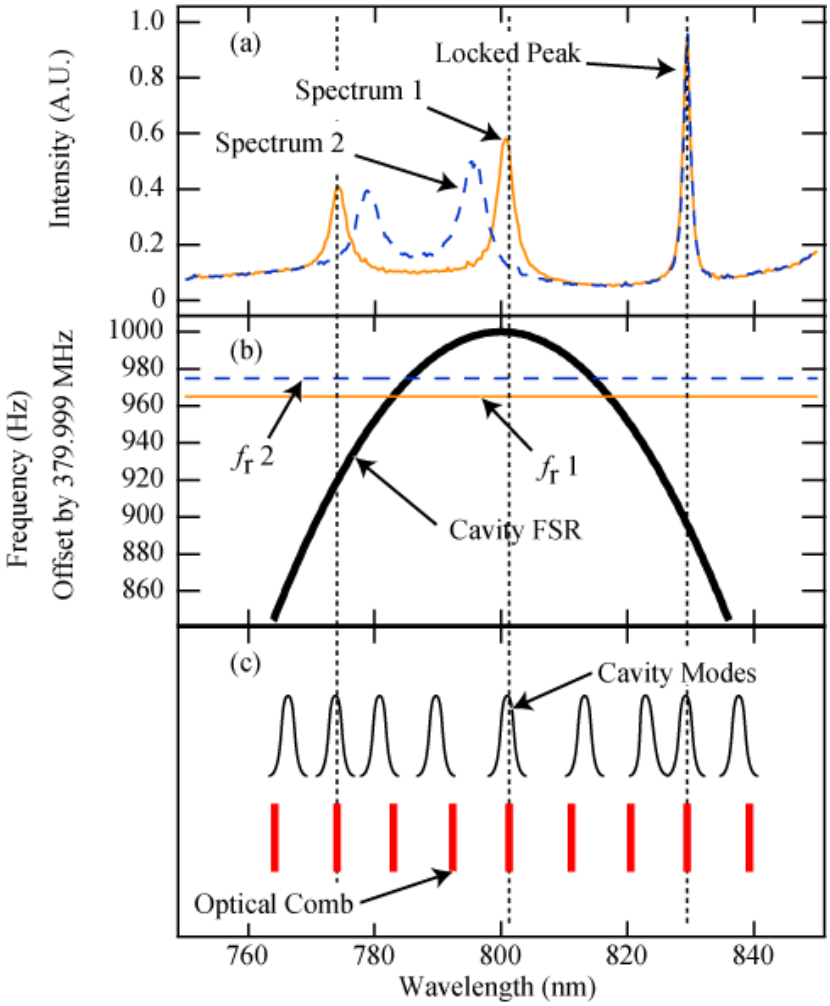


Figure 3.6: A technique for using the frequency comb for measuring intra-cavity dispersion. (a) The cavity transmission spectrum for two values of $f_r$, showing the spectral regions where the comb modes and cavity modes overlap. While comb-cavity mode overlap is forced at the locking wavelength near 830 nm, the other cavity transmission peaks arise from the frequency dependence of the cavity FSR. (b) The frequency dependent cavity FSR and values of $f_r$ that give rise to the transmission spectra in (a). (c) A schematic of the cavity and comb modes for the case of Spectrum 1 in (a), illustrating that cavity transmission peaks occur only where there is overlap between the cavity and comb modes.

after a sufficiently large spectral gap, a set of comb lines will again come on resonance with cavity modes. Overlaps between the comb frequencies and cavity modes that lead to cavity transmissions are schematically illustrated in Fig. 3.6c. A spectrometer is used to measure the wavelength-resolved intensity of the light

transmitted from the cavity, as shown in Fig. 3.6a for two different values of $f_r$.

The frequency separation between the $m^{th}$ cavity mode and the $m^{th}$ comb component from the locking point (830 nm) can be determined by the walk-off integral [112],

$$\Delta\nu_m = \int_{n_l}^{n_p} \big[FSR(n_c) - f_r(n_p)\big] dn_c. \tag{3.29}$$

Here, FSR($n_c$) is the frequency-dependent cavity FSR corresponding to cavity mode number $n_c$. $\Delta\nu_m$ is the frequency gap between the m$^{th}$ comb component and the m$^{th}$ cavity mode from the locking wavelength where $m = n_l - n_p$. $n_l$ is the mode number of the cavity that is locked to the comb. $n_p$ is the mode number of the comb tooth where the frequency difference between comb and the cavity mode is $\Delta\nu_m$. Finally, $f_r(n_p)$ is the repetition frequency of the comb that leads to a frequency difference $\Delta\nu_m$ between the comb and cavity at comb mode $n_p$. When $\Delta\nu_m = kf_r$ ($k$ = ..., -2, -1, 0, 1, 2, ...), the $m^{th}$ comb frequency overlaps with the $(m+k)^{th}$ cavity mode. This comb component then appears as a peak in the cavity transmitted spectrum.

$$(n_p - n_c) f_r(n_p) = \int_{n_l}^{n_p} \big[FSR(n_c) - f_r(n_p)\big] dn_c. \tag{3.30}$$

The walk-off integral can be changed into an integral over frequency by converting the mode numbers into their corresponding frequency values.

$$\Delta n f_r(\nu_p) = \int_{\nu_l}^{\nu_p} \big[FSR(\nu) - f_r(\nu_p)\big] \frac{d\nu}{f_r}. \tag{3.31}$$

Here, $\Delta n$ refers to the mode number slippage between the cavity and comb over the frequency interval $\nu_l$ to $\nu_p$. Since $f_r$ is a constant, this part of the frequency integral can be evaluated directly

$$\int_{\nu_l}^{\nu_p} FSR(\nu) d\nu = f_r(\nu_p)[\nu_p - \nu_l] + \Delta n f_r^2(\nu_p). \tag{3.32}$$

Finally, we use the fundamental theorem of calculus $F(b) - F(a) = \int_a^b f(x)dx$ followed by a derivative with respect to $\nu_p$ to arrive at a differential equation that

relates the frequency dependent cavity FSR to the frequencies of the peaks in the cavity transmission spectrum,

$$FSR(\nu_p) = f_r(\nu_p) + \frac{\partial f_r(\nu_p)}{\partial \nu_p}[\nu_p - \nu_l] + 2\Delta n f_r(\nu_p)\frac{\partial f_r(\nu_p)}{\partial \nu_p}. \tag{3.33}$$

With the laser locked to the cavity at 830 nm, $f_r$ is scanned and the wavelength values of the cavity transmission peaks are recorded for each value of $f_r$. Using Eq. 3.33, the values of $f_r$ that give rise to cavity transmission peaks at frequencies $\nu_p$ are used to determine the frequency dependance of the cavity FSR. Finally, a simple equation

$$GDD(\nu) = \frac{d}{d\nu}\frac{1}{FSR(\nu)} \tag{3.34}$$

is used to calculate the intra-cavity group-delay-dispersion from the frequency dependent cavity FSR. Fig. 3.7 shows a measurement of the intra-cavity dispersion for an evacuated two-mirror cavity centered at 800 nm using a Ti:Sapphire frequency comb. With this level of dispersion, the comb frequencies and cavity modes can be made to overlap over a spectral window of about 30 nm. However, this cavity has high finesse for a spectral window covering 100 nm. In the next

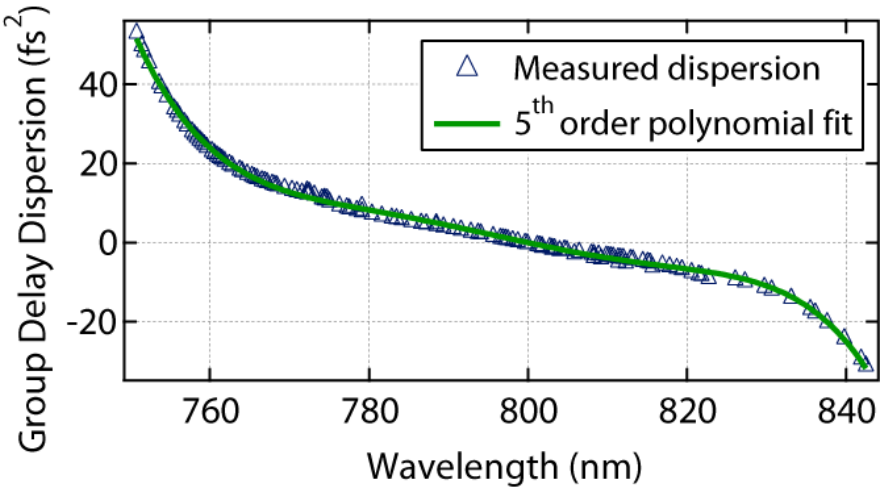


Figure 3.7: Measurement of the dispersion of a two-mirror cavity with peak reflectivity at 800 nm, using the comb-based cavity dispersion measurement technique.

chapter, we will discuss techniques for coupling the comb to the cavity that allow us to take advantage of the entire 100 nm spectral bandwidth of the cavity finesse.

The precision of this dispersion measurement technique is directly related to the cavity linewidth. Higher finesse leads to more sharply peaked features in cavity transmission and reduced uncertainties in the determination of the center wavelength of the transmission peak. In the example shown in Fig. 3.7, the cavity under measurement had a finesse of 3000, an FSR of 380 MHz, and the achieved experimental precision for intra-cavity dispersion measurement was better than 1 $fs^2$.

# Chapter 4

## Cavity-comb coupling

In this chapter we discuss techniques that are used to couple, and more importantly stabilize the coupling of, the optical comb frequencies to the resonant modes of an optical cavity. Three techniques will be discussed including (1) a tight lock of the comb components to the cavity modes, (2) a low-amplitude, fast sweep of the comb components over the cavity modes, and (3) precision scan between initially mismatched FSR and $f_r$ such that one comb component leaks out of the cavity at a time. Each of these techniques offers different benefits and limitations for performing CE-DFCS. Practical applications will dictate the choice for the right approach.

For instance, a tight lock is preferred when using a modulation spectroscopy technique such as NICE-OHMS [114] or velocity modulation spectroscopy [115] [116] in conjunction with CE-DFCS. This is because the continuous presence of the cavity transmitted beam leads to long measurement times while the modulation acts to separate the intensity noise of the cavity transmitted beam from the absorption signal. So far, there have been no efforts to marry the CE-DFCS technique with NICE-OHMS, however, a CE-DFCS and velocity modulation hybrid system is currently under development in Eric Cornell's lab to map the transitions in the $HaF^+$ molecular ion. In cases where the is no modulation applied to the absorption measurements, the sweep method is preferred because it reduces inten-

sity noise, thereby yielding a higher signal to noise ratio (S/N) for measurements of the cavity transmitted beam. This technique was used for all of the CE-DFCS measurements presented in Chapter 7. Finally, a precision scan of mismatched FSR and $f_r$ can be used to achieve high spectral resolution of the absorption measurements without the use of a high resolution spectrometer in cavity transmission. An example of this type of measurement is presented in Section 6.4.1.

## 4.1 Optimizing the coupling of a frequency comb into an optical cavity

Before discussing the details of the various techniques available for coupling a frequency comb to an optical cavity, we will spend a moment reviewing the basics of optical cavity alignment. This section will cover mode-matching, alignment of the incident laser beam to the cavity mode, and finding the values of the laser $f_r$ and $f_o$ that lead to overlap of the comb frequencies with the resonant cavity modes.

### 4.1.1 Mode-matching of the laser beam to the cavity

The first thing to consider when coupling a laser beam (frequency comb or otherwise) to an optical cavity is mode matching. Mode-matching refers to the practice of using one or several lenses to match both the radius and wavefront curvature of the incident laser beam to a transverse eigenmode of the optical cavity (Fig. 4.1). The transverse cavity eigenmode used for this discussion, and in all other experiments described in this thesis, is the $TEM_{00}$ mode.

To decide which lenses should be used and where to place them relative to the laser and optical cavity, it is first necessary to know the beam parameters for the both the laser beam and the cavity eigenmode. The beam parameters consist

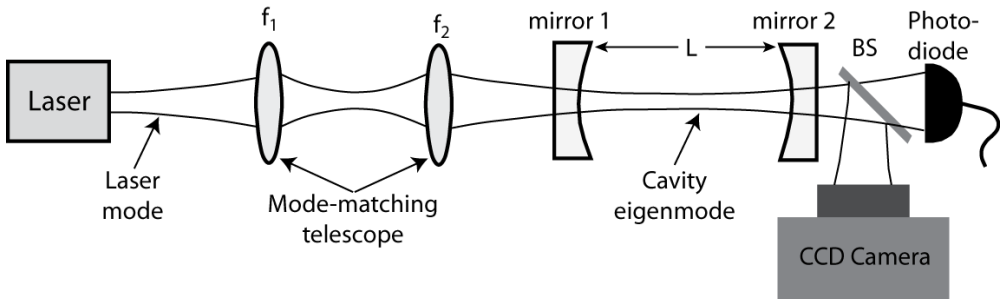


Figure 4.1: Mode-matching schematic showing how two lenses are used to match the size and wavefront curvature of an incident laser beam to a cavity eigenmode, thereby efficiently coupling the laser beam into the cavity. The laser is aligned such that the axis of the laser beam is collinear with the axis of the cavity eigenmode. A photodiode and/or CCD camera can be used in cavity transmission to observe and optimize both the mode-matching and alignment of the laser beam to the cavity.

of the position of the beam focus and the Rayleigh range of that focus. The $\mathrm{TEM}_{00}$ cavity eigenmode parameters are calculated using the so-called ABCD matrices [117][118]. For the cavity shown in Fig. 4.1, the ABCD matrix for a complete cavity round-trip starting from the intra-cavity focus is

$$\begin{pmatrix} A & B \\ C & D \end{pmatrix} = \begin{pmatrix} 1 & \frac{L}{2} \\ 0 & 1 \end{pmatrix} \begin{pmatrix} 1 & 0 \\ -\frac{2}{R} & 1 \end{pmatrix} \begin{pmatrix} 1 & L \\ 0 & 1 \end{pmatrix} \begin{pmatrix} 1 & 0 \\ -\frac{2}{R} & 1 \end{pmatrix} \begin{pmatrix} 1 & \frac{L}{2} \\ 0 & 1 \end{pmatrix} \tag{4.1}$$

$$= \begin{pmatrix} \frac{2L^2-4LR+R^2}{R^2} & \frac{L(L^2-3LR+2R^2)}{R^2} \\ \frac{4(L-R)}{R^2} & \frac{2L^2-4LR+R^2}{R^2} \end{pmatrix}. \tag{4.2}$$

Here, R is the radius of curvature of both cavity mirrors and L is the cavity length. The q-parameter of the cavity, contains information about both the position of the beam focus (the real part of q) and the Rayleigh range of the focus (the imaginary part of q) according to

$$q(z) = z - iz_0. \tag{4.3}$$

The Rayleigh range is related to the wavelength ($\lambda$) and the radius ($w_o$) of the focused beam by

$$z_0 = \frac{\pi w_o^2}{\lambda}. \tag{4.4}$$

The q-parameter for the $TEM_{00}$ eigenmode of the cavity is found from the round trip ABCD matrix using the self consistency relationship

$$q = \frac{Aq + B}{Cq + D} \tag{4.5}$$

Using Eq. 4.5 one can quickly determine if a given cavity geometry will have a stable $TEM_{00}$ mode and what the beam parameters of that mode will be [117].

The laser beam parameters are found by measuring the laser mode diameter at two different distances from laser. This can be done using a beam profiler, or more primitively, a razor blade on a translation stage and a power meter. Once the beam diameters at the two positions have been determined, the position of the laser beam waist and the Rayleigh range are found by solving the following system of equations

$$W(z_1) = \sqrt{\frac{\lambda z_o}{\pi}} \left[ 1 + \left( \frac{x + z_1}{z_o} \right)^2 \right]^{-1/2}, \tag{4.6}$$

$$W(z_2) = \sqrt{\frac{\lambda z_o}{\pi}} \left[ 1 + \left( \frac{x + z_2}{z_o} \right)^2 \right]^{-1/2}.$$

Here, $W(z_1)$ and $W(z_2)$ are the $1/e$ electric field radii of the laser beam measured at distances $z_1$ and $z_2$ from an arbitrary reference point. $x$ is the distance from the reference point to the laser beam waist, and $z_o$ is the Rayleigh range of the beam waist.

Once the laser and cavity eigenmode beam parameters are known, the laser beam can be mode-matched to the cavity mode as shown in Fig. 4.1. Unfortunately, there is no closed-form solution for selecting the focal lengths and the positions of the mode-matching lenses. This should make intuitive sense as one would expect that several combinations focal lengths and lens positions will yield successful mode-matching. To find a suitable set of lenses and positions, one typically uses some sort of computer search algorithm. One particularly nice tool for

this purpose is the MATLAB genetic algorithm tool [119]. Example code for using this tool to mode-match a laser beam with a known $q$-parameter to a two mirror symmetric cavity is provided in Appendix A. Since lenses are only available in a limited number of focal lengths, it is useful to specify the available focal lengths in the search program. It is also useful to set limits on the distances between the lenses and between the laser and the cavity based on the area available on the optical table.

Once a set of focal lengths and positions for the mode-matching lenses has been found, the solution should be verified on the optical table. With lenses in position, the laser beam should come to a focus at the position of the intra-cavity focus. This can be checked by removing the cavity mirrors and observing the beam as it passes through the region of the intra-cavity focus. If there is some problem, and the beam does not come to a focus in this region, double-check your calculations of the cavity eigenmode and the laser beam parameters. For instance, when measuring the laser beam width, it is quite easy to forget that the result of the measurement is the $1/e$ point of the beam intensity and not the electric field.

### 4.1.2 Alignment of the laser to the cavity modes

With the mode-matching telescope successfully installed, it is time to align the propagation axis of the laser beam to the axis of the cavity mode. For this task, it is useful to have a CCD camera in cavity transmission as shown in Fig. 4.1. At the very least, a photo-detector is required to observe the resonant cavity modes. At this point a slow ($< 100$ Hz) modulation should be applied to either the cavity length or the laser $f_r$ so that when the cavity-comb coupling becomes close to optimal, it will be possible to observe the resonances in cavity transmission. It is best to apply a length modulation that is larger than $\lambda/2$ so that at least one

entire FSR will be observed in cavity transmission. The laser beam should be aligned to the detector in cavity transmission with the cavity mirrors removed from their mounts. Once the beam is aligned, the rear cavity mirror (mirror 2 in Fig. 4.1) is placed in its mount and aligned such that the laser beam is perfectly retro-reflected. Next, mirror 1 is placed in its mount and is also aligned such that the laser beam is perfectly retro-reflected. At this point, it should be possible to see faint cavity modes using the CCD camera. If so, the image from the CCD can be used to align the laser beam to the cavity such that the $\text{TEM}_{00}$ is the most prominent mode in cavity transmission. If a CCD is not used, or no image can be seen, it may be necessary to adjust the cavity length or the laser $f_r$ such that $f_r \approx$ FSR before continuing with the laser beam alignment.

### 4.1.3 Matching the laser $f_r$ and $f_o$ to the cavity modes

One of the biggest differences between coupling a frequency comb versus a CW laser to an optical cavity is that efficient coupling of a frequency comb requires that $mf_r \approx$ FSR, where $m$ is an integer. Unfortunately, this requirement is a bit troublesome since there is nearly no signal in cavity transmission until $mf_r \approx FSR$. Fortunately, there are a couple of tricks that work pretty reliably for achieving coupling. The first trick involves a bit of blind faith: if you believe that the laser beam is reasonably well aligned to the cavity then you can try to scan either $f_r$ or the cavity FSR and look for resonances in cavity transmission. If the cavity finesse is not too high ($< 10,000$) and the laser power is larger than a few milliwatts this approach will work most of the time. However, if the laser power is too low, the finesse is too high, the mirrors are dirty, or you're just having an off day and you can't find the modes, you can try knocking the laser out of mode-locking. With the laser operating in CW mode, it will be possible

to see resonance in cavity transmission regardless of the cavity length. Using the CW resonances as a guide, the alignment of the laser beam to the cavity can be optimized. When the laser is once again mode-locked you can scan the laser $f_r$ and be certain that the laser beam has a good spatial overlap with the cavity mode. Another trick that is sometimes used to make aligning the beam easier is spectral broadening. Highly nonlinear fiber or a Raman shifting medium can be used to generate wavelengths that are outside of the reflectivity bandwidth of the mirrors. The wavelengths corresponding to low mirror reflectivity will pass nearly unattenuated through the cavity making it easy to see the low-spectral-resolution fringes in cavity transmission when the incident beam is aligned with the cavity mode.

Once the cavity transmission resonances have been found, the laser beam alignment, mode-matching, $f_r$ and $f_o$ can be tuned to optimize the coupling between the comb and the cavity. Guidelines for how to tune these quantities based on the structure of the resonances observed in cavity transmission are shown in Fig. 4.2. The situation of optimal coupling of the comb to the cavity is shown in Fig. 4.2a. In this case, only the $\mathrm{TEM}_{00}$ appears in cavity transmission. Also, the value of $f_o$ is set such that the height of the $f_r = \mathrm{FSR}$ resonance is maximized. This occurs when the $f_r = (1 \pm 1/n)\mathrm{FSR}$ resonances have equal amplitude, where $n$ is the comb mode number at the center of the cavity transmitted spectrum. Figures 4.2 b) and c) provide examples of non-optimal coupling: b) shows the cavity transmission when $f_o$ is not optimized resulting in a lower signal for the $f_r = \mathrm{FSR}$ resonance and unequal amplitudes for the $f_r = (1 \pm 1/n)\mathrm{FSR}$ resonances, while c) shows the laser beam misaligned and/or poorly mode-matched to the cavity resulting in the appearance of higher order transverse modes [120].

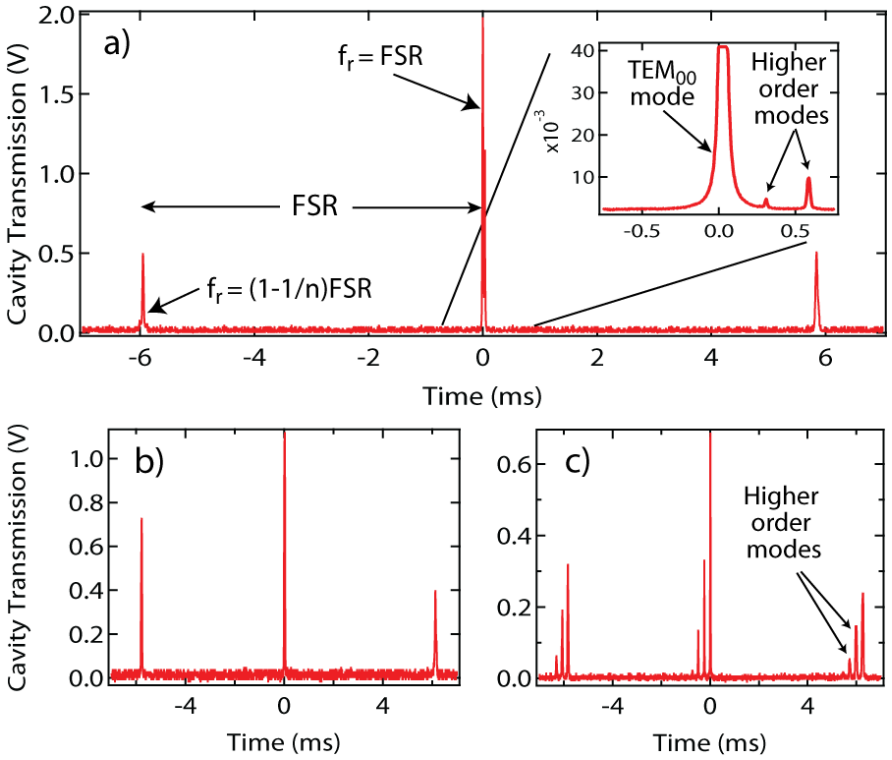


Figure 4.2: a) Optimized coupling of a frequency comb to an optical cavity. The prominent $f_r$ = FSR mode is surrounded by smaller and equally sized $f_r = (1 \pm 1/n)$FSR modes indicating that the laser $f_o$ optimally matches the evolution of the incident laser pulse phase to the phase evolution of the intra-cavity pulse. The inset shows that good mode-matching and the laser beam alignment result in higher order modes that are suppressed by a factor of 200 compared to the TEM$_{00}$. b) and c) show examples of non-optimal coupling. In b) the value of $f_o$ is set incorrectly resulting in $f_r = (1 \pm 1/n)$FSR modes that differ in height and a less prominent $f_r$ = FSR mode. In c) the laser beam is poorly aligned and/or mode-matched to the cavity resulting in prominent higher order mode structure and a reduced TEM$_{00}$ signal.

## 4.2 Comb locked to cavity

With the frequency comb optimally aligned and mode-matched to the cavity, it is natural to think of ways to stabilize the coupling of the comb to the cavity. The most intuitive method of stabilization is to maintain a precise and simultaneous overlap of all of the comb frequencies with corresponding cavity modes (Fig. 4.3). To perform this type of coupling, the laser cavity must main-

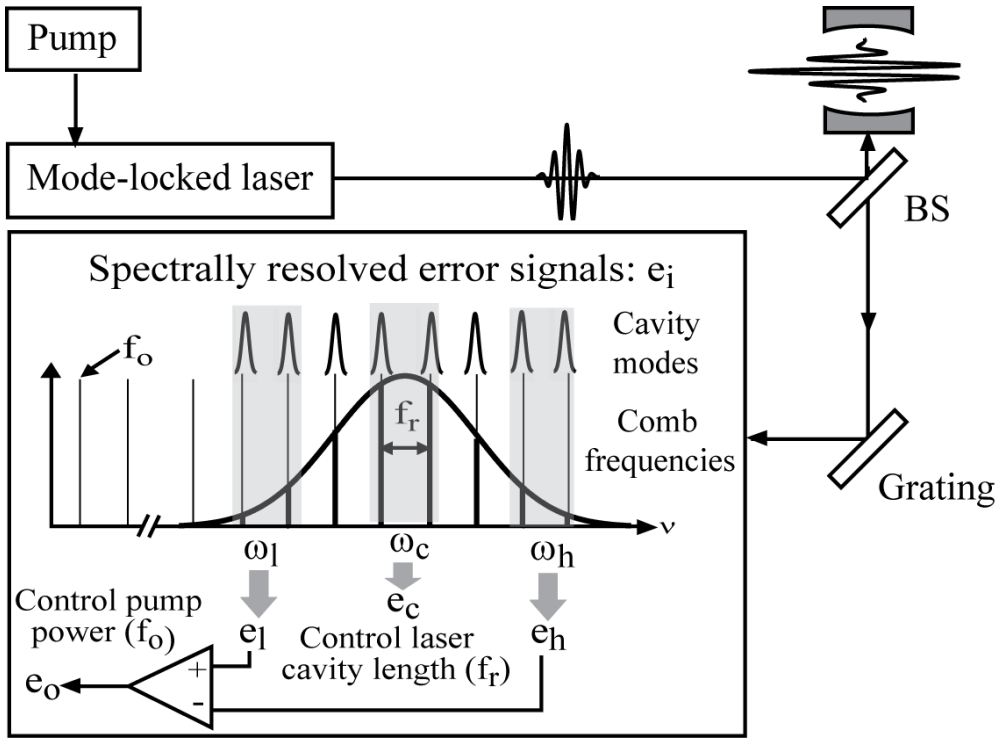


Figure 4.3: A frequency comb can be locked to an optical cavity by generating spectrally resolved cavity-locking error signals. An error signal at the center frequency is used to lock a collection of comb modes at $\omega_c$ to be on resonance with their respective cavity modes. Error signals at the high ($\omega_h$) and low ($\omega_l$) ends of the comb spectrum can be used to maintain a correct value of $f_o$. Adjustment of $f_o$ and $f_r$ (via the optical lock at $\omega_c$) ensures an optimal overlap of the comb and cavity modes over a wide spectral bandwidth.

tain an integer multiple of the intra-cavity optical path length (i.e. FSR = $mf_r$). Furthermore, the value of $f_o$ must be correct such that the comb frequencies are overlapped with the cavity modes. Finally, the dispersion of the optical cavity must be sufficiently low to ensure a large number of comb modes overlap with their corresponding cavity modes.

For a broadband frequency comb, two servo loops are needed to lock the comb to a cavity [53][54][55], one for $f_r$ and the other for $f_o$. The two servo error signals are generated through spectrally resolved detection of the cavity-comb interaction as shown in Fig. 4.3. For a robust lock, there are several schemes that

can be used to derive error signals including: a dither-lock modulation scheme, a Pound-Drever-Hall (PDH) modulation scheme [4], or a Hänsch-Couillaud polarization scheme[3]. Typically, we use a modulation/lock-in detection approach. For example, an EOM can be used to place modulation sidebands on the frequency comb to implement the PDH scheme, or the cavity length can be dithered rapidly to derive a dither lock error signal. A collection of comb modes at the center of the spectrum is detected, after their interaction with the corresponding cavity modes. This generates an error signal that is used to lock the optical comb frequencies to the cavity modes by acting on $f_r$. The interaction of the high and low frequency ends of the comb spectrum with the cavity can be used to lock $f_o$ to the value that results in the maximum spectral bandwidth coupled into the optical cavity. These two loops act together to optimize the coupling between the comb and cavity.

Figure 4.4 shows the spectrum of an incident frequency comb and the spectrum transmitted from the optical cavity ($\mathcal{F} = 2500$) when the comb frequencies are tightly locked to the cavity modes. This cavity contained a 600 $\mu$m intracavity Brewster plate made of sapphire that was dispersion compensated with a -40 $fs^2$ negative dispersion mirror. Due to the dispersion compensation, 30 nm of spectrum are efficiently coupled into the cavity with minimal filtering of the incident comb spectrum due to frequency mismatch of the comb frequencies and cavity modes.

The main benefit of locking the comb to the cavity is that the optical power transmitted through the cavity is nearly that of the incident beam for the case of a well impedance-matched cavity. Furthermore, the cavity transmission is continuously present. These two features result in a high transmitted power and fast averaging of the intensity noise. The largest drawback is that the spectral bandwidth of the comb that is coupled into the cavity is typically limited to $< 10\%$ of the center frequency, due to mirror dispersion. Also, the continuous coupling

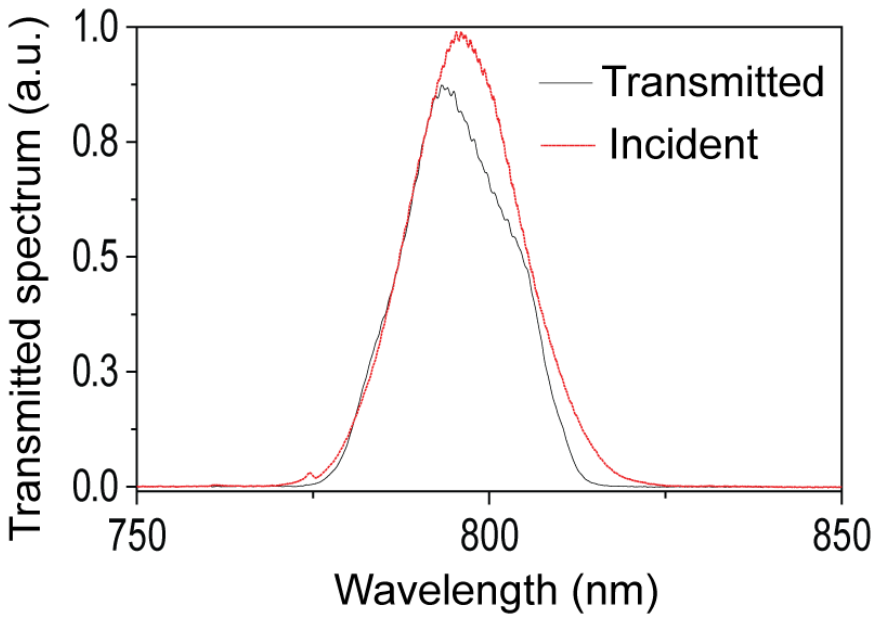


Figure 4.4: The spectrum of a Ti:Sapphire laser frequency comb spectrum (red) incident on an optical cavity. The spectrum transmitted from the cavity when the comb frequencies are locked to the cavity modes (black). The cavity transmission shows that 30 nm of comb spectrum centered at 800 nm are coupled into the cavity with a minimal amount of filtering due to frequency mismatch of the cavity modes and comb frequencies.

of the comb to the cavity is very sensitive to acoustic and vibration-induced frequency noise, which gets converted to a substantial amount of intensity noise on the cavity transmission if the servo loops do not have sufficient feedback bandwidth.

## 4.3 Comb swept around cavity

The second method for stabilizing the coupling of the comb frequencies to cavity modes involves a periodic injection of the comb into the cavity. This is accomplished by introducing a low-amplitude, high-frequency sweep between the corresponding modes of the cavity and the comb [121] [112]. This type of cou-

pling has several advantages and some drawbacks compared to directly locking the comb to the cavity.

The first advantage is that the requirement on the intra-cavity dispersion is relaxed. Since the comb and cavity modes are being swept over each other, it is no longer required that all of the comb and cavity modes are exactly overlapped simultaneously. Instead, different modes are allowed to come on resonance at slightly different times, thus increasing the useful spectral bandwidth that is recovered in cavity transmission. With a reasonably low dispersion, high finesse, and fast frequency sweeping, the time it takes for different comb modes to come on resonance with the cavity can be shorter than the cavity lifetime. For the example in Fig. 4.5, 100 nm of comb spectrum centered at 1.55 $\mu$m is swept over the cavity modes. Due to low intra-cavity dispersion and optimal matching of the comb to the cavity, all comb frequencies come onto resonance with the cavity at nearly the same time. Under these conditions, the cavity transmission signal is sharply peaked. The amplitude of the frequency sweep can be made very small such that the comb is on resonance with the cavity for a large fraction of the sweep time. By using the smallest possible sweep amplitude, the power contained in the cavity transmission is maximized.

Another advantage of sweeping over the resonance is that it largely avoids intensity noise on the cavity transmitted beam. Under the locked condition, mechanical vibration-induced cavity length fluctuations cause amplitude noise on cavity transmission, which can place a limit on the detection S/N of the transmitted beam. However, by sweeping at rates larger than the Fourier frequencies of dominant mechanical noise processes, the intensity noise of cavity transmission is drastically reduced.

The final advantage of sweeping is the ease of maintaining the desired coupling between comb and cavity modes. In this case, the servo only has to stabilize

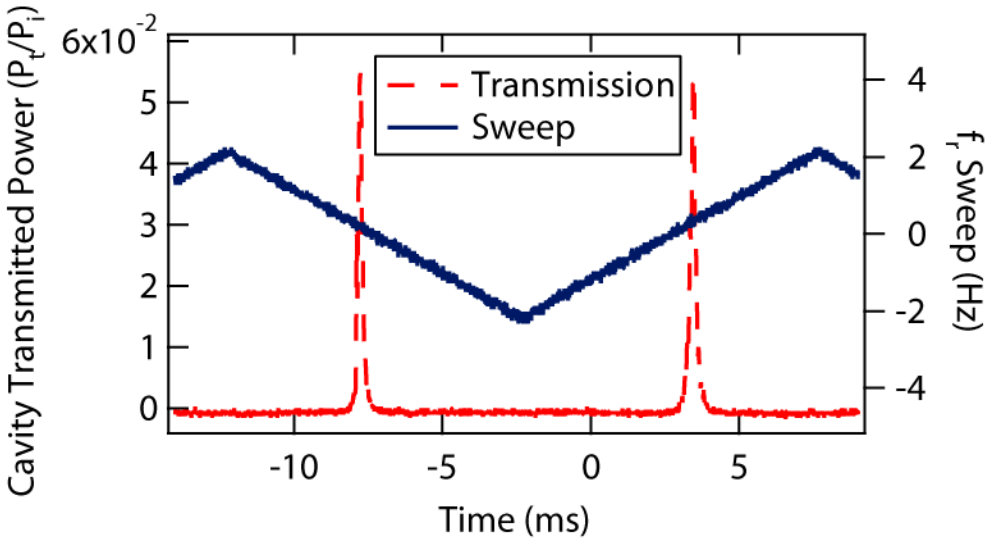


Figure 4.5: Cavity transmission for a 100 nm input spectrum coupled to a $\mathcal{F}$ = 28,000 cavity. Due to low dispersion and optimal cavity-comb matching, the entire 100 nm incident spectrum becomes resonant with the cavity at nearly the same time during a frequency sweep.

the time at which the comb modes come onto resonance with the cavity modes during the sweep cycle. As a result, a low bandwidth servo acting on the cavity length or laser length is sufficient for maintaining a constant sweep-based comb-cavity coupling. An example of this type of servo is given in Fig. 4.6. The cavity transmission is compared against a preset DC threshold in a comparator, generating a train of pulses that indicate when the comb is resonant with the cavity. These pulses become the 'clock' input for a subsequent D-flip flop. The 'D' input of the flip flop is provided by a TTL synchronization signal for the sawtooth sweep waveform. The output is high when sawtooth is increasing in amplitude and low when it is decreasing. The output of the flip flop can then be integrated to indicate the separation between successive cavity transmission peaks. A DC offset voltage can then be used to lock the separation of successive cavity transmission peaks to any desired value. Using this servoing scheme, $f_o$ is measured either by the interaction of the comb with the cavity, or by $f$ - $2f$ interferometry. Typically,

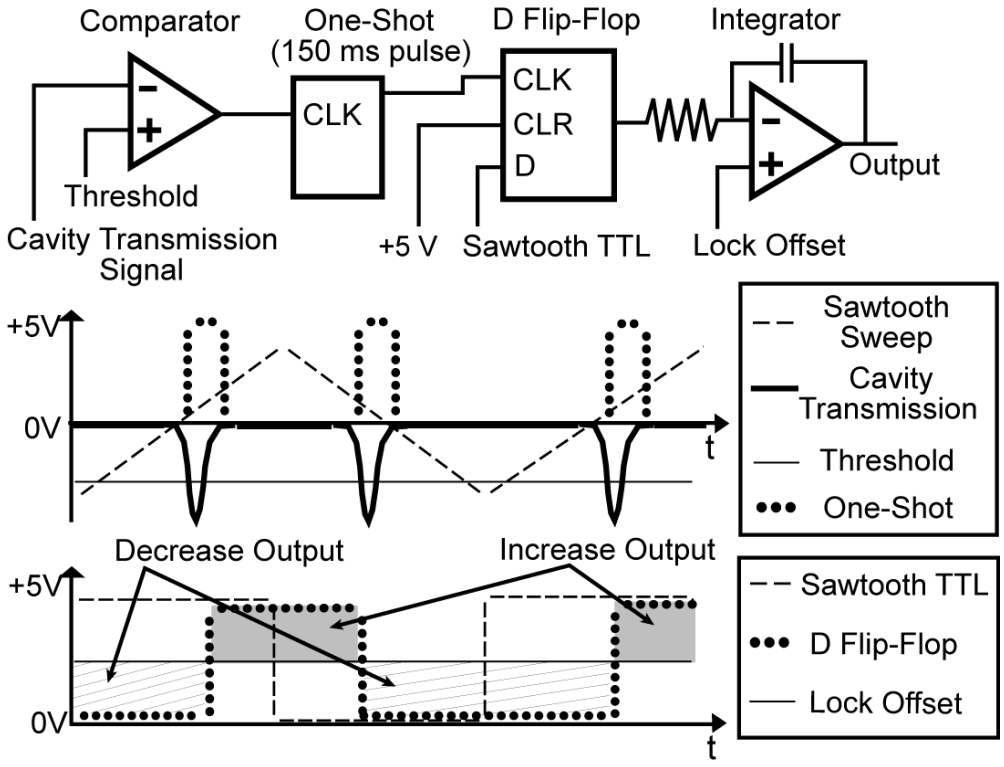


Figure 4.6: A schematic of the servo used to maintain the position at which the comb and the cavity come onto resonance during each sweep cycle.

the value of $f_o$ drifts quite slowly such that infrequent measurements, once every several minutes, can be made to maintain the value that optimizes the coupling of the comb to the cavity.

The primary disadvantage of sweep-based coupling is the loss of duty cycle for cavity transmission measurements. Making a faster sweep reduces the intensity noise, but the power transmitted through the cavity is also reduced. Therefore, it is necessary to choose an optimum sweep rate that maximizes the overall S/N of the cavity transmission by making a compromise between the intensity noise and the transmission power. For systems implemented in our lab, the optimal sweep rate is typically 1-2 kHz, such that the cavity is allowed to build-up intensity for $\sim$1/10 $\tau_{cavity}$. Of course, the optimal settings depend on the bandwidth of the sweep actuator, the vibrational mode frequencies of the laser and cavity length,

and the degree of isolation of the cavity and laser from mechanical vibrations of their environment. Less mechanical noise allows for a longer intra-cavity build-up time and higher optical power in the cavity transmitted beam.

## 4.4 Precision sweep of laser $f_r$

The final method of coupling the comb to cavity involves purposely mismatching the cavity FSR and the laser $f_r$. The comb modes are then swept precisely through successive cavity modes such that the cavity acts as a frequency filter in transmission, allowing one or a handful of comb components to be transmitted at a time. This allows serial detection of individual frequency comb components across the comb spectrum [122][123].

To illustrate this approach, we demonstrate the measurement of the spectrum of our mode-locked fiber laser using two distinctly different methods. Figure 4.7a displays the spectrum of the mode-locked laser recorded by a traditional optical spectrum analyzer. In comparison, Fig. 4.7b shows the cavity transmission signal when the laser $f_r$ is detuned from its optimal value for coupling to the cavity and then scanned with respect to the cavity modes. For this measurement, the cavity had an FSR of 396 MHz and the laser had an $f_r$ of 99 MHz, such that $4 \times f_r \approx FSR$. The scan of the laser $f_r$ in Fig. 4.7b lasted about 20 ms, and the resulting cavity transmission signal recorded over this time interval closely resembles the optical spectrum of the mode-locked laser. The optical frequency resolution and spectral bandwidth provided by the cavity filtering scheme are determined by the the detuning of the laser $f_r$ from its optimal value for coupling to the cavity ($\delta f = mf_r - FSR$), the cavity FSR, and the cavity linewidth ($\Delta\nu$).

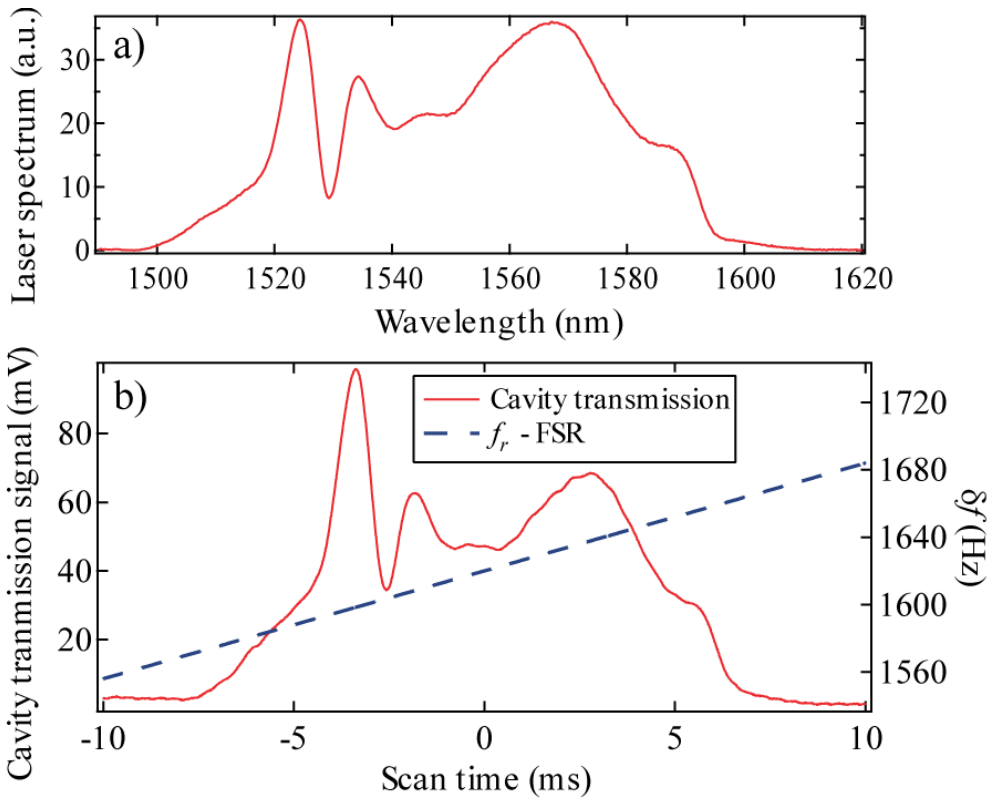


Figure 4.7: a) The optical spectrum of a mode-locked $Er^{+3}$ fiber laser measured with an optical spectrum analyzer. b) The cavity transmission signal as a function of the laser detuning $\delta f$ form the cavity FSR. The resulting cavity transmission signal recorded over time is not sharply peaked, but rather resembles the original spectrum of the mode-locked laser source.

The resolution is given by

$$resolution = \Delta\nu \quad \text{for} \quad \Delta\nu < |\delta f|, \tag{4.7}$$

or

$$resoltuion = \frac{\Delta\nu}{|\delta f|} FSR \quad \text{for} \quad \Delta\nu > |\delta f|. \tag{4.8}$$

The first scenario corresponds to the case where only one comb mode is resonant with the cavity at a time while the second case gives the resolution when several adjacent comb modes are simultaneously resonant with the cavity.

The spectral bandwidth that can be achieved in a single scan is determined

by $\delta f$, FSR, $m$, and $f_r$. Figure 4.8 illustrates that if the comb is on resonance with the cavity at a particular frequency, $\delta f$ will initially cause the comb modes to become detuned from the cavity modes in the neighboring spectral region. However, after a frequency interval of

$$bandwidth = \frac{f_r}{|\delta f|} m f_r = \frac{m f_r^2}{|\delta f|} \tag{4.9}$$

the comb will once again become resonant with the cavity modes. This relation can be easily derived by noting that

$$N m f_r - f_r = N \times FSR, \tag{4.10}$$

where $N$ is the number of cavity modes between the two spectral regions where the comb is resonant with the cavity. Rewriting this expression yields an expression for $N$ in terms of $f_r$ and $\delta f$

$$N = \frac{f_r}{m f_r - FSR} = \frac{f_r}{|\delta f|}. \tag{4.11}$$

Equations 4.7, 4.8 and 4.9 can be used to determine the resolution and spectral bandwidth for the cavity transmitted signal in Fig. 4.7b. The 396 MHz FSR and the average finesse of 6300 in the 1.5 $\mu$m to 1.6 $\mu$m spectral region result in a cavity linewidth of $\Delta\nu = 63$ kHz. Since the repetition frequency detuning ($\delta f = 1620$ Hz), was much smaller than $\Delta\nu$, the resolution of the cavity transmitted beam, given by Eq. 4.8, is 15.4 GHz. The maximum spectral bandwidth that can be achieved using these parameters is 207 nm. The scan in Fig. 4.7b shows 130 nm or 63% of the available scan range.

Equations 4.7 through 4.11 describe the case where $f_r <$ FSR. In cases where FSR $> f_r$, such that $m$FSR $\approx f_r$, the substitutions FSR $\rightarrow f_r$ and $f_r \rightarrow$ FSR must be made for Eqs. 4.7-4.11 to be valid. In this case, $\delta f = f_r - m$FSR, the spectral bandwidth is mFSR$^2/|\delta f|$, and the resolution is $\Delta\nu f_r/|\delta f|$ when $\delta f < \Delta\nu$.

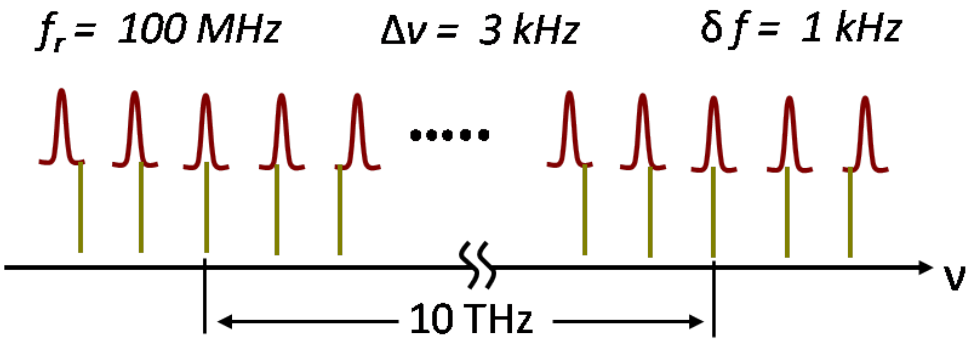


Figure 4.8: An example of the resolution (300 MHz) and spectral bandwidth ($f_r^2/\delta f$ = 10 THz) provided by cavity filtering for $f_r$ = 100 MHz, $\delta f$ = 1 kHz, and $\Delta\nu$ = 3 kHz.

When more than one spectral region is transmitted from the cavity at a time, there is no longer a unique mapping between scan time and the frequency in cavity transmission. To avoid ambiguity in such a case, a dispersive element with a coarse resolution (better than $mf_r^2/\delta f$) should be placed between the cavity transmission and the detector. To obtain a precise calibration of the cavity transmitted wavelength during a scan of $f_r$ requires that the frequencies of the cavity modes be known to high precision. For this, the dispersion measurement technique described in Section 3.3 can be used to provide a high precision measurement of the wavelength dependence of the cavity mode frequencies. Figure 4.8 illustrates the frequency domain picture of cavity filtering of a comb where $f_r$ = 100 MHz, $\Delta\nu = 3$ kHz, and $\delta f$ = 1 kHz.

To achieve the actual cavity-linewidth-limited spectral resolution for $\Delta\nu < \delta f$, the frequency difference between the cavity and comb modes needs to be stabilized to within the cavity linewidth. If the jitter of the cavity or comb modes is larger than the cavity linewidth, then the value of $\Delta\nu$ used for determining the resolution should be replaced with the frequency jitter. Since cavities used for sensitive detection can have linewidths in the kHz range, stabilizing the jitter be-

low this level is straightforward in a research laboratory but could be challenging in field applications.

Compared to the frequency sweep technique for coupling the comb to the cavity, the approach of precision $f_r$ scan typically uses slower sweep rates of the comb modes. It is therefore more susceptible to cavity-comb coupling noise arising from mechanical vibrations. Furthermore, this approach takes measurements in a serial manner, prolonging the measurement time. However, this technique does have the benefit of spectrally resolving the cavity transmitted signal without the need for an external spectrometer, a unique feature not shared by the two other coupling techniques.

# Chapter 5

# Measurement schemes

This chapter describes three measurement schemes that can be used to recover intra-cavity absorption information from the cavity transmitted beams. The two common methods are cavity-enhanced absorption spectroscopy (CEAS) and cavity ringdown spectroscopy (CRDS). In addition, CEAS can be implemented in two forms: steady-state or transient. The type of measurement that will be most convenient for a given CE-DFCS application depends on both the type of comb-cavity coupling that is implemented and the scheme for detecting the cavity transmitted beam that is used (see Chapter 6).

## 5.1 Cavity-enhanced absorption spectroscopy

CEAS refers to measurements of the intra-cavity absorption that are made by comparing the power transmitted through the cavity with and without absorption present. These measurements can be performed by either locking the comb to the cavity or by sweeping the comb frequencies over the cavity modes. For the purposes of this section, tightly-locked measurements will be referred to as steady state CEAS while measurements involving frequency sweep will be referred to as transient CEAS. As will be seen in the following section, the signal to noise ratio achieved in cavity transmission and thus the absorption sensitivity depends slightly on the type of CEAS that is implemented.

### 5.1.1 Steady-state CEAS

For steady state CAES measurments, the comb is locked to the cavity, allowing the intra-cavity power in each mode to reach steady state after several cavity lifetimes. For a single comb component that is on resonance with a cavity mode, the effect of absorption on the power of the light transmitted through the cavity is given by

$$\frac{P_t(\nu)}{P_{inc}} = \frac{T_1 T_2 e^{-\alpha(\nu)L}}{\left|1 - \sqrt{R_1 R_2} e^{-\alpha(\nu)L}\right|^2}. \tag{5.1}$$

Here $\mathrm{P}_t(\nu)$ is the transmitted power, $\mathrm{P}_{inc}$ is the power incident on the cavity, and $\mathrm{R}_{1,2}$ and $\mathrm{T}_{1,2}$ are the reflectivity and transmission of the cavity mirrors at frequency $\nu$. $L$ is the cavity length and $\alpha(\nu)$ is the frequency-dependent intra-cavity absorption [124][125]. In the limit that $\alpha(\nu)L \ll (1 - R_{1,2})$ and $R_{1,2} \approx 1$, the change in transmitted power due to absorption $\alpha(\nu)$ can be written as

$$\frac{\delta P_t(\nu)}{P_{inc}} = \frac{2\mathcal{F}\alpha(\nu)L}{\pi}. \tag{5.2}$$

A detailed derivation of these expressions can be found in Appendix B.2. Equation 5.2 illustrates that in the limit of low absorption, steady-state CEAS results in an enhancement of the single pass absorption signal by a factor of $2\mathcal{F}/\pi$. Steady-state CEAS has the benefit that it is the most sensitive of the intra-cavity absorption measurement techniques. However, as discussed in the previous section, there are several drawbacks to this technique. The first is the complexity of the comb-cavity servo system necessary to control both the laser $f_r$ and $f_o$ to high precision. Secondly, intra-cavity dispersion due to the mirrors and sample gas results in a limited spectral bandwidth over which the comb frequencies and cavity modes are overlapped. Finally, when locking a comb to a high finesse cavity, it is

difficult to avoid frequency to amplitude noise conversion, unless a technique similar to NICE-OHMS is employed [114][126]. Consequently, the sensitivity benefit of steady state CEAS is often compromised by technical noise.

### 5.1.2 Trasient CEAS

Transient CEAS, performed by a frequency sweep between the comb and cavity modes, overcomes some of the limitations of steady-state CEAS. This scheme is relatively easier to implement due to the relaxed locking requirements and it solves the problem of limited spectral bandwidth encountered when locking the comb to the cavity. The cost of transient CEAS is a reduced sensitivity for absorption measurements.

To perform transient CEAS, the comb modes are made to overlap the cavity modes like they would be for steady state CEAS. However, instead of locking the comb to the cavity, a low modulation amplitude (<10% FSR), fast (>1 kHz) sweep is applied to either the laser $f_r$, $f_o$, or the cavity FSR. For a single comb component, the effect of intra-cavity absorption on the transmitted power is given by

$$\frac{P_t(\nu)}{P_{inc}} = T_1 T_2 \Big| \sum_{n=1}^{\infty} r_1^{n-1} r_2^{n-1} e^{-(2n-1)\alpha L/2} e^{i\phi_n(t)} \Big|^2. \tag{5.3}$$

Here $n$ is the number of cavity round trips and $r_{1,2}$ are the electric field reflection coefficients for the cavity mirrors. The phase term is given by

$$\phi_n(t) = 2\pi(2n-1)(L\frac{\nu(t)}{c} - 2(n-1)\beta\frac{L^2}{c^2}), \tag{5.4}$$

where $\nu(t)$ is the instantaneous frequency of the comb component, and $\beta$ is its frequency sweep rate [127] [128]. A derivation of the transient CEAS equations can be found in Appendix B.3. Besides the lower detection sensitivity, transient CEAS

also has the disadvantage that quantitative measurements of the intra-cavity absorption require careful calibration. The calibration accuracy is contingent on precise control of the frequency sweep. Maintaining a constant sweep rate is important. A common culprit causing non-constant sweep rates is hysteresis found in transducers such as piezo electrics. It is therefore necessary to either make measurements only in one sweep direction or determine the actual frequency sweep function and take measurements when the opposing sweep rates are equal.

## 5.2 Cavity ringdown spectroscopy

Another method for making intra-cavity absorption measurements is cavity ringdown spectroscopy (CRDS) [6][106] [129][130][107]. To perform CRDS, light is first injected into the resonant modes of the optical cavity. When the intra-cavity power in each cavity mode reaches a sufficient level, the light incident on the cavity is switched off. The cavity decay signal is then recorded by a photodiode with a detection bandwidth exceeding that of the cavity decay rate. The power in each cavity mode decays exponentially with a decay constant given by

$$\tau_{cavity} = \frac{1}{FSR(\nu)Loss} = \frac{1}{FSR(\nu)(1 - R_1 R_2 e^{-2\alpha(\nu)L})}. \tag{5.5}$$

Depending on the length and finesse of the optical cavity, this decay time can take on values ranging from tens of nanoseconds to hundreds of microseconds. In the limit that $\alpha(\nu)L \ll (1 - R_{1,2})$ and $R_{1,2} \approx 1$, the change in cavity decay time due to absorption $\alpha(\nu)$ can be written as

$$\frac{\delta\tau_{cavity}(\nu)}{\tau_{cavity}} = \frac{\mathcal{F}\alpha(\nu)L}{\pi}. \tag{5.6}$$

A derivation of the cavity ringdown equations is provided in Appendix B.1. For CRDS, the enhancement of the absorption signal in the low absorption limit is

exactly half of the enhancement in steady-state CEAS. This is due to the fact that for steady-state CEAS, the presence of the incident beam suppresses decay of the intra-cavity field from the input mirror. While in CRDS, the field decays through both the input and output mirrors. In the case that the reflectivity of the input and output mirrors are exactly equal, CEAS is twice as sensitive to intra-cavity absorption as CRDS. In the case of unequal reflectivities, Eqs. 5.1 and 5.5 can be used to determine the relative sensitivities.

CRDS has a couple of advantages over the CEAS methods for measuring intra-cavity absorption. First, since the laser is effectively switched off during the measurement time, cavity ringdown measurements are free of laser intensity noise. Also, since the finesse of an optical cavity is typically a very stable quantity that can be measured to high precision, background measurements of the cavity decay rate without any intra-cavity absorption can be performed relatively infrequently. Hence, more time can be devoted to making absorption measurements rather than calibrating them. The primary drawback of cavity ringdown spectroscopy is that it requires fast sampling to record the cavity decay rate. This becomes challenging in broadband applications where hundreds or even thousands of channels must be simultaneously sampled to record an intra-cavity absorption spectrum.

## 5.3 Sensitivity comparison

To conclude this section we present a comparison of the absorption signal enhancement for each of the three measurement schemes. This comparison will be illustrated by the enhancement of absorption signals for a transient CEAS measurement as a function of the speed at which a single comb 'tooth' is swept over a cavity mode. In the limit of an infinitely slow sweep, the signal enhancement of transient CEAS approaches that of steady-state CEAS. In the limit of a very fast

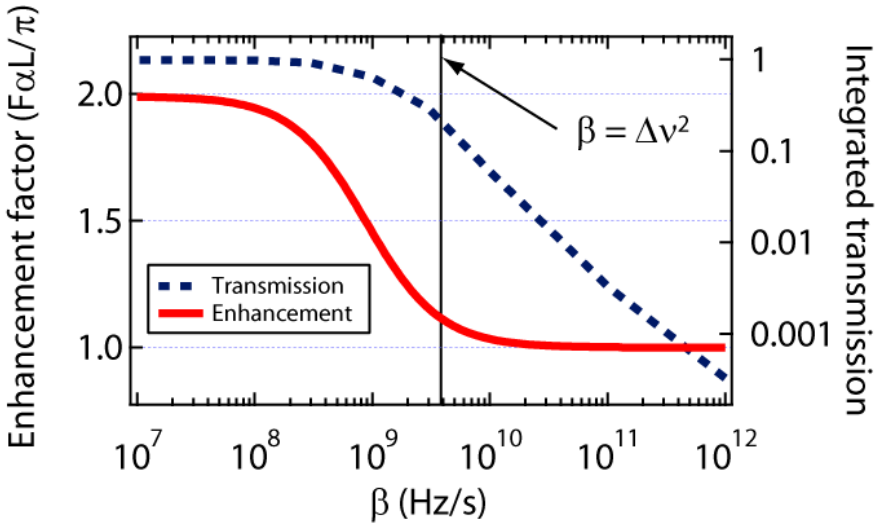


Figure 5.1: Absorption sensitivity and integrated power of cavity transmission versus sweep speed ($\beta$) for transient CEAS. Cavity FSR = 400 MHz and mirror reflectivity R = 0.9995 resulting in a cavity linewidth $\Delta\nu$ = 63.7 kHz. A time window of 100 $\mu$s was used for integrating the cavity transmitted signal.

sweep speed, the sensitivity of transient CEAS approaches that of CRDS. Fig. 5.1 shows both the low absorption limit detection sensitivity and the time-integrated fractional transmitted power in transient CEAS as a function of the sweeping speed of the incident laser frequency.

For the calculations displayed in Fig. 5.1, FSR = 400 MHz and $R_{1,2} = |r_{1,2}|^2$ = 0.9995, resulting in a cavity lifetime of 2.5 $\mu$s. A time window of 100 $\mu$s was chosen for integrating the cavity transmitted signal. The center wavelength was 1.525 $\mu$m and the intra-cavity absorption was $10^{-8}$ cm$^{-1}$. At slow sweep speeds, it takes a comb frequency many cavity lifetimes to scan across the cavity linewidth. Under these conditions, the intra-cavity power nearly reaches the steady state value and cavity transmitted beam power is $P_\alpha = P_o(1 - 2F\alpha L/\pi)$. Here, $P_o$ is the cavity transmitted power with no intra-cavity absorption. For a fast sweep speed, the comb frequency scans across the cavity resonance in much less than a cavity lifetime. In this case, the peak intra-cavity power is much smaller than the steady

state value, and the majority of the cavity transmitted signal takes the form of an exponential decay. Since the time integral of an exponentially decaying signal is proportional to its decay time, the change in the integrated cavity transmission due to absorption is just proportional to the change in the cavity ringdown time, thus linking transient CEAS to CRDS. When the frequency sweeping speed ($\beta$) is such that the comb frequency traverses the cavity line-width in one or a few cavity lifetimes ($\beta \approx \Delta\nu^2$), changes in the cavity transmission due to intra-cavity absorption arise from a combination of steady state CEAS and CRDS effects.

Unless a modulation spectroscopy technique is used to separate intensity noise for the absorption signal, it is usually advantageous to sacrifice the factor of 2 enhancement associated with steady state CEAS and work in the regime of fast sweeping. Doing so allows us to avoid relatively low frequency mechanical noise present in both the laser and the passive optical cavity. The gain in S/N by making detection at Fourier frequencies where mechanical noise is low is typically much greater than the factor of 2 gained via steady-state detection.

# Chapter 6

# Detection schemes

In the previous chapter we outlined a few strategies for making intra-cavity absorption measurements. In this chapter we focus on broad-bandwidth detection schemes that can be implemented to provide frequency-resolved and massively parallel detection channels for the intra-cavity absorption. Depending on the particular application, different detection schemes can provide uniquely optimized performances.

## 6.1 The grating spectrometer

The simplest way to perform parallel detection of a broadband cavity transmission signal is to disperse the beam using a diffraction grating. The dispersed beam can then be imaged onto a multi-channel detector such as a photodiode array or a CCD camera. Since nearly all of the multi-channel detection techniques presented in this chapter involve the use of a diffraction grating, we will devote the first section to developing the theory of the grating spectrometer. We will then highlight the capabilities of the grating spectrometer for parallel detections before presenting schemes for implementation in the following sections.

### 6.1.1 Theory of the grating spectrometer

When used for parallel detection of many frequency channels, a grating spectrometer consists of a diffraction grating, an imaging lens, and a detector array, as shown in Fig. 6.1. In the following paragraphs, we derive equations for several properties of a grating spectrometer including the spatial dispersion, the spectral resolution, and intensity distribution of light at the detection plane.

As shown in Fig. 6.1, the cavity transmitted beam, with beam radius $w$, is incident on the diffraction grating at an angle $\theta_{ig}$. The diffracted angle of the light leaving the grating $\theta_{dg}$ is determined by the grating line-spacing $d$, the wavelength of the incident light $\lambda$, and the incident angle of the beam according to the familiar grating equation [131]

$$m\lambda = d(\sin(\theta_{dg}) - \sin(\theta_{ig})), \tag{6.1}$$

where m is the order of the diffracted light. Typically the first diffraction order (m = 1) is used to maximize the diffraction efficiency. The angular separation between two different wavelengths as a function of diffracted angle can be found by solving equation 6.1 for $\theta_{dg}$

$$\theta_{dg} = \sin^{-1}\left(\frac{m\lambda + d\sin(\theta_{ig})}{d}\right). \tag{6.2}$$

Next, Eq. 6.2 is differentiated with respect to wavelength and then we substitute Eq. 6.1 into the denominator yielding

$$\frac{d\theta_{dg}}{d\lambda} = \frac{1}{\sqrt{1-\left(\frac{m\lambda+d\sin(\theta_{ig})}{d}\right)^2}}\frac{m}{d} = \frac{1}{\sqrt{1-\sin^2(\theta_{dg})}}\frac{m}{d}. \tag{6.3}$$

Finally, we use the identity $1 = \sin^2(\theta) + \cos^2(\theta)$ to obtain a compact formula for the angular dispersion of light diffracted from the grating

$$\Delta\theta_{dg} = \frac{m}{d\cos(\theta_{dg})}\Delta\lambda. \tag{6.4}$$

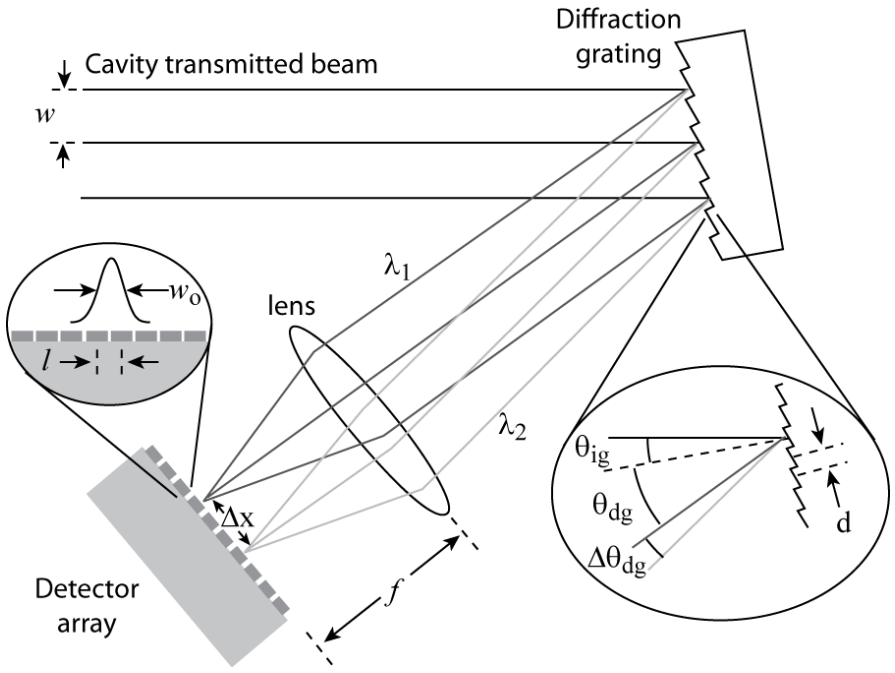


Figure 6.1: Grating spectrometer schematic. A cavity transmitted beam with 1/e electric field radius $w$ is incident on a diffraction grating with line-spacing $d$ at angle $\theta_{ig}$. Light is diffracted from the grating at a wavelength dependent angle $\theta_{dg}$. The dispersion of grating is characterized by the angular separation $\Delta\theta_{dg}$ between two wavelengths separated by $\Delta\lambda$. The dispersed light is imaged onto a detector array with pixel pitch $l$ using a lens of focal length $f$. The detector array is placed at the focal plane where the focused light has a diffraction limited spot size $w_o$.

Once the grating dispersion is known, an imaging relationship from Fourier optics, $\Delta x = \Delta\theta f$, can be used to determine the spatial separation ($\Delta x$) of the optical frequencies at the detector array (the focal plane) [132][133].

$$\alpha = \frac{dx}{d\omega} = \frac{\lambda^2 f}{2\pi c d \cos(\theta_{dg})}. \tag{6.5}$$

Here, the diffraction order $m = 1$ has been assumed, and the differential relationship

$$\Delta\lambda = -\frac{\lambda^2}{2\pi c}\Delta\omega \tag{6.6}$$

has been used to convert from wavelength to angular frequency. The radius of a focused, single wavelength, beam on the detector array is related to $w$ by the

imaging lens focal length, and the incident and diffracted angles from the grating [134][133]

$$w_o = \frac{\cos(\theta_{ig})}{\cos(\theta_{dg})} \frac{f\lambda}{\pi w}. \tag{6.7}$$

Combining equations 6.5 and 6.7 with the Fourier relation results in an equation for the frequency dependent spatial intensity distribution of light on the detector array

$$I_{det}(x,\omega) \propto I_{in} e^{\frac{-2(x-\alpha\tilde{\omega})^2}{w_o^2}}. \tag{6.8}$$

Here $\tilde{\omega} = \omega - \omega_o$ and $\omega_o$ is the frequency at the center of the detector array. The maximum resolution that can be achieved by a grating spectrometer depends on the diameter of the incident beam $w$, the wavelength of the incident light, the line-spacing of the grating, and the incident and diffracted angles [135]. If we choose a fairly conservative resolution condition (e.g. two spots must be separated by a $1/e^2$ beam diameter to be resolvable) we find that the maximum resolution is

$$\Delta\nu_{min} = \frac{2cd}{\pi w\lambda}. \tag{6.9}$$

Two conditions must be met to achieve the resolution limit of Eq. 6.9. First, the lens used to image the diffracted light onto the detector must have low aberrations (chromatic, spherical, etc.) and must be sufficiently well aligned to reach the diffraction limit. Second, the diffraction limited spot size must be much larger than the pixel pitch $l$ such that the spectrometer resolution is not limited by spatial sampling of the detector array.

Grating spectrometers typically provide resolutions on the order of a few to many tens of gigahertz. The overall spectral bandwidth that can be recorded by the detector in a single shot is limited by both the size of the detector array and the area over which a flat, or abberation free, field of imaging can be maintained. In general, single shot spectral bandwidths range from hundreds of gigahertz to several terahertz. For a fixed detector size with $n$ resolvable detection channels

and a resolution of $\Delta\nu$, the spectral bandwidth that can be recorded in a single shot is $n\Delta\nu$. This relationship illustrates the compromise that must be made between single shot bandwidth and resolution that is encountered when designing a broadband detection system.

## 6.2 Multi-channel cavity ringdown detection

A serious issue that arises from multichannel detectors is the rate at which the array can be read out. Depending on the detector size and the type of a multiplexer used for sampling, read-out rates in the tens of Hz to tens of kHz range can be achieved. While the later provides fast frame acquisitions for signal averaging, it is still too slow to directly observe cavity ring-down decays. Most cavities require a sampling rate of around 1 MHz to perform accurate ring-down measurements. In the following subsections two techniques are described for simultaneously recording multiple channels of cavity ring-down signals.

### 6.2.1 Streak camera cavity ring-down

The first method, originally referred to as 'Ring-down spectral photography', uses a rotating mirror to streak the cavity transmitted light across a CCD camera [136]. Using this technique the cavity ringdown decay signal is recorded by the CCD as a as a function of position on the detector array [137]. During our first experiment involving CE-DFCS, we implemented this strategy. Images of the position-dependent decay from these experiments are shown in Fig. 6.2a, b, & c. Here, the cavity transmitted beam was dispersed in the horizontal dimension by a grating and a rotating mirror was positioned between the imaging lens and the camera to streak the beam across the camera in the vertical dimension [37]. For

this experiment, we used a resonantly driven (355 Hz) gold mirror mounted on a torsion spring as our rotating mirror. The mirror had a total deflection angle of 40° (20° in each direction from its rest position) and was placed 10 cm from the CCD. The mirror was aligned so that the cavity transmitted beam was incident on the center of the camera when the mirror was at rest. Accordingly, the beam deflection as a function of time at the CCD plane is given by

$$x(t) = x_o \cos(\omega t), \tag{6.10}$$

where $x_o = 10(cm) \times \tan(20°)$ and $\omega = 2\pi \times 355$ Hz. The velocity of the beam across the center of the CCD is found by differentiating Eq. 6.10 with respect to time

$$v(t) = \omega x_o \sin(\omega t). \tag{6.11}$$

The grating spectrometer used for these measurements produced a 2 cm diameter beam that was focused onto the CCD with a 25 cm focal length lens. The near diffraction limited spot size measured at the CCD had a 1/e width of a = 12.5 $\mu$m. At the center of the CCD, the focused beam traverses each pixel in time

$$\delta t = \frac{a}{v_{max}} = \frac{12.5\mu m}{\omega x_o} = 0.15\mu s. \tag{6.12}$$

The detection cavity for this experiment had a finesse of 4500 and an FSR of 380 MHz, resulting in an empty cavity ring-down time of 1.88 $\mu$s. Therefore, the streak camera spectrometer sampled the cavity transmitted intensity more than 12 times during each 1/e-decay interval of the intra-cavity power. Equation 6.11 is used to precisely convert the decay-versus-position signal to decay versus time. The cavity ring-down signal is then fit with a decaying exponential to extract the ring-down time, which is related to the intra-cavity absorption at the corresponding detection channel. Each column of the CCD simultaneously records a decay signal at a different wavelength, resulting in a single-shot, broad bandwidth

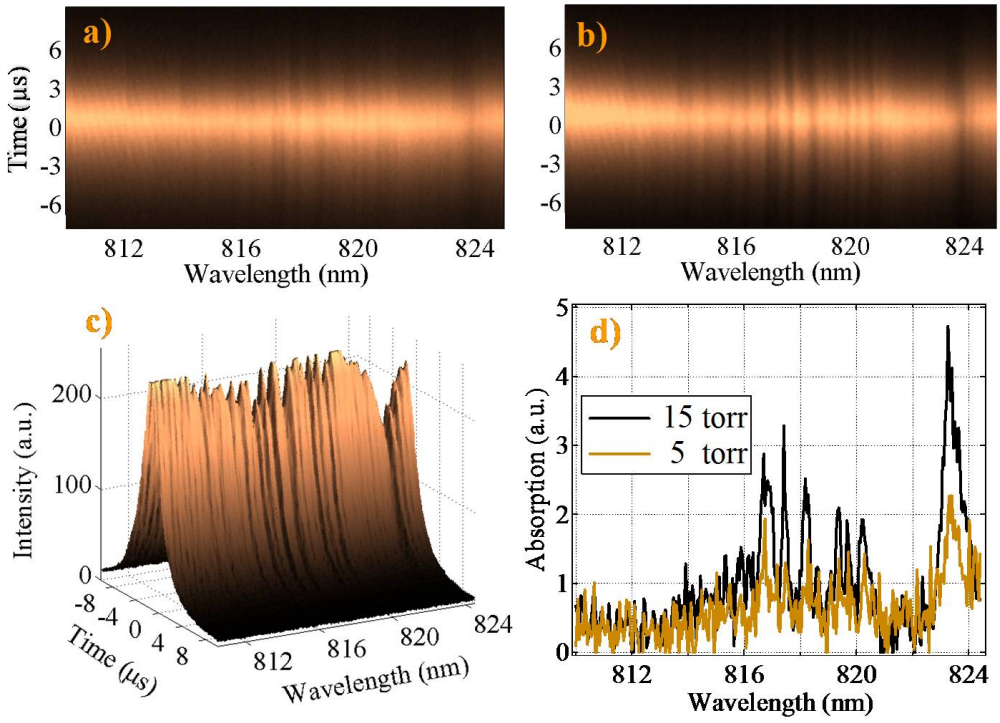


Figure 6.2: Streak camera images recorded near 820 nm with a) 5 Torr and b) 10 Torr of $H_2O$ inside the detection cavity. c) A 3-D image of the 10 torr streak image reveals the lower build-up and faster ring-down of the wavelengths that correspond to strong $H_2O$ absorptions. d) The mirror rotation rate and mirror to CCD distance are used to convert the streak images into ring-down times which are then converted to absorptions.

ring-down spectrum shown in Fig. 6.2d.

To successfully record broadband ring-down images like those in Fig. 6.2, two conditions must be met. First, the cavity decay events must be synchronized with the rotating mirror such that the ring-down signal hits the same area on the CCD for every measurement, thus preserving the position-time calibration. This can be accomplished by sweeping the laser $f_r$ with a sawtooth waveform that is triggered by the rotating mirror driver electronics. A convenient way to derive this signal is to integrate the TTL synchronization signal from the rotating mirror driver electronics. Secondly, $f_o$ and $f_r$ of the comb must be well matched to the cavity as described in Section 4.1.3 such that all wavelengths are simultaneously

resonant with the optical cavity.

Since the scanning mirror in this experiment operated at 355 Hz, we were able to acquire a ring-down spectrum every 1.4 ms. However, the CCD we used is capable of exporting a ring-down image to the data acquisition computer every 300 $\mu$s. Therefore, the use of a faster scanner could result in a faster spectral acquisition rate. Eventually, the camera frame rate will be the ultimate limitation for the streak camera detection scheme. In the next section, we discuss an electronics architecture that could be used to acquire ring-down spectra much faster than is possible using the streak camera method.

### 6.2.2 Multichannel cavity ring-down sampling electronics

The main disadvantage of the streak camera method is that it requires a 2D detector array to record 1D spectral data. To directly sample ringdown signals from a large-numbered 1D photodiode array, we have developed an electronics architecture that is capable of sampling and recording ringdown events from an arbitrarily large photodiode array at rates that can easily exceed 1 MHz. A block diagram of the electronics architecture is shown in Fig. 6.3. A large photodiode array, consisting of hundreds to thousands of detector elements, is first divided into sub-arrays of 10 to 50 elements that detect adjacent portions of the optical spectrum. The photodiode array in Fig. 6.3 represents one of these sub-arrays. The current from each element in the sub array is converted to a voltage by a bank of transimpedance amplifiers. Next, a bank of comparators is used to compare these photo-voltages against a known reference voltage that is set by a digital-to-analog converter (DAC). The reference voltage is chosen to be a fraction of the peak voltage recorded by one of the detector elements in the sub-array. As the intra-cavity field decays, each photo-voltage drops below the reference voltage

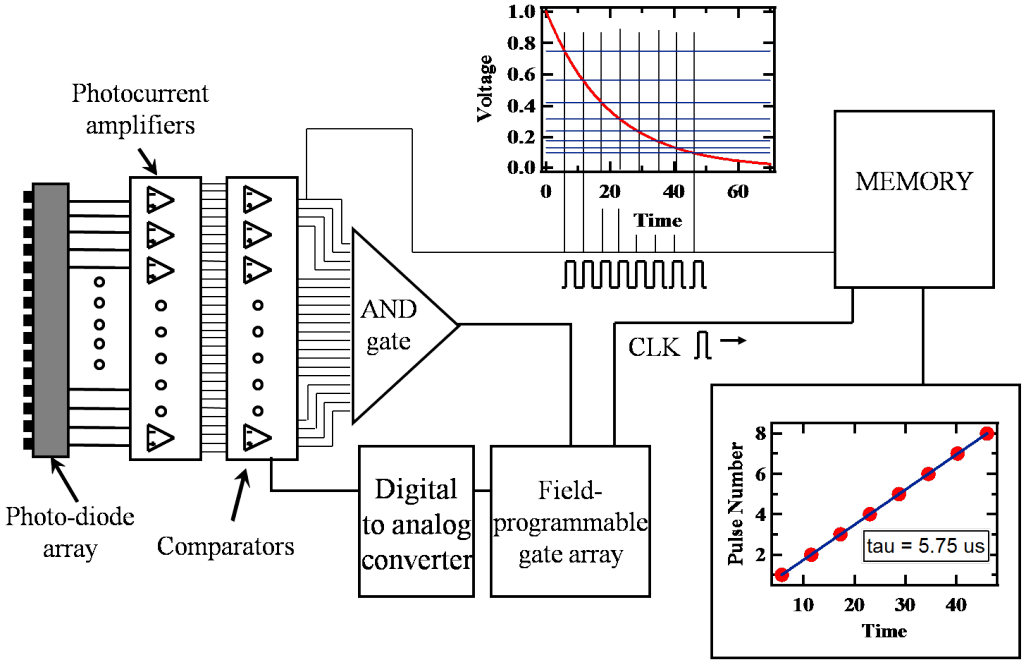


Figure 6.3: A circuit for parallel readout of cavity ringdown signals from a photodiode array.

and the corresponding comparator emits a pulse that is recorded by a clocked memory chip. The comparator pulse is also sent to the input of an AND gate. When each signal drops below the DAC voltage, the output of the AND gate switches, instructing the DAC to set a new reference voltage. The subsequent reference voltages are chosen to be a power law series such that an exponentially decaying ring-down signal will produce a series of comparator pulses that are equally spaced in time. This sequence continues until all signals drop below the lowest reference voltage. During this process, a field programmable gate array (FPGA) performs a number of operations to ensure that the reference voltages switch at the appropriate times and that the ringdown signal for each channel is recorded correctly. When the comparator pulse arrival data is retrieved from the memory chip, a simple linear fit of the arrival time of the comparator pulses versus pulse number reveals the ringdown time of that channel. So far, only a small

prototype of this circuit consisting of four channels has been built and tested, but the scalability of this architecture will allow for hundreds to thousands of channels to be simultaneously sampled with a small additional effort.

## 6.3 The virtually-imaged phased-array spectrometer

One way to overcome the compromise between spectral bandwidth and resolution is to use a virtually-imaged phased-array (VIPA) spectrometer shown in Fig. 6.4 [138][38][76]. This spectrometer contains a solid etalon (VIPA etalon), similar to a Fabry-Perot, whose spectral dispersion is oriented orthogonally to that of a diffraction grating. The etalon is tilted slightly ($\sim 2^{\circ}$) from normal incidence such that the beam transmitted from the VIPA resembles an elongated stripe of light. The name and dispersing capability of the VIPA come from the fact that as light bounces back and forth up the etalon, the transmitted light appears to originate from a phased-array of sources (see inset in Fig. 6.4). These sources are termed 'virtual' because their apparent locations are on a line that extends from the back side of the VIPA normal to the surface. The interference of the source array gives rise to a large angular dispersion of light transmitted from the etalon that is roughly 20 times greater than the dispersion of an optical grating [139]. A diffraction grating is placed after the etalon to disperse the transmitted beam into a 2D pattern, with each spatial element corresponding to a unique comb frequency. The 2D spatial pattern of the comb is then imaged onto a CCD camera to record the frequency-resolved image of the cavity transmitted power. While light dispersed along the tilt of etalon provides a high spectral resolution, light dispersed along the orthogonal direction by the grating acts to resolve the different mode orders transmitted through the VIPA.

Like a Fabry-Perot etalon, each mode order of a VIPA etalon covers a frequency range that is equal to the FSR of the etalon. Unlike a Fabry-Perot, the

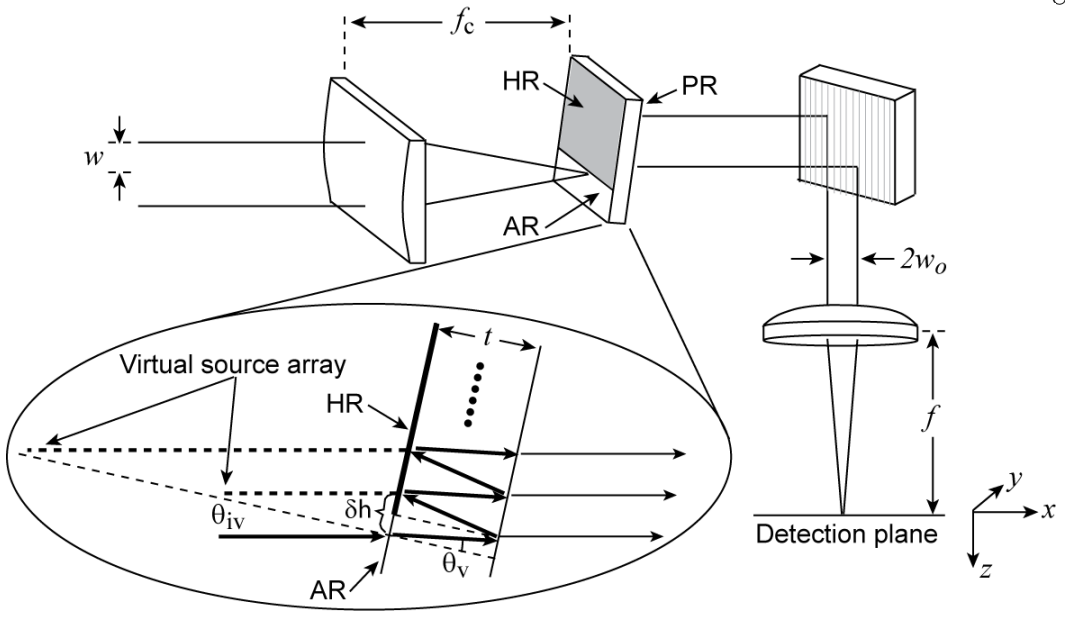


Figure 6.4: A schematic of the VIPA spectrometer showing the incident beam focused into the VIPA etalon via a cylindrical lens. The transmission of the VIPA etalon is dispersed in the horizontal dimension using a diffraction grating and then imaged onto the focal plane of a detector array. The expanded VIPA schematic shows the incident angle of the focused beam $\theta_{iv}$ and the propagation angle inside the VIPA $\theta_v$. The array of virtual sources that generate the interference pattern transmitted from the VIPA are shown originating from a line perpendicular to the surface of the etalon.

surface of the VIPA is designed with three regions of different reflectivity. The bottom of the front side of the etalon has an anti-reflective (AR) coating and is used to couple light into the VIPA. The top of the front side has a highly reflective (HR) coating (R$\sim$100%) that directs light inside the VIPA toward the transmission direction. Finally, the back side has a partially-reflective (PR) coating (r$\sim$96%) that transmits a small portion of the light from inside the VIPA at each reflection point. The sum of all of the transmitted waves from the partially reflective surface creates the phased-array interference effect and hence the angular dispersion of the transmitted beam.

### 6.3.1 Theory and design considerations

There have been several theoretical treatments of the VIPA etalon [139][140] [138][141][142][143]. These theories vary in complexity and in agreement with experimental observations. The discussion presented here will be based on a master equation for the propagation of a beam through a VIPA spectrometer developed by Xiao *et al.* [138]

$$I_{det}(x,y,\omega) \propto I_{in} e^{\frac{-2f_c^2 y^2}{f^2 w^2}} \frac{1}{(1-Rr)^2 + 4Rr\sin^2(\frac{k\Delta}{2})} e^{\frac{-2(x-\alpha\tilde{\omega})^2}{w_o^2}}. \tag{6.13}$$

This equation describes the 2D intensity distribution of the frequency-resolved interference image at the detector plane. $f_c$ and $f$ are the focal lengths of the cylindrical and imaging lenses, $w$ is the incident beam radius, $R$ and $r$ are the high and partial reflectivities, and $k = 2\pi/\lambda$ is the wavenumber of the beam. Since the grating and VIPA dispersions are orthogonal, Eq. 6.13 is a simple product of the grating intensity distribution (x-direction) and the VIPA intensity distribution (y-direction) [133][141]. Therefore, the term for the grating dispersion intensity distribution is identical to Eq. 6.8. Most of the physics that determines the VIPA dispersion is contained in the parameter

$$\Delta = 2tn_r\cos(\theta_v) - 2t\frac{\tan(\theta_v)\cos(\theta_{iv})y}{f} - \frac{t\cos(\theta_v)y^2}{n_r f^2}. \tag{6.14}$$

Here, $t$ is the etalon thickness, $n_r$ is the index of refraction, $\theta_{iv}$ is the incident angle of the focused beam on the VIPA, and $\theta_v$ is the propagation angle of the beam inside the VIPA. The incident and internal propagation angles of beam are related according to Snell's law ($n_r\sin(\theta_v) = \sin(\theta_{iv})$). A thorough derivation of the VIPA intensity distribution using paraxial wave theory can be found in reference [141]. In the following paragraphs, Eq. 6.13 will be used to determine most of the important properties of the VIPA spectrometer.

The first important property we will examine is the spatial dispersion of

light at the detection plane. The intensity pattern in Eq. 6.13 has maxima when

$$k\Delta = 2m\pi, \tag{6.15}$$

where m is the mode order of the VIPA transmission. The approximate mode number is given by $m \sim 2tn_r\cos(\theta_v)/\lambda_c$ where $\lambda_c$ is the center wavelength of the dispersed spectrum. Using this condition, the wavelength can be related to the y-position in the detection plane by

$$m\lambda = 2tn_r\cos(\theta_v) - 2t\frac{\tan(\theta_v)\cos(\theta_{vn})y}{f} - \frac{t\cos(\theta_v)y^2}{n_r f^2}. \tag{6.16}$$

Taking the derivative of this expression with respect to $y$ yields an equation for the VIPA etalon dispersion

$$\frac{\Delta\lambda}{\Delta y} = -\frac{2t}{mf}\left[\tan(\theta_v)\cos(\theta_{iv}) + \frac{\cos(\theta_v)y}{n_r f}\right]. \tag{6.17}$$

Of course, this equation is important for mapping wavelengths to positions in the dispersed interference pattern. It is also useful during the spectrometer design process for determining if one FSR of the VIPA transmission will fit within the area of the detector array.

Another important property of the VIPA spectrometer is the spectral resolution. The resolution can be determined from the second term in Eq. 6.13. We know from Eq. 6.15 that the transmitted intensity is maximum when

$$\frac{1}{(1-Rr)^2 + 4Rr\sin^2\left(\frac{k\Delta}{2}\right)} = \frac{1}{(1-Rr)^2}. \tag{6.18}$$

As the wave number $k$ changes, the transmitted intensity is reduced from $I_{max}$ to $\frac{I_{max}}{2}$ when

$$(1-Rr)^2 = 4Rr\sin^2\left(\frac{k\Delta}{2}\right), \quad \text{or} \quad \frac{1-Rr}{2\sqrt{Rr}} = \sin\left(\frac{k\Delta}{2}\right). \tag{6.19}$$

Since $Rr \sim 1$, Eqs. 6.19 indicate that $\sin(k\Delta/2) \ll 1$ when the transmitted intensity drops to $\frac{I_{max}}{2}$. Accordingly, we can use the paraxial approximation

$(\sin(2\pi mx + \delta x) \approx \delta x)$ by defining

$$\frac{k\Delta}{2} = 2\pi mx + \delta x, \quad \text{and} \quad \frac{k_o\Delta}{2} = 2\pi mx, \tag{6.20}$$

where $k_o$ is a wavenumber that corresponds to $I_{max}$. Combining the two equations in 6.20, we find that

$$\delta x = \frac{\Delta k_o \delta\lambda}{2\lambda}. \tag{6.21}$$

Substituting this result into Eq. 6.19 yields an expression for the wavelength interval $\delta\lambda$ between the positions corresponding to $\mathrm{I}_{max}$ and $\mathrm{I}_{max}/2$ in the detection plane. The 'full width at half maximum' (FWHM) linewidth is defined as twice this interval such that

$$\delta\lambda_{FWHM} \approx \frac{\lambda_o^2(1-Rr)}{\pi\Delta\sqrt{Rr}}. \tag{6.22}$$

Using the familiar relation $\delta\nu = -(c/\lambda^2)\delta\lambda$ we can convert Eq. 6.22 to the frequency domain.

$$\delta\nu_{FWHM} \approx \frac{c(1-Rr)}{\pi\Delta\sqrt{Rr}}. \tag{6.23}$$

Equation 6.23 describes the position dependent resolution of the VIPA spectrometer in the y-direction. An examination of $\Delta$ reveals that the resolution is only weakly position dependent, so for most cases it is sufficient to write the VIPA spectrometer resolution using only the first term in $\Delta$

$$\delta\nu_{FWHM} \approx \frac{c(1-Rr)}{2\pi t n_r \cos(\theta_v)\sqrt{Rr}}. \tag{6.24}$$

A rigorous determination of the spectrometer resolution also requires consideration of the pixel size of the detector array. In particular, if the diffraction limited spot size of the focused beam on the detector is of similar size or smaller than the detector pixels, the pixel size must be considered in the resolution calculation. In this case, Eq. 6.17 is used to find the frequency interval that corresponds to one pixel width. The pixel frequency interval is then convolved with the VIPA

resolution function, which results in the overall spectrometer resolution.

Another important consideration regarding the VIPA resolution is the lineshape of a single frequency at the detector plane. The lineshape function can be derived by substituting the approximations in Eqs. 6.20 and 6.21 into the second term in Eq. 6.13

$$g(\lambda) \approx \frac{1}{(1-Rr)^2 + \frac{Rr\Delta^2 k_o^2}{\lambda^2}(\lambda - \lambda_o)^2}. \tag{6.25}$$

Here we see that while the grating spectrometer lineshape is Gaussian, the VIPA lineshape is Lorentzian. This arises because the light intensity transmitted from the VIPA decreases exponentially as a fucntion of height along the etalon [142][141]. Since the Lorentzian function decays slowly, the frequency channels in the VIPA spectrometer have high levels of cross-talk. This fact must be considered when making quantitative spectroscopic measurements of closely spaced absorption features. There have been several proposals to alter the VIPA lineshape including graded reflectivity coatings, but so far none of the solutions are practical to manufacture [142].

The final VIPA spectrometer property that we will discuss is the physical size of the interference pattern at the detection plane. The first term in Eq. 6.13 determines the y-direction extent of the interference pattern. Specifically, the distance between the 1/e intensity points in the detection plane is

$$W_y = \frac{\sqrt{2} f w}{f_c}. \tag{6.26}$$

Accordingly, the y-direction size of the interference pattern depends on the width of the cavity transmitted beam and the ratio of the focal lengths of the imaging lens and the cylindrical lens. Equation 6.26 is useful for matching the size of the VIPA interference pattern to the size of the detector array. When designing a VIPA spectrometer, it can happen that you wish to change $W_y$ to match the

Table 6.1: VIPA spectrometer example design parameters.

| VIPA and grating parameters | | Camera parameters | |
|---|---|---|---|
| $n_r$ | 2 | l | 25 $\mu$m |
| t | 1.5 mm | pixels | 320×256 |
| R | 1.0 | Lenses | |
| r | 0.96 | f | 20 cm |
| $\theta_v$ | 1.25° | $f_c$ | 6 cm |
| $\theta_{iv}$ | 2.5 ° | Incident beam | |
| d | 0.909 $\mu$m | $w$ | 1.5 mm |
| $\theta_{ig}$ | - 75 ° | $\lambda$ | 1.6 $\mu$m |
| $\theta_{dg}$ | 52.6° | | |

size of the detector, but it is not desirable to change either $f$ or $f_c$. In this case, a telescope can be used to expand or contract the cavity transmitted beam to produce the desired value of $W_y$.

### 6.3.2 VIPA spectrometer design example

In this section, we present an example design of a VIPA spectrometer. Using the parameters contained in Table 6.1 and the equations in Section 6.3.1, we will calculate some of the spectrometer properties and illustrate some of the important design considerations.

We begin with a calculation of the how efficiently light is coupled into the VIPA etalon. The coupling efficiency is determined by how of much the incident beam is clipped by the interface between the HR and AR coatings as it enters the etalon. The two important quantities for this calculation are the size of the focused beam as it enters the etalon $w_v$ and the length interval $\delta$h, shown in Fig. 6.4. Using the parameters in Table 6.1, the 1/e radius of the beam power is given by

$$w_v = \frac{f_c \lambda}{\sqrt{2}\pi w} = 14.4 \ \mu\text{m}. \tag{6.27}$$

The length interval $\delta$h can be found from the etalon thickness and the beam propagation angle inside the VIPA

$$\delta h = 2t\tan(\theta_v) = 65.4\ \mu\text{m}. \tag{6.28}$$

The clipping loss is minimized when the center of the incident beam is positioned $\delta$h/2 below the line separating the HR and AR coatings. The beam experiences clipping loss twice as it enters the etalon. Once as it enters the front surface of the VIPA and a second time when it makes its first reflection from the HR coating. According to the paramters in Table. 6.1, the portion of the beam coupled into the VIPA is

$$\frac{P_{coupled}}{P_{incident}} = (1 - e^{\frac{-37.8^2}{14.4^2}})^2 = 0.9885 = 98.85\%. \tag{6.29}$$

To understand how sensitive the coupling is to the spectrometer parameters we will make the same calculation, but this time we'll reduce the incident beam radius by half

$$\frac{P_{coupled}}{P_{incident}} = (1 - e^{\frac{-37.8^2}{28.8^2}})^2 = 0.525 = 52.5\%. \tag{6.30}$$

This small change in parameters has increased the clipping loss by a factor of 40 from 1.2% to almost 50%!

For the next calculation, we'll determine the vertical size of the VIPA interference pattern at the detector plane. To make efficient use of the light transmitted from the spectrometer, it is desirable to match the size of the interference pattern to the size of the detector array. In the y-direction, the detector has 256 pixels with a pixel spacing $l$ of 25 $\mu$m for a total height of 6.4 mm. The size of the interference pattern can be calculated using Eq. 6.26,

$$W_y = \frac{\sqrt{2}fw}{f_c} = 7.1\ \text{mm}. \tag{6.31}$$

According to Eq. 6.31, we can calculate that at the top and bottom of the image, the intensity of the VIPA fringes will have dropped to $e^{-3.2^2/3.55^2} \approx 44\%$ of their

value at the center of the image.

The next question we'll address is, "what is the size of one FSR of the VIPA transmission at the detector plane?" To make sure that most of the detector area contains unique spectroscopic information, one FSR should cover more than half of the y-direction size of the detector array. The VIPA etalon used here has an FSR of approximately $c/(2n_r t) = 50$ GHz, and the mode number of the VIPA transmission at 1.6 $\mu$m is $m \approx 2tn_r \cos(\theta_v)/\lambda = 3749$. With this information, Eq. 6.17 can be used to determine the spatial extent of one FSR

$$\Delta y \approx \frac{FSR\lambda^2 mf}{2tc\left[\tan(\theta_v)\cos(\theta_{iv}) + \frac{\cos(\theta_v)y_{ave}}{n_r f}\right]} = 4.2 \text{ mm}. \tag{6.32}$$

Here the average value of the y-coordinate ($y_{ave}$) in the detector plane is 1.6 mm. The result of this calculation is that one FSR of the VIPA transmission occupies (4.2 mm)/(6.4 mm) = 65% of the detector area.

The final calculation in this section will determine the resolution of our example VIPA spectrometer. According to Eq. 6.23, the VIPA resolution is

$$\delta\nu_{FWHM} \approx \frac{c(1-Rr)}{2\pi tn_r \cos(\theta_v)\sqrt{Rr}} = 650 \text{ MHz}. \tag{6.33}$$

To check if the pixel size affects the spectrometer resolution we can calculate the frequency interval corresponing to one pixel width

$$\delta\nu_{pixel} \approx \frac{2ltc}{\lambda^2 mf}\tan(\theta_v)\cos(\theta_i v) = 256 \text{ MHz}. \tag{6.34}$$

A convolution of these two frequencies results in a total resolution of 697 MHz, which shows that the contribution of the pixel width is minimal.

We conclude this section by presenting a CE-DFCS absoprtion image recorded by a VIPA spectrometer with paramters very similar to those in Table 6.1. Figure 6.5 shows an absorption image of the rovibrational spectrum of $CO_2$ centered at 1.609 $\mu$m. Each vertical fringe contains roughly 1.7 FSR mode orders of the

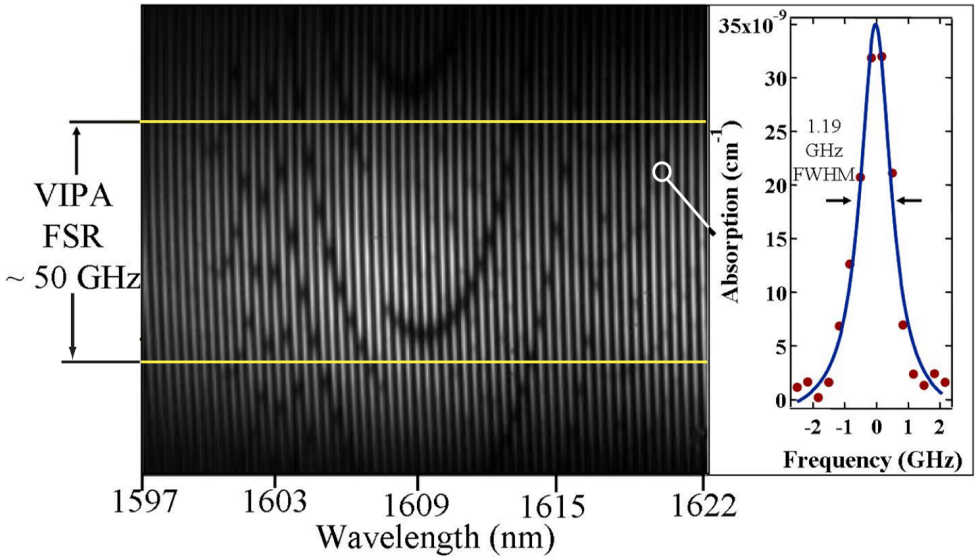


Figure 6.5: An image of a rotational spectrum of a $CO_2$ vibration overtone centered at 1.609 $\mu$m recorded with the VIPA spectrometer. The image contains 25 nm of spectrum with 833 MHz resolution. The panel to the right shows the P(13) line of the (011) to (311) vibration overtone band, illustrating the resolution.

etalon transmission, which has been dispersed and resolved in the horizontal direction by the grating. The vertical fringes in the interference pattern are well-resolved due to the 25 GHz resolution of the grating spectrometer compared to the 50 GHz FSR of the VIPA etalon. Probably the most impressive aspect of this image is that it contains more than 3500 spectral channels that were acquired simultaneously. This is far more than what could be achieved using a one-dimensional grating spectrometer, and with significantly higher resolution.

To create this image the cavity was filled with such a large concentration of $CO_2$ that the cavity response has been completely saturated. As a result, the cavity transmitted light is extinguished where there are $CO_2$ absorption features. This has been done for the purpose of visualizing the frequency resolved absorption patterns in the VIPA interference image; however, during typical operation of the spectrometer, the cavity is operated in the linear regime and absorption features are not be visible with a naked eye. Instead, a differential measurement

is made that subtracts the VIPA image with intra-cavity absorptions present from one that was taken when the cavity contains no absorption. This procedure will be discussed further in Section 6.3.4. However, before one can make absorption measurements, the VIPA spectrometer must first be constructed, aligned and calibrated. This procedure will be the subject of the next section.

### 6.3.3 Construction, alignment, and calibration

Before beginning to construct the VIPA spectrometer, there are few experimental conditions that must be met to ensure a successful experience. First, the average power of the beam used to align the VIPA must be sufficiently high to be easily detected. Ideally, the beam could be visibly detected via an IR card or a thermally sensitive liquid crystal sheet. Often times, the average power of the cavity transmitted beam is quite low and so it may be necessary to use a second laser beam that has been aligned collinear to the cavity transmission for aligning the VIPA. Second, the cavity transmitted beam should be aligned to propagate parallel to the optical table prior to aligning the VIPA spectrometer. Finally, the cavity transmitted beam should be well collimated. If the detection cavity has a gentle intra-cavity focus, this condition should already be met. Otherwise, a lens should be used to collimate the beam.

Figure 6.6 shows a four step procedure for constructing and aligning a VIPA spectrometer. In the first step, the VIPA etalon is positioned such that the division between the HR and AR coatings perfectly bisects the beam. Also, the bisecting line should be horizontal, or parallel with the optical table. The beam bisection can be optimized by adjusting the etalon position while watching either the transmitted or reflected beam from the VIPA. Next, the horizontal angle of the beam on the VIPA should be aligned to normal incidence. This is accomplished

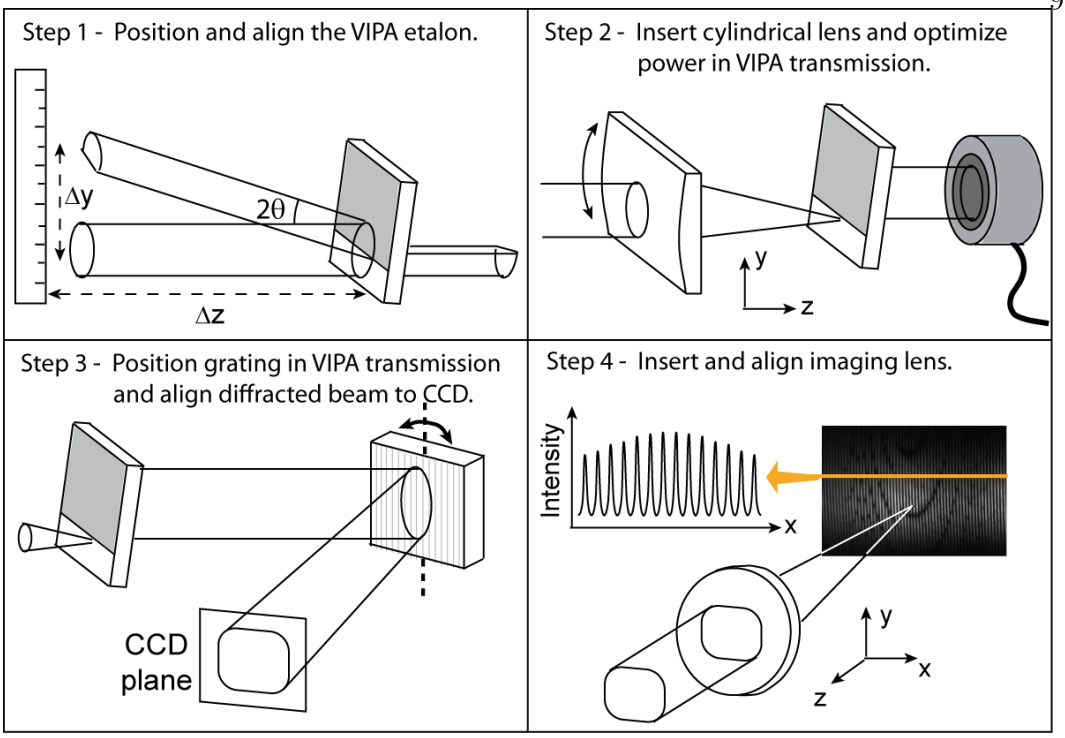


Figure 6.6: Procedure for constructing and aligning a VIPA spectrometer.

by adjusting the VIPA so that the reflected beam is directly above the incident beam. Finally, the vertical angle of incidence for the beam should be aligned to the desired value (typically 1.5°-3.5°). For this, a ruler can be placed at a known distance ($\Delta$z) from the etalon to measure the vertical displacement between the incident and reflected beams ($\Delta$y). These distances can then be used to calculate the vertical angle of incidence.

In the second step, the cylindrical lens is placed roughly one focal length in front of the VIPA etalon. This lens should create a horizontal focused line at the front surface of the etalon. The axis of the focus should be parallel to the line dividing the HR and AR coatings. The line-focus should intersect the front surface of the etalon approximately $\delta h/2$ below the HR/AR division as shown in Fig. 6.4. To adequately align the cylindrical lens, it is useful to mount it on a two-axis translation stage for fine control of the $y$ and $z$ position. Also, the lens

can be mounted on a goniometer for adjusting the angle of the line focus relative to the line dividing the HR and AR regions. The alignment of the cylindrical lens can be optimized by maximizing the power transmitted from the VIPA. When the beam is optimally coupled into the VIPA etalon, the transmitted beam should resemble a single vertical stripe that has the same width as the input beam. If the stripe is not vertical, or if it appears split into multiple stripes, the alignment is not optimal.

When the transmission of the VIPA looks optimal, it is time to introduce the grating. The grating should be mounted on a rotation stage such that the center of the grating's front surface is along the axis of rotation. The mount should also allow for control of the vertical tilt of the grating, which can be achieved by fixing the grating to a mirror mount. The grating should be positioned such that the VIPA transmission is centered on the grating as shown in Fig. 6.6. The zeroth-order reflection from the grating and the vertical tilt control can be used to make sure that the beam reflected from the grating is level with the optical table. Finally, the camera should be positioned in preparation for introducing the imaging lens. The distance between the camera and the grating should be at least 1.5 times the focal length of the imaging lens. The height of the detector array should be the same height of the beam above the optical table, and it should be positioned along the anticipated propagation direction of the beam diffracted from the grating. Finally, the plane of the detector array should be oriented perpendicular to the incident beam. This can be accomplished by positioning one arm of a carpenter's square along the line from the center of the grating to the center of the detector array. The other arm is then perpendicular to the incident beam and can be used as a reference for orienting the detector.

The final, and most difficult, step in aligning the VIPA spectrometer is optimizing the interference pattern at the detection plane. This discussion will first

address the procedure for coarse alignment of the imaging lens before moving on to fine-tuning the alignment. Five control axes are required to achieve optimal alignment of the imaging lens: a three-axis translation stage allows control of the (x, y, & z) positions of lens while a mirror mount provides tilt control in the vertical and horizontal directions.

For coarse alignment, place the imaging lens roughly one focal length from the detector plane. Position the lens so that the incident beam passes through the center of the lens. Again, a carpenter's square can be used to orient the lens perpendicular to the incident beam. At this point, an interference pattern similar to the one in Fig. 6.5 should be recorded by the camera. This image will be used to fine tune the alignment of the imaging lens. A particularly useful diagnostic is the line that transects the interference pattern in Fig. 6.7a, which corresponds to an intensity cross-section of the interference fringes on the detector. The camera images should be streamed via computer so that intensity cross-sections can be observed in real-time. Fig. 6.7 shows some of the ways that the fringe curve can be used to optimize the alignment of the imaging lens.

The first step in fine-tuning the imaging lens alignment is to optimize the focus of the fringe pattern. To do this, move the lens toward and away from the detector plane. You should observe the fringe contrast changing as you move the lens. At the lens position that produces the maximal fringe contrast, record the fringe contrast $(I_{max} - I_{min})/I_{max}$. Next, move the lens toward the detector plane until the fringe contrast has been reduced by half. Record the lens position. Similarly, move the lens away from the detector plan, past the optimal position, until the contrast is again reduce by half and record the lens position again. The lens should be placed at the average of the two recorded positions for optimal focusing of the fringe pattern.

While moving the lens toward and away from the detector plane it is worth

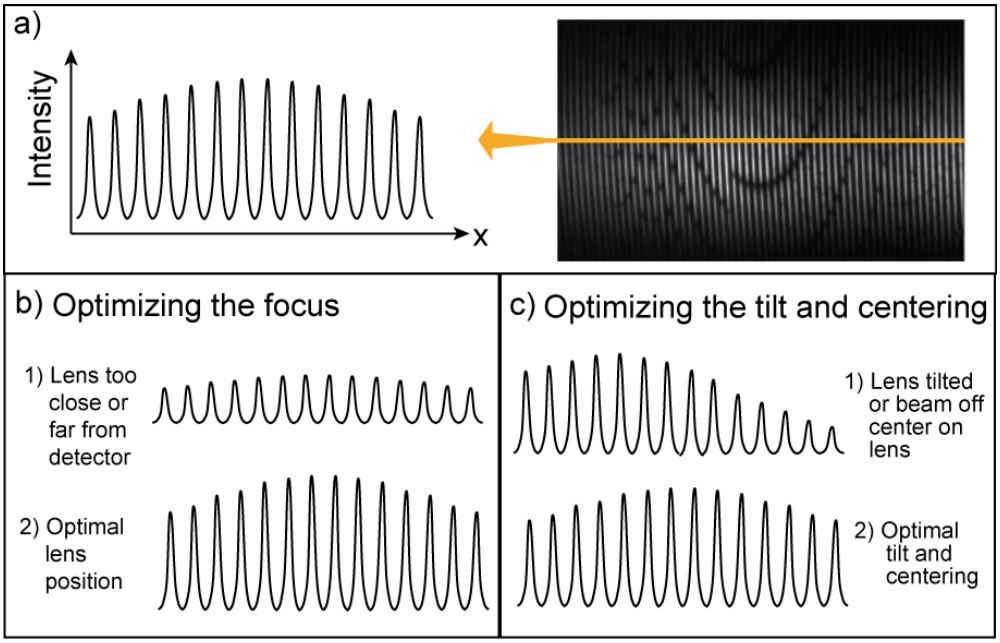


Figure 6.7: a) The fringe intensity cross-section. b) The focus of the imaging lens can be aligned by maximizing the fringe contrast. Curve 1 shows the fringe contrast when the imaging lens is either too close to (or far from) the detector. Curve 2 shows the fringes when the lens is optimally positioned. c) The tilt of the lens and centering of the diffracted beam on the lens can be optimized by comparing the fringe contrast at the left versus right side interference image. Similarly, the y-direction tilt can be optimized by comparing the fringe contrast between the top and bottom of the image.

noting if the contrast of the fringe pattern is changing uniformly across the image. If the fringe contrast changes are not spatially uniform, the imaging lens tilt and/or the centering of the incident beam on the imaging lens must be optimized. This is an iterative process by which the lens is tilted and/or translated until the fringe pattern is in sharp focus everywhere in the recorded interference pattern.

The final steps in preparing the VIPA spectrometer for making quantitative absorption measurements are wavelength and resolution calibrations. These calibrations can be done by filling the detection cavity with a low pressure, dilute sample of an appropriate calibration gas. The calibration gas should have absorption lines in the spectral region where the VIPA spectrometer will be op-

erated. The absorption lines should have well-known transition frequencies for wavelegnth calibration and well-known pressure broadening coefficients for resolution calibration of the spectrometer. The interference image in Fig. 6.5 shows the spectrum of $CO_2$, a good candidate for a calibration gas at 1.6 $\mu$m. Using this image, one can quickly determine the VIPA FSR interval. The many absorption features, each with a well-known transition frequency, allow for a complete mapping of wavelength to position within the interference image. Since the linewidth of the absorption feature is known (i.e. the Doppler width convolved with pressure broadened width), the resolution of the spectrometer can be determined by deconvolving the known linewidth from the linewidth measured by the VIPA spectrometer. An accurate measurement of the VIPA spectrometer resolution requires that the intra-cavity absorption be sufficiently weak such that it doesn't saturate the cavity response. Also, the intra-cavity pressure must be low enough that pressure broadening is negligible and the VIPA resolution is the dominant contribution to the measured linewidth.

### 6.3.4 VIPA image processing

Once the VIPA spectrometer is well-aligned and calibrated, it can be used to record spectra of the intra-cavity absorption. To extract a traditional absorption spectrum from the recorded VIPA images requires a modest amount of image processing. A flow diagram of the spectral recovery process is presented in Fig. 6.8, where a pair of 256 x 320 pixel images are converted into a 25 nm absorption spectrum. The first step is to locate the nearly vertical fringes produced within the picture. This is done using the reference image, which is recorded without intra-cavity absorption. Fringes are located by an algorithm that begins at the peak of each fringe at the middle of the picture (i.e. row 128) and 'walks' along

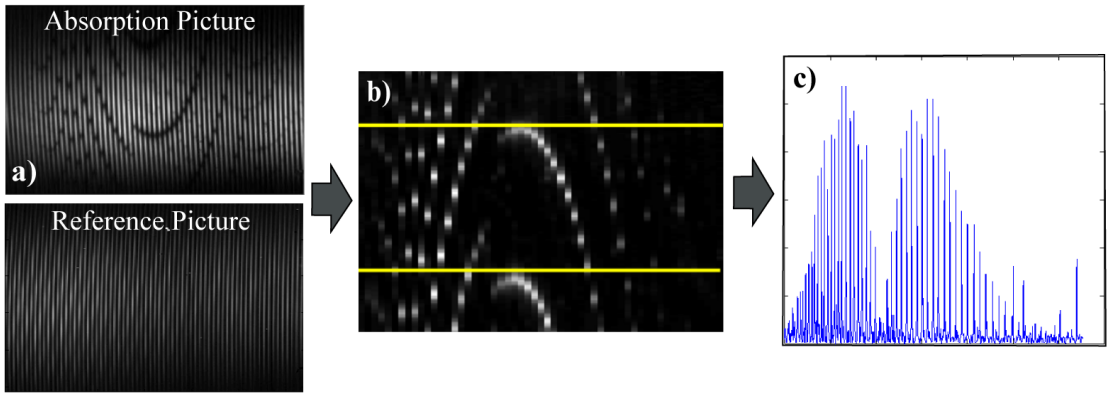


Figure 6.8: Generation of an absorption spectrum from VIPA images. a) absorption and reference images are recorded. b) The nearly vertical fringes in both the reference and absorption images are collected into column vectors and processed according to $(P_r - P_a)/P_r$ to form a relative power array. The relative power array is used to find the VIPA FSR, indicated by the area between the solid lines. c) The fringe intervals between the solid lines are then collected and arranged endwise to form a traditional absorption spectrum.

each fringe up and down to find the crest of each fringe within the entire picture frame. The intensity of each fringe is converted into a column vector forming an array that contains frequency resolved cavity transmitted power information. A MATLAB routine for finding the fringes with and calculating the normalized cavity transmitted power at each frequency within the VIPA image is provided in Appendix C.

To correct for possible drifts in the cavity transmitted power between the acquisition of the absorption and reference pictures, an area of low absorption in the absorption fringe array is equalized in power to the reference fringe array. The two fringe arrays are subtracted and then divided by the reference fringe array, resulting in a power-normalized fringe array shown in Fig. 6.8b. The FSR interval of the VIPA, shown as the interval between the two solid horizontal lines in Fig. 6.8b, is determined from the recognition of the repetitive patterns of absorp-

tion peaks in the power-normalized fringe array. All unique information about the molecular absorption is contained within this interval. Once this interval is determined, the area of the normalized fringe array between the horizontal lines is unwrapped into a one dimensional spectrum of relative power versus wavelength. Here the Eq. 6.13 can be used to obtain a high precision mapping of the position of each wavelength on the normalized fringe array. Finally, the cavity enhancement equations from Chapter 5 are used to convert changes in cavity transmitted power to their corresponding values of intracavity absorption.

## 6.4 Precision scan of $f_r$ and cavity filtration

Another approach for achieving high spectral resolution over a large spectral window is cavity-filtered comb detection. Unlike previously mentioned approaches that rely completely on optical dispersers to analyze the cavity transmission, the cavity-filtered detection uses the frequency response of the cavity itself to only allow specific spectral components of the frequency comb to be transmitted through the cavity at a time. Cavity filtered detection can be performed using a single detector element in cavity transmission, or in conjunction with a low resolution spectrometer and a detector array. The relationship between the $f_r$ of the comb and the FSR of the cavity determine which detection scheme should be used in cavity transmission.

### 6.4.1 Single detector element cavity filtered detection

In this section, we present an example of cavity-filtered detection that uses only a single detector element in cavity transmission. A detailed discussion of cavity frequency filtration is presented in Section 4.4. The results presented here are based on a $f_r = 99$ MHz mode-locked erbium fiber laser comb, a detection

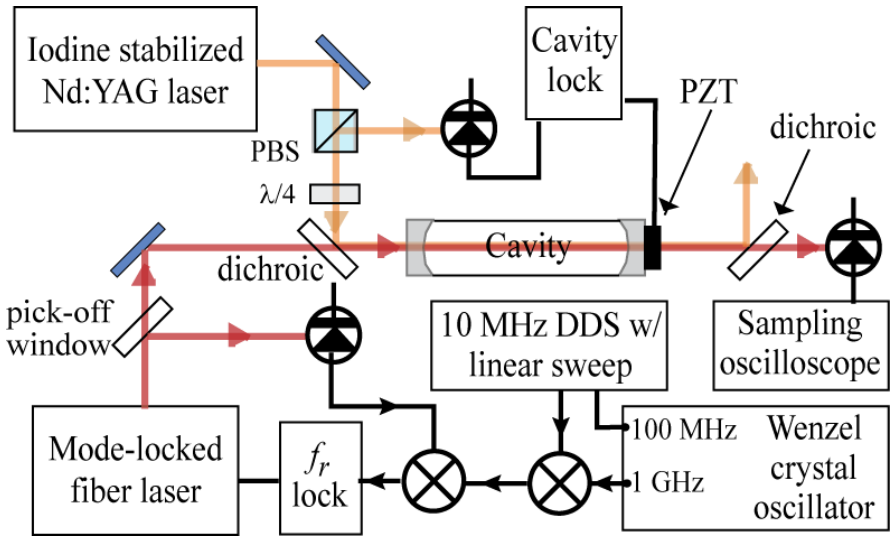


Figure 6.9: Schematic for the cavity filtration measurement setup. An iodine stabilized Nd:YAG laser (1064 nm) is used to stabilize the cavity frequencies via a piezo electric actuator that controls the cavity length. The $10^{th}$ harmonic of the laser $f_r$ is locked to a microwave signal that is the mixing product of a 1 GHz Wenzel oscillator and a 10 MHz DDS. To scan a spectrum, the DDS frequency is set such that the laser $f_r$ is detuned from the cavity FSR. The DDS frequency is then linearly scanned, resulting in a time-dependent output frequency for the cavity transmission.

cavity with an FSR of 396 MHz (FSR $\approx 4 \times f_r$), and a finesse of 6300 at the detection wavelength 1.525 $\mu$m. According to the relationship $\Delta\nu = \text{FSR/finesse}$, the cavity has an intrinsic linewidth of 63.5 kHz.

To use the cavity-filtration approach for frequency-resolved detection of cavity transmission, it is necessary to precisely control the frequencies of both the cavity and comb modes. For the measurements presented here, the frequency stabilization scheme is shown in Fig. 6.9. The cavity is stabilized by locking a particular cavity resonance (and thus the cavity length) to a frequency-stabilized Nd:YAG laser at 1064 nm, resulting in a $\lambda/3200$ stabilization of the cavity length. For an FSR ≈400 MHz cavity, this corresponds to stabilization of a cavity resonance frequency to within 250 kHz. To stabilize the relative frequency between the cavity and the comb, the tenth harmonic of the laser $f_r$ is locked to the frequency

difference of a 1 GHz low-phase-noise crystal oscillator and a 10 MHz auxiliary RF signal from a direct digital synthesizer (DDS). The time base of the DDS is slaved to the same low-phase-noise crystal oscillator. The DDS is used to generate a high precision linear frequency ramp that sweeps the comb frequencies over the cavity modes. The DDS makes a 500 Hz ramp in steps of 23 mHz, each lasting 10.2 $\mu$s for a total sweeping time of 0.22 s.

To illustrate the utility of this scheme for frequency-resolved detection of cavity transmission, the cavity was backfilled with 100 mTorr of $C_2H_2$ and 500 Hz scans were taken at detunings of $\delta f = 10$ kHz and $\delta f = 20$ kHz, where $\delta f = 4f_r -$ FSR (Fig. 6.10). Since the cavity modes were stabilized to within 250 kHz (effective $\Delta\nu$), the $\delta f = 10$ kHz scan resulted in a resolution of $(\Delta\nu/\delta f)\times$FSR = 10 GHz. The available spectral bandwidth for this scan is $mf_r^2/\delta f = 3.92$ THz, or 30 nm at 1.525 $\mu$m. Figure 6.10a shows a 25 nm spectrum, or 83% of the available scan range, with the $C_2H_2$ absorption spectrum clearly extracted in Fig. 6.10b. For the 20 kHz scan, $\delta f$ was increased by a factor of 2 and consequently the resolution increased and the bandwidth decreased by the same factor of 2. This leads to the 12 nm spectrum with 5 GHz-resolution shown in Fig. 6.10c. The variations in the baselines of these two scans arise from a combination of cavity-comb coupling noise and absorptions due to unresolved hot bands of $C_2H_2$ that occupy the same spectral region as the first overtone of the asymmetric C-H stretch.

### 6.4.2 Cavity filtration with multiple detection channels

A couple of options exist to use cavity filtration to achieve higher resolution detection. The first and the most intuitive approach is to increase the detuning $\delta f$ and perform scans of higher resolution with narrower spectral bandwidth. The second and more elegant method was recently demonstrated by Gohle *et al.*

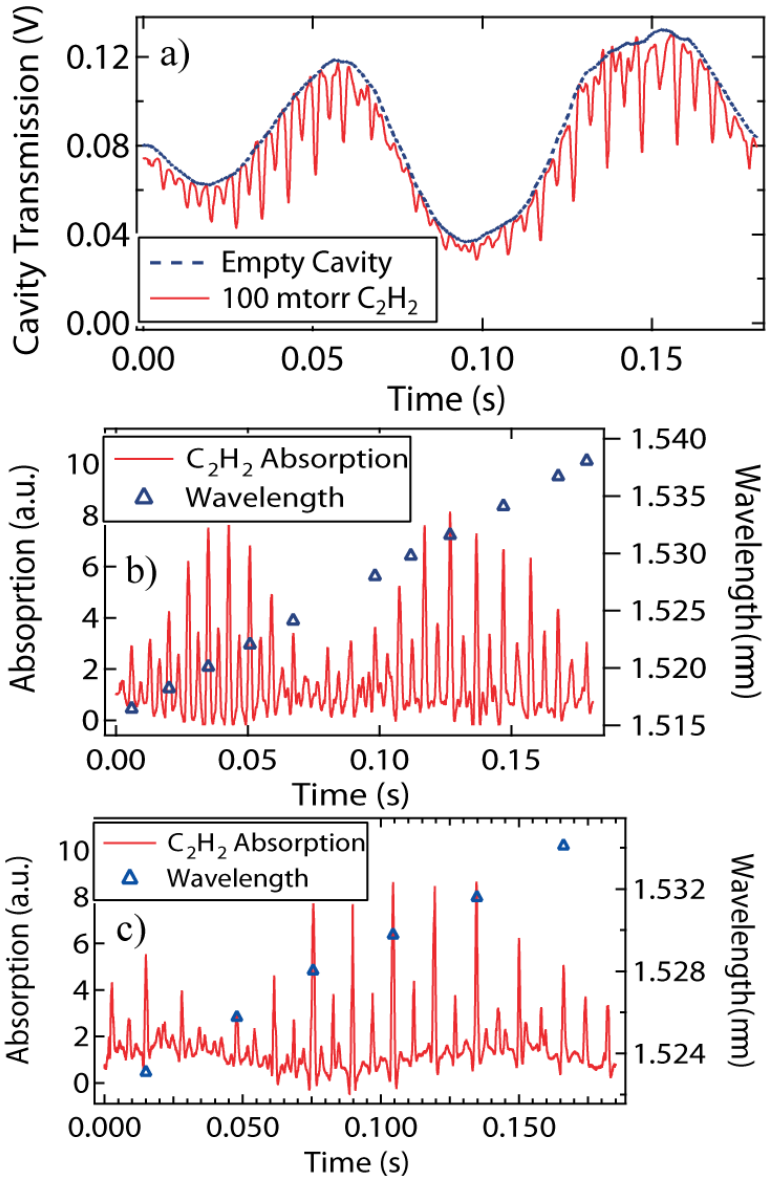


Figure 6.10: a) The cavity transmission signal with and without 100 mTorr of $C_2H_2$ inside the cavity for a $\delta f = 10$ kHz detuning of $4 \times f_r$ from the cavity $FSR$. b) The $C_2H_2$ absorption spectrum extracted from a) showing 25 nm of spectrum with 10 GHz resolution. c) A second sweep, where $\delta f = 20$ kHz, resulting in a 12.5 nm spectrum with 5 GHz resolution.

[122]. This method combines cavity filtering with a grating spectrometer in cavity transmission to achieve high resolution and large spectral bandwidth in a single system. In a sense this scheme shares the same spirit as the VIPA spectrometer,

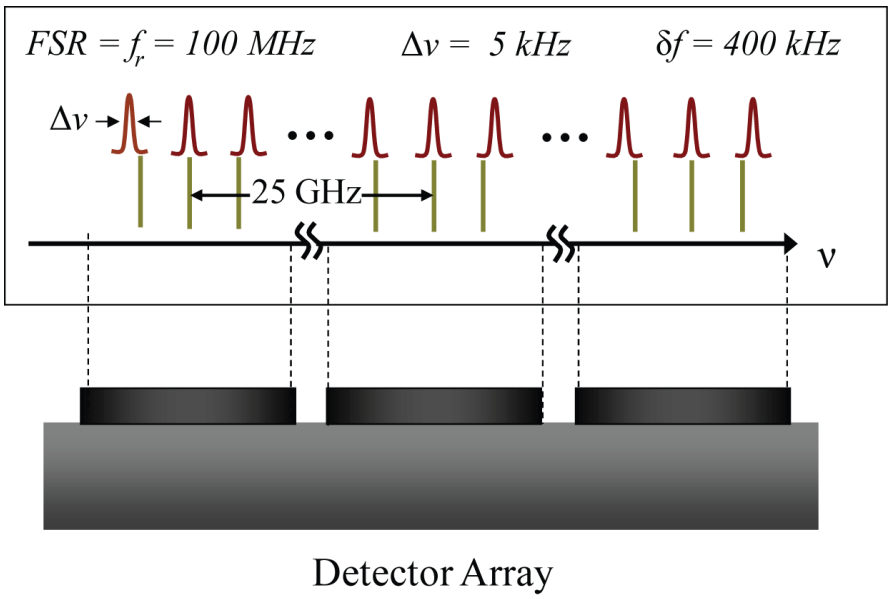


Figure 6.11: An example of how the comb-cavity detuning ($\delta f$) can be selected to match the cavity-filtered spectral bandwidth to the corresponding spatial period of a multichannel spectrometer in cavity transmission.

where a high resolution element (etalon) is combined with a low resolution grating. Whereas the VIPA scheme uses a second spatial dimension to provide high resolution, cavity filtration uses a temporal scan of the comb frequencies.

Figure 6.11 shows a schematic of how the cavity filtration and spatial dispersion can work together to provide high resolution and large spectral bandwidth. First, the detuning $\delta f$ is chosen such that the spectral bandwidth of cavity filtration is equal to or larger than the resolution of the grating spectrometer. In the case shown in Fig. 6.11, FSR $= f_r = 100$ MHz and $\delta f = 400$ kHz resulting in a spectral bandwidth of 25 GHz between frequencies where the comb is resonant with the cavity. Since the cavity linewidth, $\Delta\nu = 50$ kHz, is much less than $\delta f$, only one comb component is transmitted from the cavity in each 25 GHz frequency interval. Figure 6.11 shows a grating spectrometer with a resolution of 25 GHz can then be used to record the transmitted power of each comb component. Using this technique, the single-shot bandwidth of the grating spectrometer limits

the spectral bandwith of the measurement, while the resolution is limited by the cavity linewidth. Finally, each scan covers 250 cavity modes requiring a scan time of at least 250 cavity lifetimes for single comb mode resolution. For typical cavities, 250 cavity lifetimes corresponds to a scan time of one to tens of milliseconds.

# Chapter 7

# Applications

In the final chapter, we present a series of cavity-enhanced direct frequency comb spectroscopy measurements, beginning with initial demonstrations of these techniques followed by more advanced and recent measurements. This overview is meant to demonstrate the general capabilities of these systems and highlight recent technological advances that have allowed significant simplifications and expanded capabilities of the experimental setups. The initial demonstrations of CE-DFCS used Ti:Sapphire lasers at 800 nm and relatively low resolution grating spectrometers to probe weak high molecular overtone transitions. While these systems were adequate to develop the CE-DFCS measurement techniques, they were not well suited for demanding applications such as trace molecular detection.

As a first step toward addressing this problem we used an $Er^{3+}$ fiber laser at 1.5 $\mu$m to probe the much stronger first overtones of molecules containing C-H, O-H and N-H bonds. More recent work using the $Er^{3+}$ fiber laser and the high resolution VIPA spectrometer have allowed CE-DFCS to emerge as a powerful spectroscopic tool that combines high resolution, high sensitivity, and broad spectral bandwidth. The majority of this chapter is devoted to CE-DFCS measurements made using an $Er^{3+}$ fiber laser source and VIPA spectrometer detection. These measurements include trace detection of room temperature gas samples, molecular isotope analysis, human breath analysis, and detection and characterization

of supersonically cooled molecular jets.

## 7.1 Initial demonstrations

There were several demonstrations of cavity-enhanced absorption spectroscopy using short pulses with broad spectral coverage that provided the foundation for our eventual development of CE-DFCS. The first of these, performed by Crosson *et al.*, was referred to as 'Pulse-stacked cavity ring-down spectroscopy' and used a mid-infrared free electron laser (FEL) to coherently add picosecond pulses inside of an optical enhancement cavity [144]. This approach increased the S/N of cavity ring-down measurements by several orders of magnitude compared to a single pulse measurement. Using the pulse stacking scheme they were able to achieve an absorption sensitivity of $2 \times 10^{-9}$ cm$^{-1}$ at 10 seconds averaging time for an $H_2O$ absorption line at 5.38 $\mu$m. Crosson *et al.* realized that efficient coupling of pulses into the cavity required that the pulse injection rate be equal to a harmonic of the cavity FSR and that the phase of the injected pulse must match the phase of the pulse inside to cavity. However, since the FEL source had a large amount of phase noise and no means by which to control the phase of the incident pulse train, it could not be coupled optimally to the cavity.

Shortly thereafter, work by Scherer *et al.* made progress toward broad bandwidth detection by developing a spectrometer for the parallel acquisition of many cavity ringdown signals [137]. Their technique, known as 'Broadband ring-down spectral photography', used a broad-bandwidth dye laser and a rotating mirror in cavity transmission to streak the spectrally dispersed cavity-transmitted light across a CCD camera. This initial demonstration probed the rotational spectrum of the $b^1\Sigma_g - X^3\Sigma_g$ transition in $O_2$ and achieved the detection of a 8.5 nm spectral bandwidth with a 45 GHz resolution in a single measurement. This corresponds

to the parallel acquisition of 120 ring-down measurement channels. The primary drawback of this work was the extremely inefficient coupling of the dye laser spectrum into the optical enhancement cavity.

The final precursor to CE-DFCS was performed by Gherman and Romanini using a mode-locked Ti:sapphire laser to probe the high overtone spectrum of $C_2H_2$ at 860nm [121]. In this work, Gherman *et al.* came close to realizing the full set of requirements for efficient coupling of a frequency comb to an optical cavity. They determined that $f_r = \text{FSR}$ was a necessary condition, and also observed that even though $f_r = \text{FSR}$ they still had not achieved optimal coupling. They guessed that the non-optimal coupling must be due to $f_o$. Unfortunately, they had no means to control $f_o$ and therefore were not able verify their suspicion, nor could they achieve optimal coupling of the comb frequencies to the cavity modes. Their experiment used transient CEAS measurements and a cavity with a finesse of 420 for an absorption sensitivity of $2 \times 10^{-7}$ cm$^{-1}$ Hz$^{-1/2}$. A high resolution grating spectrometer and a CCD camera were implemented in cavity transmission to provide 14 nm of single shot bandwidth with a resolution of 6 GHz.

The first demonstration of CE-DFCS was made using a Ti:Sapphire laser-based frequency comb at 800 nm to probe the high overtone spectra of $C_2H_2$, $H_2O$, $NH_3$, and a weak forbidden electronic transition in $O_2$ [37]. This work, for the first time, exploited control of the $f_o$ to maximize the coupling efficiency of the frequency comb to the resonant modes of the optical cavity. This capability was coupled with parallel detection of cavity ringdown signals resulting in greatly improved S/N and sensitivity of absorption measurements. An example of these measurements is provided in Fig. 7.1. This system used a $\mathcal{F} = 3300$ cavity and cavity ringdown detection to achieve an integrated absorption sensitivity of $10^{-8}$ Hz$^{-1/2}$ ($2.5\times10^{-10}$ cm$^{-1}$Hz$^{-1/2}$). In cavity transmission a grating spectrometer and CCD were implemented to record 20 nm of single shot spectra with 25 GHz

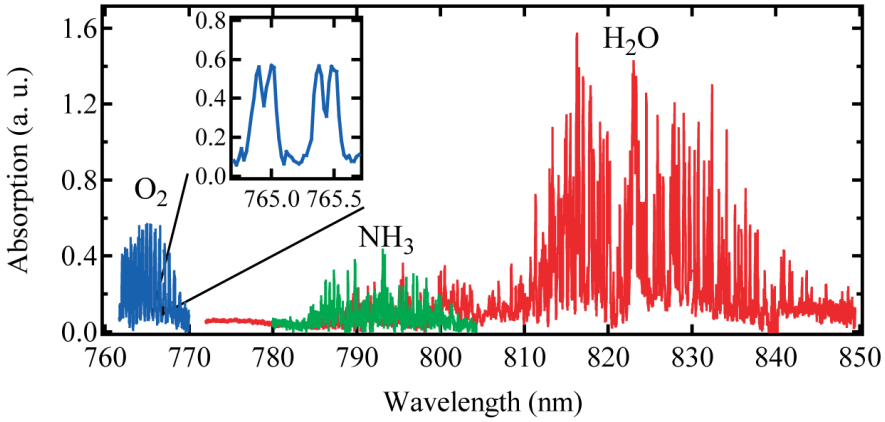


Figure 7.1: The overtone spectrum of $H_2O$ (red), the P-branch of the $b^1\Sigma_g - X^3\Sigma_g$ (0,0) vibrational transition of the electronic transition in $O_2$ (blue), and the overtone spectrum of $NH_3$ near 790 nm (green) demonstrate the broadband, high resolution, and high sensitivity capabilities of this spectroscopic technique. For each molecule, 1000 spectral scans were averaged to produce the traces shown. The inset graph show that the individual rotational lines of each spectrum have been resolved revealing the characteristic doublet structure of the $O_2$ rotational spectrum.

resolution. To achieve adequate time resolution of the ringdown signals, a rotating mirror was placed between the imaging lens and the CCD and the streak camera technique described in Section 6.2.1 was used. This combination of spectral bandwidth and resolution allowed for the parallel detection of 375 ring-down channels.

## 7.2 Trace detection at 1.5 $\mu$m

While the Ti:Sapphire-based CE-DFCS system provides good sensitivity for the study of high molecular overtones, the weak absorption associated with these transitions make them not very desirable for investigating low concentration

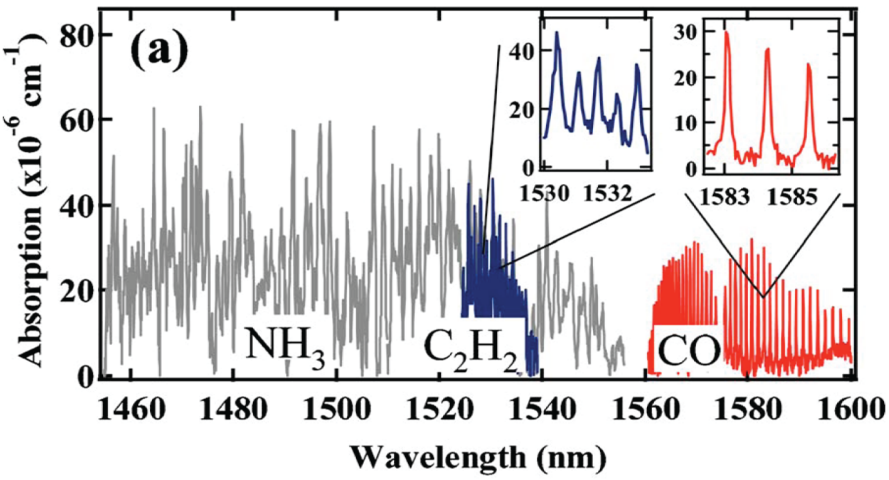


Figure 7.2: Absorption spectrum measurements for 2 Torr CO, 10 mTorr $NH_3$, and 1.5 mTorr $C_2H_2$, showing 150 nm of spectral information. The inset of the P-branch of the CO overtone spectrum shows individually resolved rotational lines.

molecular samples. Furthermore, the resolution of this system is too low to resolve the Doppler line-widths of room temperature gases, further limiting the sensitivity of molecular concentration measurements. In response to these limitations, we began constructing CE-DFCS systems based on $Er^{3+}$ fiber laser frequency combs at 1.5 $\mu$m. In addition, we implemented a high resolution VIPA spectrometer in cavity transmission to dramatically increase the detection sensitivity and spectral resolution without diminishing the spectral bandwidth available with CE-DFCS systems [76].

The first demonstration of CE-DFCS using an erbium fiber laser probed the first overtone transitions of $NH_3$ and $C_2H_2$, and the second overtone of CO [75]. This system still used a low resolution grating spectrometer in cavity transmission, and therefore was not well suited for performing trace detection measurements. However, the advantages of probing lower vibrational overtones for trace detection can already be seen in the measurements, shown in Fig. 7.2. Here the absorption spectra of 2 torr CO, 10 mTorr $NH_3$, and 1.5 mTorr $C_2H_2$ demonstrate that a thousand times greater concentration of CO is required to produce an absorption

signal that is similar to the signals from $NH_3$ and $C_2H_2$. The factor of 1000 in concentration is due to the fact that both $NH_3$ and $C_2H_2$ are detected using a first overtone transition while CO is detected via its second overtone. Because of this, the 1.5 $\mu$m spectral region is especially useful for detecting molecules with N-H, C-H, and O-H bonds.

The final step toward constructing a suitable trace gas detection system at 1.5 $\mu$m was the implementation of a high resolution VIPA spectrometer in cavity transmission. The complete 1.5 $\mu$m trace detection system was first reported in the breath analysis measurements in Ref. [76], and a schematic of this system is shown in Fig. 7.3. The move to high resolution detection allows for the optimization of the molecular absorption signal by matching the resolution of the spectrometer to the absorption line-width. This point will be addressed in more detail in the next section. For now, consider the simple case where the molecular absorption is much narrower than the spectrometer resolution. In this case, most of the light in a given detection channel will not interact with the molecular absorption. The result is that the molecular absorption signal is diluted by a factor equal to the ratio of the spectrometer resolution to the absorption line-width.

### 7.2.1 Trace molecular concentration measurements

In this section, we present a series of trace molecular concentration measurements in the 1.5-1.7 $\mu$m spectral region made using the CE-DFCS system shown in Fig. 7.3a. These measurements are meant to demonstrate the capabilities of our trace detection system and provide examples of real-world applications of CE-DFCS technique. The frequency comb used for this system was a 35 mW average power $Er^{3+}$ fiber laser with $f_r$= 99 MHz. This laser generates a 100 nm spectrum from 1.5 to 1.6 $\mu$m. For measurements in the 1.6-1.7 $\mu$m spectral region, a Raman

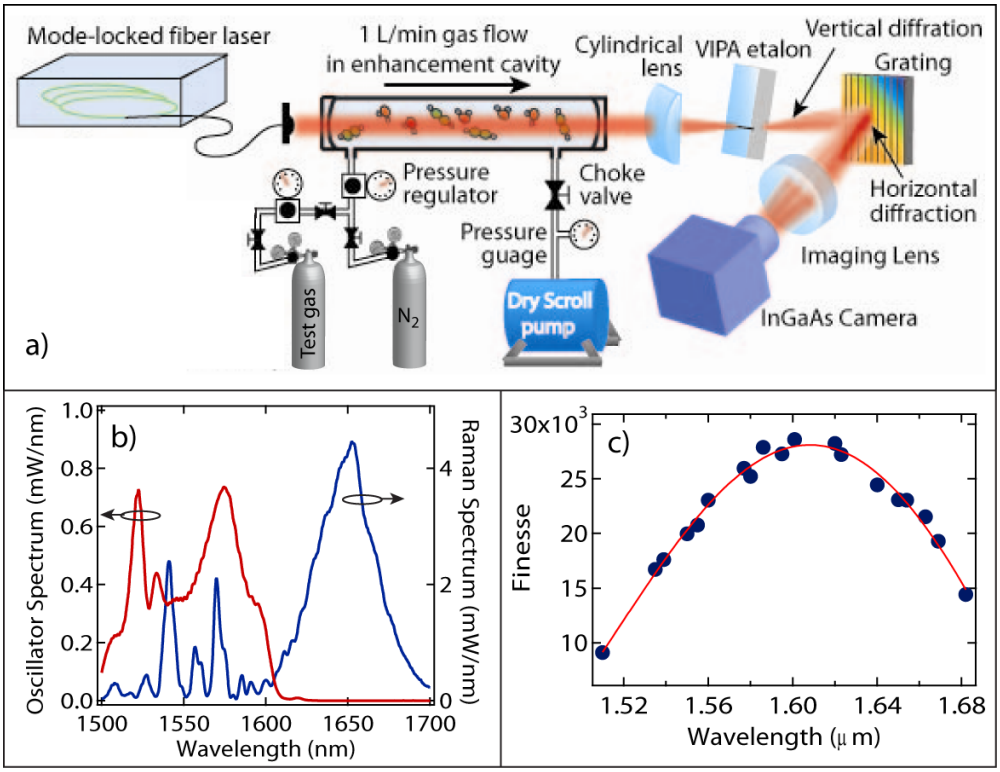


Figure 7.3: a) Schematic of the 1.5 $\mu$m CE-DFCS trace detection system. b) Spectrum directly from the laser (right) and the spectrum from the Raman-shifting amplifier (left). c) The wavelength dependent finesse of the detection cavity.

shifting amplifier is used to shift the spectrum and increase the average power to 300 mW (Fig. 7.3b) [98]. The detection cavity had an FSR of 99 MHz with a peak finesse of 28,000 at 1.61 $\mu$m (Fig. 7.3c). The comb was coupled to the cavity via swept frequency coupling and transient CEAS measurements were performed. A VIPA spectrometer was used in cavity transmission to achieve a 25-nm single shot bandwidth and 800 MHz resolution.

To characterize the absorption sensitivity of the system we performed measurements of the cavity transmitted light with the VIPA spectrometer centered at 1.61 $\mu$m and only dry nitrogen in the detection cavity. We recorded two consecutive VIPA images that were converted into an absorption spectrum using the procedure outlined in Section 6.3.4. The residual noise from these measurements

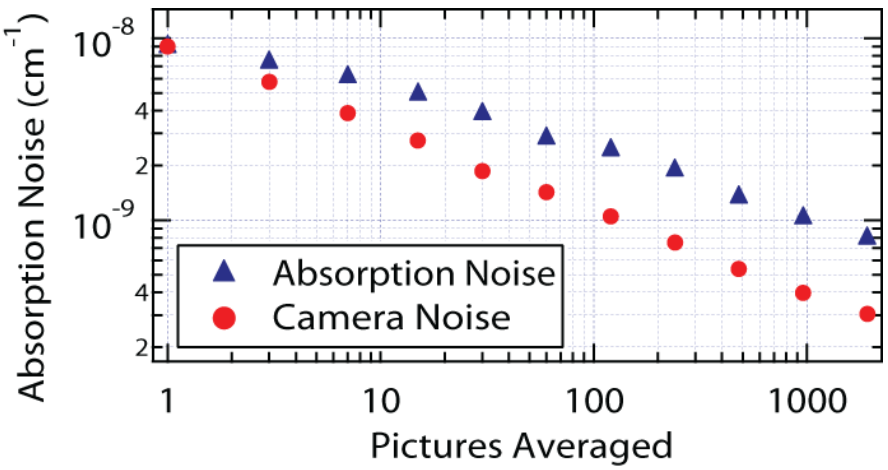


Figure 7.4: The absorption noise versus number of measurements at 1.61 $\mu$m.

are plotted in Fig. 7.4 against the number of pictures that were averaged to make the measurement. The upper data set (red) shows the residual noise when the cavity transmitted light was incident on the camera and the lower data set (blue) shows the noise when the cavity transmitted light was blocked from the camera. The camera frame rate for these measurements was 60 Hz. Therefore, ~30 s were required to average 2000 pictures at which point the residual absorption noise was $8\times10^{-10}$ cm$^{-1}$ per detection channel.

For these measurements there are several effects to consider in order to optimize the spectrometer performance. The equation that relates the absorption coefficient measured by the spectrometer to the gas concentration is [145]

$$\alpha(\nu) = \rho S_i g(\nu). \tag{7.1}$$

Here, $\alpha$ is the absorption per unit length (cm$^{-1}$), $\rho$ is the gas concentration (cm$^{-3}$), $S_i$ is the transition strength (cm), and $g(\nu)$ is the absorption line-shape (cm). The values for $S_i$ can be measured, found, or inferred from a variety of references [146] [147]. Although the values for $S_i$ have a strong temperature dependence, all trace concentration measurements presented in this section were made at a temperature of 296 K and so the values of $S_i$ will be treated as constants for the present

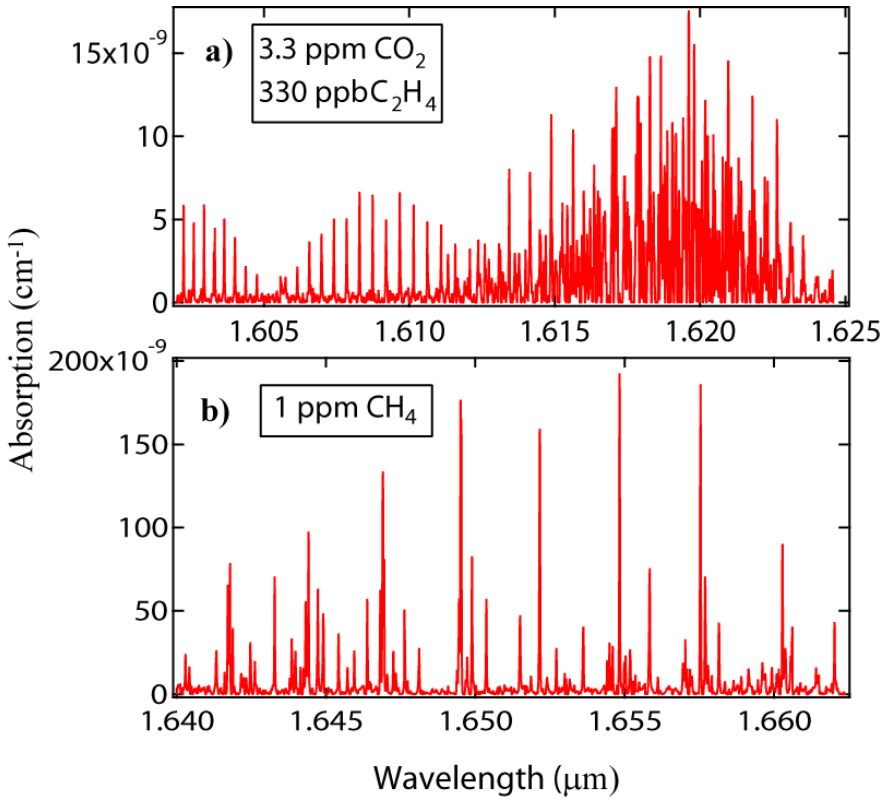


Figure 7.5: The rovibrational overtone spectra of a) 330 parts per billion (ppb) $C_2H_4$ and 3.3 ppm $CO_2$ and b) 1 ppm $CH_4$.

discussion [148]. The temperature dependence of $S_i$ will be discussed in detail in Section 7.3.2. The absorption line-shape depends on both the temperature and pressure conditions of the measurement. In particular, choosing the appropriate intra-cavity gas pressure is important for maximizing the molecular absorption while not diminishing spectral resolution via collision broadening. The gases that were measured and analyzed in our 1.5 $\mu$m CE-DFCS system include: CO, $CO_2$, $C_2H_2$, $C_2H_4$, $CH_4$, and $NH_3$. Parts of the recorded spectra for each of these gases are shown in Figs. 7.5 and 7.6. Since these trace gases are measured in a host gas of $N_2$, the air broadening coefficient adequately describes the observed collision broadening. For the measurements presented in this section, an intra-cavity gas pressure of 250 Torr was chosen such that the average line-width for a gas under

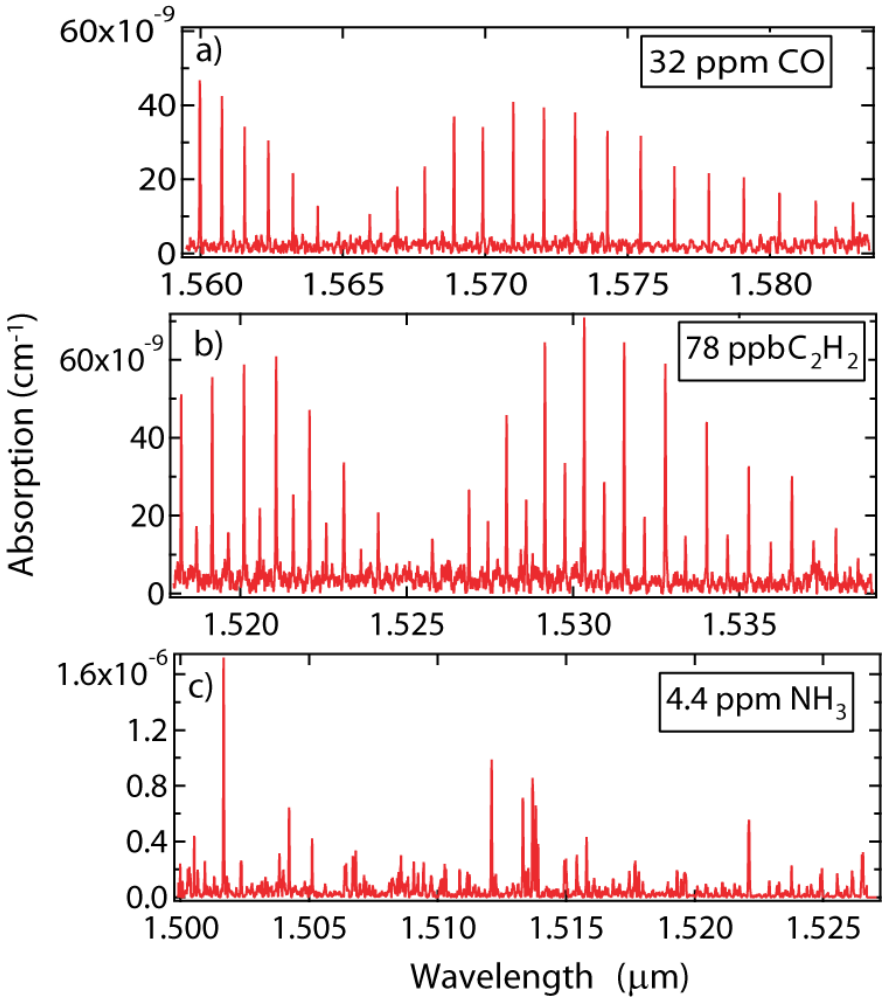


Figure 7.6: The rovibrational overtone spectra of a) 32 ppm CO, b) 78 ppb $C_2H_2$, and c) 4.4 ppm $NH_3$.

measurement was 1.8 GHz, resolvable by the 800 MHz resolution of our system.

For the molecules studied by this system, the spectral window between 1.5 $\mu$m and 1.7 $\mu$m contains more than 10,000 individual lines for measurements at 296 K. To handle this large amount of information, we created a database containing the center frequency, line intensity, and the air-broadening coefficient of more than 60% of the existing lines. This database was compiled from a variety of sources [146][147][16]. Using this database, gas concentrations were determined for each molecule by performing modified Voigt fits for several absorption fea-

Table 7.1: Spectral location and minimum detectable concentration (MDC) of measured molecules using the 1.5 $\mu$m CE-DFCS system.

| Molecule | Wavelength ($\mu$m) | MDC |
|---|---|---|
| CO | 1.56-1.62 | 900 ppb |
| $CO_2$ | 1.56-1.62 | 770 ppb |
| $CH_4$ | 1.63-1.69 | 10 ppb |
| $C_2H_2$ | 1.51-1.54 | 3 ppb |
| $C_2H_4$ | 1.61-1.65 | 33 ppb |
| $NH_3$ | 1.50-1.55 | 15 ppb |

tures that also included the resolution of the VIPA spectrometer. By finding the value of the instrument resolution that provided the best fit to the experimentally recorded line-shapes, an instrument resolution of 800 MHz was experimentally verified.

Calibration of the spectrometer was performed using three gas mixtures containing a total of four target gases consisting of 10 parts per million (ppm) $CO_2$, 1 ppm $CH_4$, 1 ppm $C_2H_4$, and 1 ppm $NH_3$, all mixed in high purity $N_2$. The accuracy of trace gas concentrations was specified to within 1% of the total concentration by Airgas, the supplier of our calibration gases. Since the spectral lines from these four molecules cover the entire spectral region from 1.5 $\mu$m to 1.7 $\mu$m, we were able to verify the calibration of the absorption loss provided by the cavity transmission equation (Eq. 5.3) for the entire spectral region. Finally, we made mixtures of CO and $C_2H_2$ by mixing pure samples of these gases with $N_2$ to determine the minimum detectable concentrations of these gases. These results, along with their detection wavelengths, are listed in Table 7.1.

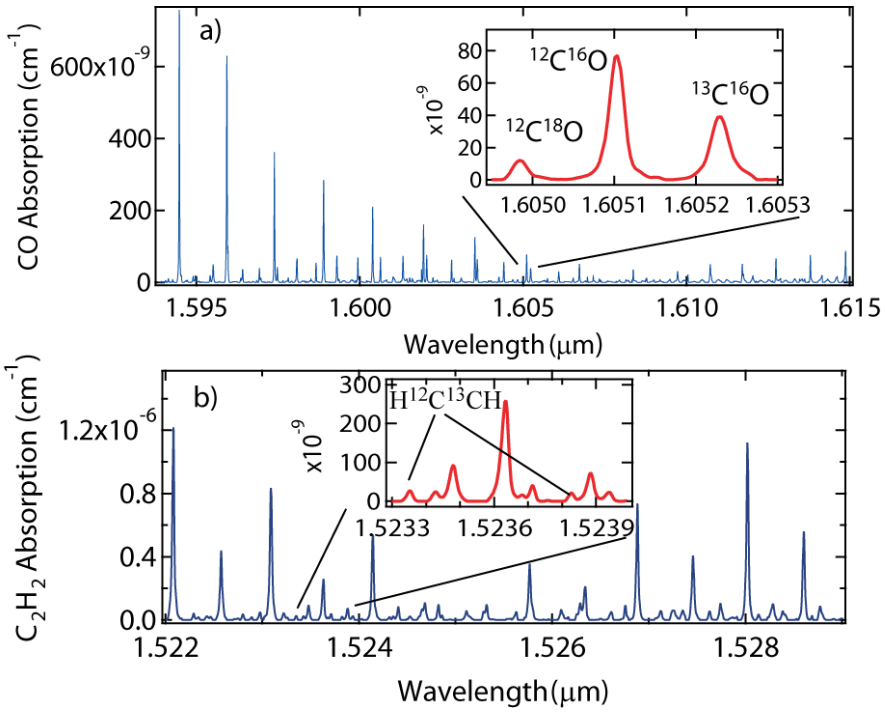


Figure 7.7: a) The isotope spectrum of CO near 1.605 $\mu$m at a CO concentration of 4.5 parts per thousand. b) The isotope spectrum of $C_2H_2$ near 1.524 $\mu$m at a $C_2H_2$ concentration of 2.2 ppm. The unlabeled lines in the $C_2H_2$ spectrum are $^{12}C_2H_2$ while the labeled lines are $H^{12}C^{13}CH$.

### 7.2.2 Isotope ratio measurements

A powerful demonstration of the sensitivity, dynamic range, and resolution of our spectrometer can be made via isotope measurements. During the course of measuring the spectra of CO, $CO_2$, $C_2H_2$, $H_2O$, and $CH_4$, we recorded spectral regions that contain multiple isotopes of all of these molecules. Figure 7.7 shows the spectra of CO and $C_2H_2$ containing multiple isotopes. For both CO and $C_2H_2$, the relative abundances of the isotopes measured by our system matched those found in the HITRAN database to within 0.4%. We also estimated the minimum concentration of CO and $C_2H_2$ that would allow detection of the second most abundant isotope to be 200 ppm for CO and 200 ppb for $C_2H_2$.

The ability to accurately measure molecular isotope ratios has found impor-

tant applications in many fields of science. For instance, doctors use stable isotope ratios of $^{13}CO_2$ on the breath of patients to detect *Heliobacter Pylori* for diagnosing ulcers [149]. Geologists use stable isotopes of $H_2O$ to investigate the transport of groundwater sources [150]. Climatologists and paleontologists use stable isotopes of $O_2$ to determine the past temperature of the Earth's atmosphere from ice cores [151]. These examples represent just a few of the useful applications of stable isotope ratio measurements.

### 7.2.3 Human breath analysis

Another emerging application of trace gas detection is human breath analysis. To date, researchers have identified over 1000 different compounds contained in human breath. These molecules have both endogenous and exogenous origins and provide information about physiological processes occurring in the body as well as environment-related ingestion or absorption of contaminants [50] [152]. While the presence and concentration of many of these molecules are poorly understood, many 'biomarker' molecules have been correlated to specific diseases and metabolic processes. Such correlations can result in non-invasive methods of health screening for a wide variety of medical conditions. Several methods of trace molecular detection have been applied to the problem of breath analysis including optical detection [149][17], mass spectrometry [153][154], and electronic noses [154] [155].

To understand the choice of optical detection as the preferred technique for breath analysis, we first evaluate the available techniques in the context of the system criteria. For instance, mass spectrometry (MS) is extremely sensitive and thus capable of detecting very small quantities of the analyte molecule. However, when several molecules are present, MS has difficulty identifying a single component of the mixture. To remedy this problem, MS is often used in conjunction

with gas chromatography to separate out various components of a mixture prior to measurement. While these hybrid systems are highly sensitive and accurate for a large number of biomarkers, they are also large, complex, and require a long period of time to perform a measurement [156]. Conversely, electronic nose devices are typically inexpensive and perform measurements rapidly. However, these devices, which are designed to measure volatile organic compounds, have difficulty distinguishing and accurately measuring concentrations of individual molecules from the group they are designed to detect [157]. Optical detection provides a good compromise as a general approach that can be applied to many molecules. The unique absorption spectrum of each molecule allows accurate identification and concentration measurements of a single molecule in the presence of many others. Furthermore, cavity enhancement techniques permit highly sensitive detection in a matter of seconds [130][158]. CE-DFCS is particularly well suited for breath analysis because of its wide spectral coverage allowing for detection of many different biomarkers simultaneously.

In the 1.5 $\mu$m to 1.7 $\mu$m spectral region, there are more than 10 biomarkers that exist in human breath in detectable quantities. The measurements presented in this section explore three of these biomarkers: CO, $CO_2$, and $NH_3$. These measurements were performed using the 1.5 $\mu$m trace detection system described in the previous section.

Our protocol for collecting breath samples to be measured requires that the test subject first take one deep breath. Next, the subject inhales normally and the breath is held for five seconds. Finally, the first half of the breath is released into the air before the second half of the breath is exhaled into the 1 liter Tedlar sample bag shown in Fig. 7.8. The use of only the second half of the breath sample increases the concentration of alveolar breath that is measured.

The first set of our breath measurements involves the analysis of stable iso-

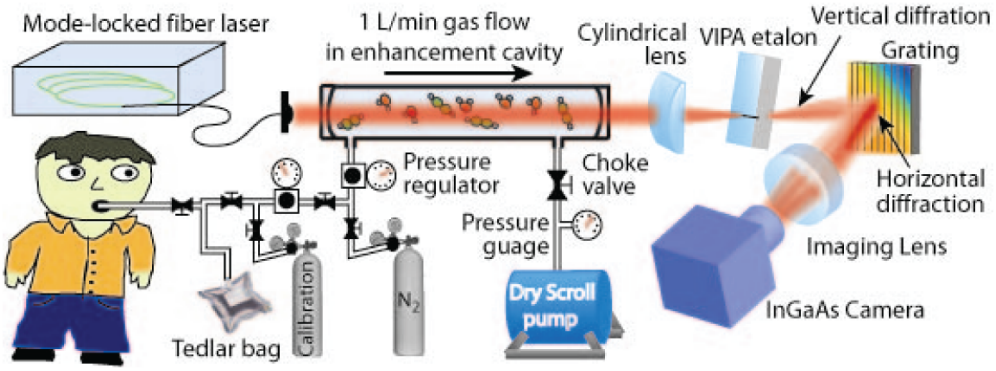


Figure 7.8: Schematic of the cavity-enhanced direct-frequency-comb spectrometer, with a modified gas handling system for breath analysis.

topes. Here we focus on measurements of $CO_2$ isotopes, but other isotopes such as $H_2O$ and $CH_4$ also exist in measurable quantities within our spectral region. Exhaled $CO_2$ is of a medical interest because the ratio of $^{13}C^{16}O_2$ to $^{12}C^{16}O_2$ can be used to determine if a patient is infected with *Heliobacter pylori*, a common cause of ulcers. This breath test is conducted by having the patient ingest a $^{13}$C-labeled urea and then measuring the ratio of $^{13}C^{16}O_2$ to $^{12}C^{16}O_2$ on the patients breath [159]. Increased levels of $^{13}C^{16}O_2$ indicate the presence of *H. pylori*, a bacteria that helps to convert the $^{13}$C-labeled urea into $^{13}CO_2$ before being exhaled in the patients breath.

Two spectral windows centered at 1.59 $\mu$m and 1.63 $\mu$m contain spectroscopic features of three isotopes of $CO_2$, all with roughly equal absorption strengths. Figure 7.9 shows the breath spectrum of a healthy graduate student in the window centered at 1.63 $\mu$m and illustrates a unique feature of broadband detection. In the spectral region shown in Fig. 7.9, there are 78 $^{12}CO_2$ absorption lines and 29 $^{13}CO_2$ lines. The two zoomed-in panels (a) and (b) both contain a number of spectral features for each of the three isotopes. By measuring many absorption lines and computing a concentration for each line, the overall accuracy of the isotope ratio measurement is enhanced by the square root of the number

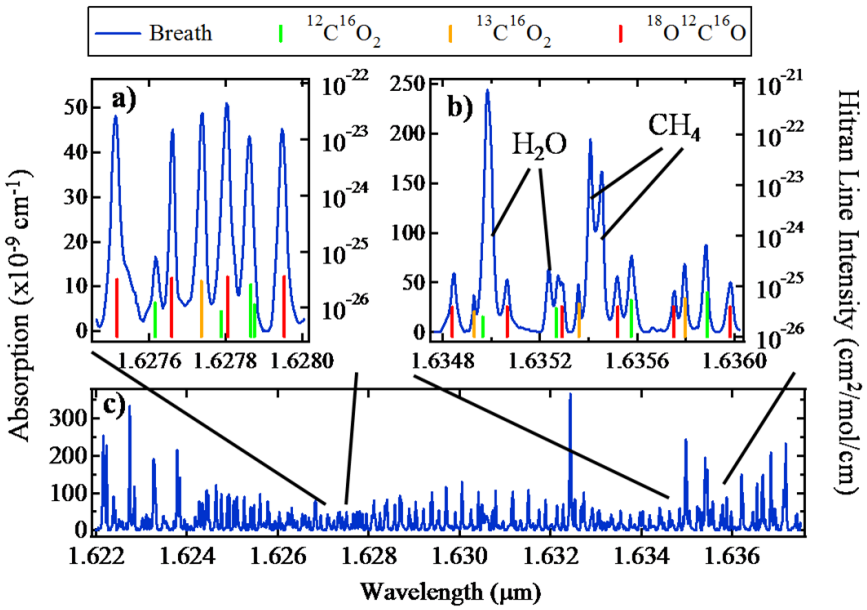


Figure 7.9: a)Breath spectrum of $CO_2$ isotopes near 1.63 $\mu$m. The inset shows a zoomed-in portion of the $CO_2$ landscape. The spectral region between 1.622-1.638 $\mu$m contains 78 $CO_2$ lines, 29 $^{13}CO_2$ lines, and 62 $^{18}O^{12}C^{16}O$ lines making it an ideal spectral region for determining isotope ratios.

of lines measured. To calculate the isotope ratios from the spectrum shown in Fig. 7.9c, a modest selection of 5 lines is chosen for each isotope. Typically, isotope measurements are expressed in parts per thousand such that $\delta$ = ($R_{sample}$ - $R_{standard}$)/$R_{standard}$ x 1000, where $R_{standard}$ is the natural abundance of the isotope and $R_{sample}$ is the abundance found in the breath sample [149]. For this measurement, we used the natural isotopic abundances reported in the HITRAN database to calculate the values of $R_{standard}$. Using this analysis we find that $\delta^{18}O$ = -9.1 $\pm$ 4.2 and $\delta^{13}C$ = -28.8 $\pm$ 4.1. The $\delta^{13}C$ ratio is currently the only breath biomarker that is used for widespread clinical diagnosis. However, the ability to measure other stable isotopes of $CO_2$ at increased accuracy, and the capability of measuring isotopes of other molecules such as $H_2O$ (1.55 $\mu$m) or $CH_4$ (1.65 $\mu$m), could significantly broaden the scope of future breath research.

The second breath measurement shown in Fig. 7.10 illustrates how environ-

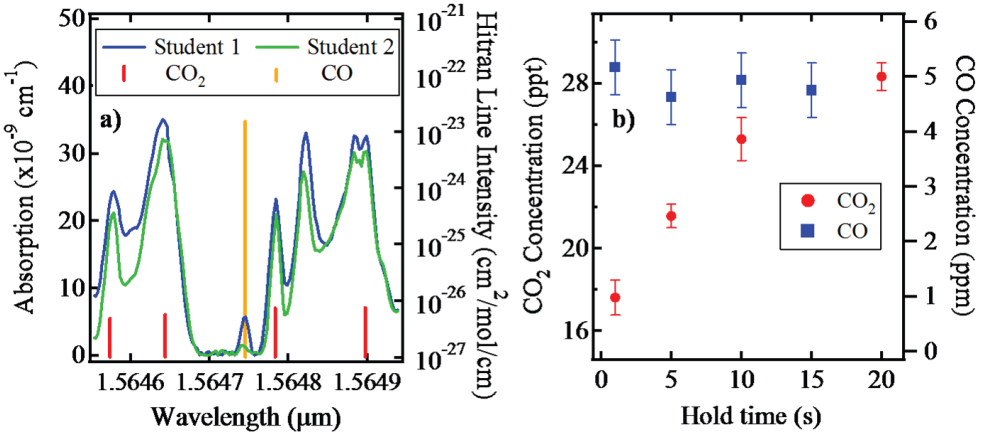


Figure 7.10: a) The $CO_2$ and CO absorption spectra of student 1 (smoker) and student 2 (non-smoker) in the 1.564 $\mu$m spectral region, along with line intensities from the HITRAN spectral database. The smoker's obvious increase in CO concentration is clearly detected. b) The breath concentration of $CO_2$ in parts per thousand (ppt) and CO in parts per million (ppm) as a function of time during which the test subject holds their breath prior to exhaling into the sample bag.

mental and behavioral factors that determine health can be monitored via breath analysis. Although CO has more than 170 spectral features between 1.55 $\mu$m and 1.61 $\mu$m, only one absorption line at 1.56474 $\mu$m does not overlap with interfering absorptions from $H_2O$ and $CO_2$. The measurement shown in Fig. 7.10a utilizes this spectral feature to detect the concentration of CO contained in the breath of two students. Student 1 is a smoker who had a cigarette 15 minutes prior to the beginning of the measurements while student 2 is a non-smoker. Both students provided five breath samples, each separated by 10 minutes. Both students exhibited constant levels of CO in their breath above the minimum detectable concentration of CO at 1.564 $\mu$m, which is 900 parts per billion (ppb). The average CO concentration measured for the smoker (6.5 ppm) was five times that of the non-smoker (1.3 ppm). While analyzing the data for the CO concentration, we noticed a small difference in the concentration of $CO_2$ exhaled by the two students (Fig. 7.10a). This observation led us to examine the sensitivity of our

concentration measurements to possible variations in our measurement protocol. In particular, we investigated both the CO and $CO_2$ breath concentrations as a function of time the test subjects held their breath prior to exhaling into the sample bag. Figure 7.10b shows these dynamic results. For $CO_2$, two separate measurements were taken at each hold time and five spectral features were used from each measurement for a total of ten samples to determine the concentration at each hold time. For CO, only a single measurement was taken at each hold time and consequently the error bars shown for CO correspond to the minimum detectable concentration of 900 ppb. This test shows that while the $CO_2$ concentration is quite sensitive to how long the test subject holds their breath, the CO concentration is not to within the statistical uncertainty of the measurement. Finally, a previous study of CO contained in the breath of smokers finds concentrations ranging from 1-68 ppm [160], indicating our system is capable of measuring CO breath concentrations for this entire population. While smoking provides an example of the behaviorial effect on the CO level in breath, environmental conditions can also lead to elevated CO breath levels. For instance, individuals who spend a large portion of their day in congested traffic or people live with elevated levels of CO at home are also prone to elevated CO levels in their breath [160].

The final breath-related measurement was the determination of the minimum detectable concentration of $NH_3$, a biomarker for renal failure that can be detected within a large concentration of $H_2O$. The absorption spectrum of $NH_3$ overlaps heavily with $H_2O$ in the spectral region from 1.5 $\mu$m to 1.55 $\mu$m. Two spectral windows, one at 1.513 $\mu$m and the other at 1.517 $\mu$m, were found to contain at least two strong $NH_3$ absorption lines that have minimal overlap with $H_2O$ absorptions (Fig. 7.11). To find these spectral windows and determine the minimum detectable $NH_3$ concentration, we measured the absorption spectrum of a calibrated sample of 4.4 ppm $NH_3$ in high purity $N_2$ and compared this

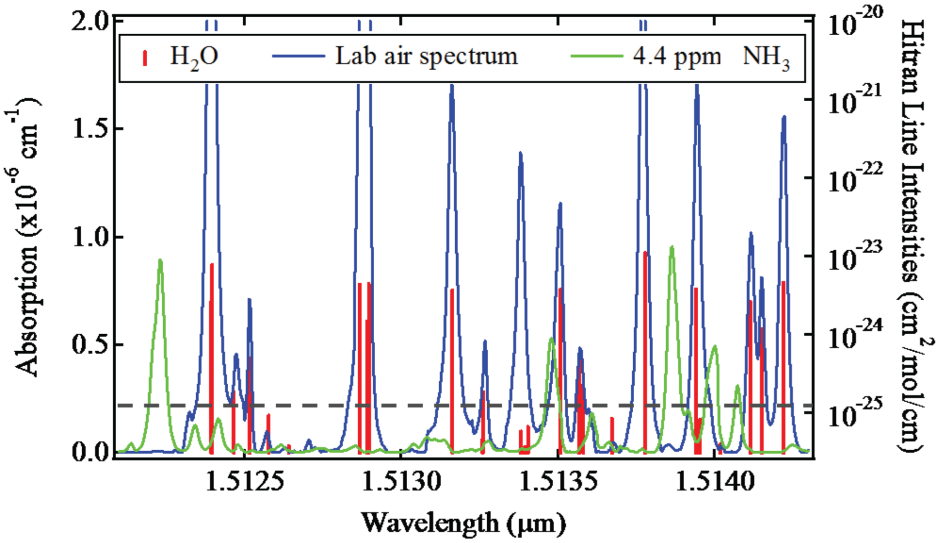


Figure 7.11: a)The absorption spectrum of lab air superimposed over the spectrum of 4.4 ppm of $NH_3$. HITRAN line intensities for $H_2O$ are included to identify the absorption features of the lab air spectrum. The dashed grey line represents the typical concentration of $NH_3$ contained in the breath of a patient at final stages of renal failure.

spectrum to both the lab air spectrum and the spectra generated from breath samples. The feature with the greatest $NH_3/H_2O$ absorption ratio was centered at 1.512231 $\mu$m. The minimum detectable concentration of $NH_3$ is considered to have a corresponding absorption feature that is twice the standard deviation of the measurement noise. According to this criterion, the minimum detectable concentration of $NH_3$ in the lab air at a 25% relative humidity was 18 ppb. Since our breath measurements nominally contain 3 to 4 times higher $H_2O$ concentration, small overlaps with $H_2O$ absorptions lead to slightly higher minimum detectable concentrations of ammonia in breath. Although this limit is still higher than detectable $NH_3$ present in the breath of most healthy individuals, it is sufficient to detect increased $NH_3$ present in the breath of people at early stages of renal failure (Fig. 7.11) [161].

The breath measurements presented here provide a modest glimpse of the

health information that can be acquired by analyzing a patient's breath. In the 1.5 $\mu$m spectral region alone there are also strong absorptions from methylamines which can be used to detect kidney failure and liver disease [162], acetone which is an indicator for diabetes [48], and ethane and ethylene for detecting lung cancer [13]. Currently the biggest obstacle to clinical application of breath analysis is the variation of breath samples from patient to patient, and the lack of a complete picture regarding how molecules contained in breath relate to disease and metabolic processes. The large number of biomarkers that can be measured using the CE-DFCS system, along with sub-minute measurement times, presents a cost effective way to accelerate research and future clinical applications of human breath analysis. With the rapid progress of frequency comb technology it most likely will not be long until commercial CE-DFCS instrumentations are available for this purpose.

## 7.3 Spectroscopy of jet cooled molecules

The measurements presented so far in this chapter have been on room temperature gas samples at relatively high pressures and therefore do not require higher spectral resolution than what is provided by the VIPA spectrometer. In this section, we discuss a technique that uses precise control of the comb and cavity frequencies in conjunction with a VIPA spectrometer to extend the spectral resolution far beyond the limitations of the VIPA spectrometer. We then show how the high resolution capability allows CE-DFCS systems to study molecular ensembles involving complex velocity and internal state dynamics. In particular, correlations between the internal energy states and external motions of molecular ensembles can be observed due to the simultaneous high resolution and broad spectral coverage the observation. This demonstration suggests that CE-DFCS will be an ideal tool for the emerging field of cold molecule

physics and cold chemistry, where experimental conditions involve small numbers of molecules, narrow resonances, and potentially many internal energy states for different species [49][47][163][164][165][166]. Indeed, femtosecond pulse trains and frequency combs are already being used for population transfer and coherent control of cold molecules [167][168][33] [169].

As a first effort in making a complete characterization of cold molecular ensembles with CE-DFCS, we have performed a tomographic reconstruction of absorption measurements from a supersonically cooled jet of $C_2H_2$ molecules. Tomographic reconstructions are enabled by the use of a movable jet nozzle, allowing us to measure the integrated absorption through the supersonic jet at a variety of distances from the nozzle and heights from the jet axis. The precise frequency control of the comb allows us to record the absorption line-shapes at each measurement position, while the broad spectral coverage of the comb allows us to record the entire $\nu_1 + \nu_3$ rovibrational band of $C_2H_2$ (both P and R branches) in a single measurement. As a result, the transverse velocity distributions of the molecules in the jet and their corresponding internal energy states are determined at the same time. Due to these capabilities, the use of CE-DFCS provides unprecedented advantages over previous supersonic jet studies that used Raman spectroscopy or contiunuous-wave cavity ringdown spectroscopy for supersonic beam investigations [170][171] [172][130]. The ability to simultaneously observe the internal and external energies of the molecular jet allows us to rapidly generate spatial maps of the density, velocity, and internal state distributions via tomographic reconstruction [173], essentially providing a thermodynamic snapshot of the entire jet.

The tomographic reconstructions presented in this section reveal several interesting features of the pulsed supersonic jet. First, we find spatially varying anomalous line-shapes that, to our knowledge, had not been previously reported. We also observe an anomalous rotational temperature map that suggests the cold-

est temperatures in the jet are not at the center, but rather form a ring around the axis of the jet. We also infer that the radial velocity is strongly correlated with the radial positions of the molecules in the beam. Finally, we present evidence indicating a transverse velocity dependence of the rotational cooling rate of the molecules within the expansion.

### 7.3.1 High-resolution spectroscopy of a supersonic jet of $C_2H_2$

For the this experiment, a cavity FSR of 700 MHz is chosen to be seven times that of $f_r$ (100 MHz) such that every seventh comb mode is coupled to the cavity. This choice of FSR acts to filter the comb modes as shown in Fig. 7.12 so that each molecular absorption line, having a nominal Doppler line-width of 350 MHz, only interacts with one comb mode. The comb teeth are rapidly swept over the cavity modes by modulating the laser $f_r$, and absorption measurements are performed using the technique of transient cavity-enhanced absorption spectroscopy [123][128]. The cavity is constructed from two 2-meter radius of curvature mirrors with a reflectivity of 99.95%, resulting in a finesse of 6300. The $TEM_{00}$ cavity mode has a 1/e electric field diameter of 1 mm which sets the spatial resolution limit of the tomographic measurements presented here. The Rayleigh range of the cavity mode is 50 cm such that its diameter is nearly constant over the length of the cavity. To avoid degrading the finesse by scattering loss from the supersonic expansion nozzle, the cavity mode must be positioned at least 2.5 mm from the nozzle. This requirement sets the minimum distance from the nozzle that measurements can be made with this system. Of course, engineering a smaller diameter cavity mode would allow for both higher spatial resolution and measurements closer to the expansion nozzle. One of the cavity mirrors is mounted on a 1 inch diameter ring PZT for servoing of the cavity length at bandwidths of up

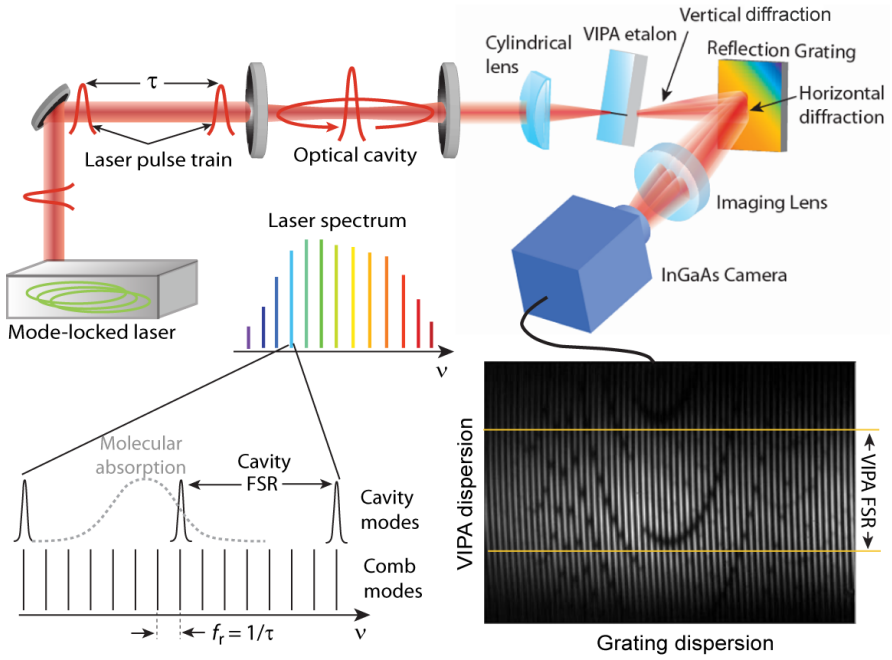


Figure 7.12: a) Schematic of the basic CE-DFCS system. A mode-locked laser generates a pulse train that is coupled into a high finesse detection cavity. The light transmitted from the cavity is analyzed using a VIPA spectrometer producing an interference image (bottom right). The parabolic patterns of dark spots are due to $CO_2$ absorption at 1.6 $\mu$m. The frequency diagram (bottom left) shows how the comb modes are coupled into the high finesse cavity. The molecular absorption line is measured by scanning both the comb and cavity modes over 1 FSR of the cavity.

to 1 kHz. Large changes to the cavity length are made by a resistive heater that holds the cavity at a nominal temperature of 35 °C.

The VIPA spectrometer is aligned to capture the cavity transmission within a 25 nm spectral range from 1.515 $\mu$m to 1.54 $\mu$m. The etalon used in this experiment has an FSR of approximately 50 GHz. A grating with 1100 lines/mm is used with a 20 cm focal length imaging lens to achieve a resolution of 25 GHz in the horizontal direction. As a result, the interference image in Fig. 7.12 shows dark stripes separating the bright vertical fringes, indicating that the mode orders of the VIPA etalon are well-resolved. We performed careful measurements of the VIPA FSR and position-dependent resolution of the spectrometer prior to the $C_2H_2$ jet

experiment. These measurements were made by observing the cavity transmitted absorption spectrum of a dilute sample of $C_2H_2$. Using the well-known transition frequencies of the $\nu_1 + \nu_3$ rovibrational band of $C_2H_2$, the VIPA FSR was determined to be 49.52 GHz [174][146]. The spatially varying spectrometer resolution was determined by comparing the spatial extent of absorption transitions that appeared at different heights on the interference image to the VIPA FSR interval. The VIPA spectrometer configuration used in this experiment had a resolution that varies from 1.0 GHz at the bottom of the FSR interval to 1.3 GHz at the top of the interval. Due to the 700 MHz spacing of the cavity transmitted comb modes and the Lorentzian transfer-function of the VIPA etalon transmission, each resolvable frequency channel recorded by the InGaAs camera samples an average of 2.5 comb modes. This acts to dilute the signal carried by each comb mode that interacts with the intra-cavity absorption. However, since only one comb mode is interacting with the molecular absorption within each resolvable channel, the frequency resolution of the measurement is not limited by the VIPA spectrometer, rather by the stability of individual comb modes.

To demonstrate high resolution and stable frequency measurements, the cavity mode frequencies are stabilized to within 700 kHz using a frequency stabilized Nd:YAG laser [175]. The comb frequencies are slaved to the cavity modes using a servo scheme described in Section 4.3. Frequency scans of the comb and cavity modes are performed by stepping the frequency of the 1.064 $\mu$m Nd:YAG laser in 25 MHz steps over 1 GHz, resulting in a 700 MHz (1 FSR) total scan of the cavity mode frequency at 1.525 $\mu$m made in 17.5 MHz steps. The 650 m/s average forward velocity of molecules moving through the 1 mm diameter of cavity mode results in a transit-time broadened line-width of 200 kHz. Accordingly, resolutions of better than 1 MHz can be achieved, which is more than sufficient to record the nominal Doppler limited line-width for molecules in the jet. Meanwhile,

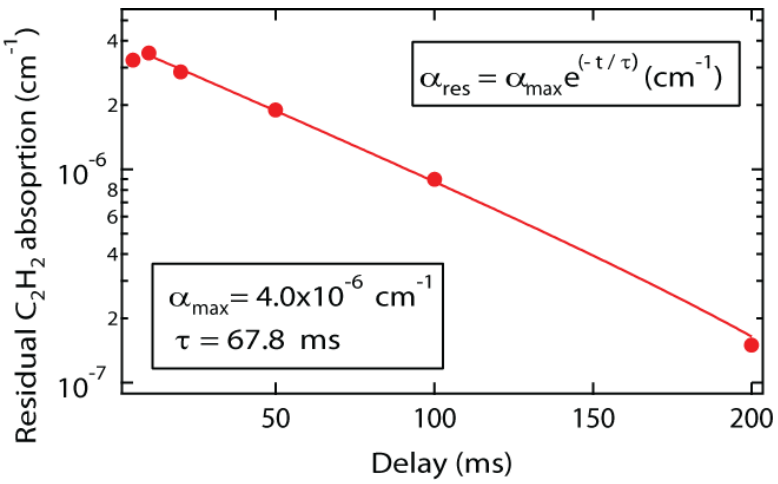


Figure 7.13: Residual $C_2H_2$ absorption of the R(1) transition versus time after firing the expansion valve.

the VIPA spectrometer easily captures the entire cooled rotational spectrum of the $C_2H_2$ molecules in a single measurement.

To create the pulsed supersonic expansion, a mixture of 2.5% $C_2H_2$ and 97.5% Ar at 650 torr is allowed to expand through a 1 mm diameter circular valve into an evacuated chamber with pressure $< 10^{-5}$ Torr. The nozzle was constructed with a pseudo-trumpet geometry shown in Fig. 7.18 as a compromise between ease of manufacturing and optimal cooling and forward collimation of the molecular beam [176]. A 2 Hz valve rate was chosen to allow adequate evacuation of the residual $C_2H_2$ inside the detection cavity before the again firing the valve. The data in Fig. 7.13 shows that the decay constant for residual $C_2H_2$ absorption on the R(1) transition inside the detection chamber is 68.7 ms. Therefore, after 500 ms, the residual R(1) absorption signal will be on the order of $\alpha_{max} e^{500/68.7} = 7 \times 10^{-7} \alpha_{max}$. Opening and closing of the value is actuated using a piezo-electric disc. The expanding jet of molecules is oriented perpendicularly to the mode of an optical cavity where CE-DFCS measurements are performed. The valve is mounted in a bellows and on translation stages, allowing control of

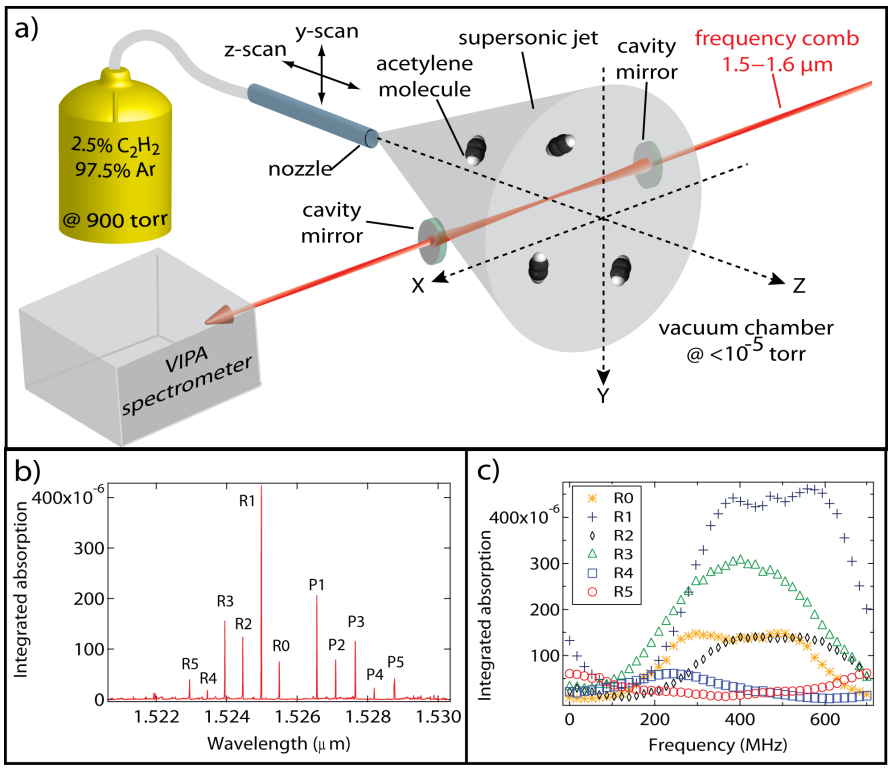


Figure 7.14: a) Schematic of the supersonic jet measurement via CE-DFCS. b) A snapshot of the rotational spectrum of the $C_2H_2$ beam at z = 6 mm, y = 1 mm. c) The peak absorption values for the R-branch transitions at z = 6 mm and y = 1 mm as the cavity length is scanned through one FSR in 17.5 MHz steps. The rotational spectrum snapshot in b) was captured at a frequency of 600 MHz during the scan in c).

the distance from the valve to the cavity mode (z-coordinate) and the height of the valve with respect to the cavity mode (y-coordinate) (Fig. 7.14a). Specifically, the z-coordinate is measured from the tip of the expansion nozzle (Fig. 7.18), and the y-coordinate is measured from the jet axis. Due to the mobility of the valve, line integrals along the cavity mode (x-coordinate) of the absorption through the beam can be performed at a variety of positions, allowing for tomographic reconstruction. The tomographic reconstructions are used to determine the exact position of the jet axis (y = 0 mm).

To characterize the time-dependent shape and forward velocity of our

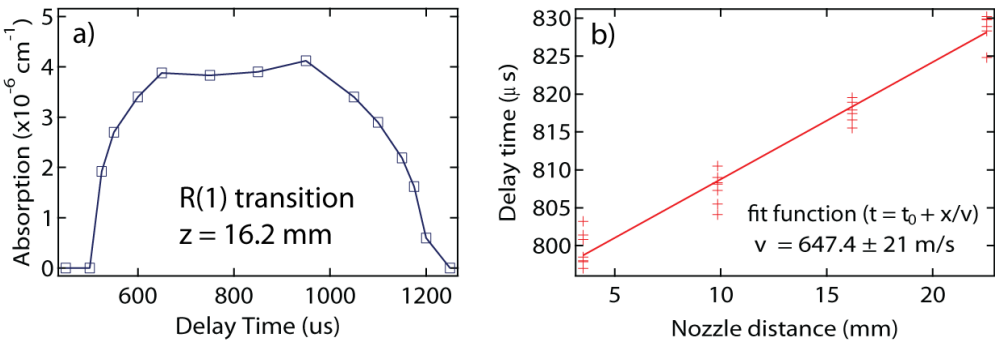


Figure 7.15: .a) The $C_2H_2$ pulse shape measured by scanning the delay between firing the valve and measuring the intra-cavity absorption of the R(1) transition. b) The delay time corresponding to the center of the R(1) absorption as a function of nozzle distance. Fitting the data points yields an average forward velocity of 647 ± 21 m/s.

molecular packet, we measured the pulse shape for y = 0 mm at four different distances from the nozzle (z = 3.5, 9.85, 16.2 & 22.55 mm). At each z-position we varied the time delay between opening the valve and performing the absorption measurement to map out both the pulse shape and the arrival time of the front edge of the pulse. The molecular pulse shape resembled a plateau with sharp front and back edges and a flat top at all measurement positions (Fig. 7.15a). From these measurements, we determined that the average forward velocity of our jet was 647 ± 21 m/s. The repeatability of these measurements indicated that our control of the valve opening time was better than ±5 $\mu$s.

Figure 7.14b shows the cooled $C_2H_2$ rotational spectrum at a distance of z = 6 mm from the nozzle. This spectrum is an average of 10 measurements for a total acquisition time of 5 seconds. Frequency scans of the cavity over one FSR are made by successively changing the cavity length to map out the entire frequency spectrum within the 25 nm bandwidth of the VIPA spectrometer. Figure 7.14c shows a one FSR frequency scan of the peak absorption wavelengths of the 0 through 5 transitions of the R-branch. This scan was performed in approximately 30 minutes, and yielded line-shape measurements for each of the P and R

branch transitions. For the frequency scans in Fig. 7.14c, the valve height was y = 1 mm such that the cavity mode was approximately 1 mm below the axis of the molecular beam. The minimum detectable integrated absorption of the system is $1 \times 10^{-6}$ at 1 ms of integration time. For the typical temperature and diameter of our beam (T = 10 K and d = 1 cm), the minimum detectable concentration of $C_2H_2$ is $1.7 \times 10^{11}$ cm$^{-3}$.

### 7.3.2 Tomography of a supersonic jet of $C_2H_2$

Our measurements in this experiment were restricted to parallel integrated absorption measurements as a function of height from the jet axis due to our setup. Since our scheme provides measurements at only one angle through the supersonic jet, our tomographic reconstructions are limited to distributions that are axis-symmetric [173]. In this case, an inverse Abel transform is used to convert the single set of parallel integrated absorption measurements into a radial absorption distribution $\alpha(r)$, where $r$ is the radial position [173]. We justify our assumption of a radially symmetric jet based on our use of the cylindrically symmetric nozzle shown in Fig. 7.18. Furthermore, we have performed frequency scans of the integrated absorption both above and below the jet axis which yield very similar absorption lines, both in shape and intensity. Evidence of the agreement between above and below axis measurements can be seen by comparing the y = -1.1 mm and y = 0.9 mm measurements in Fig. 7.16a. For jets that lack axial symmetry, our general approach can still be implemented; however, the number and type of measurements required to reconstruct the beam are significantly more extensive. In the asymmetric case, sets of parallel height-dependent measurements must be performed at a variety of angles covering 180° through the jet, and the more complicated Radon transform must be implemented to reconstruct the asymmetric

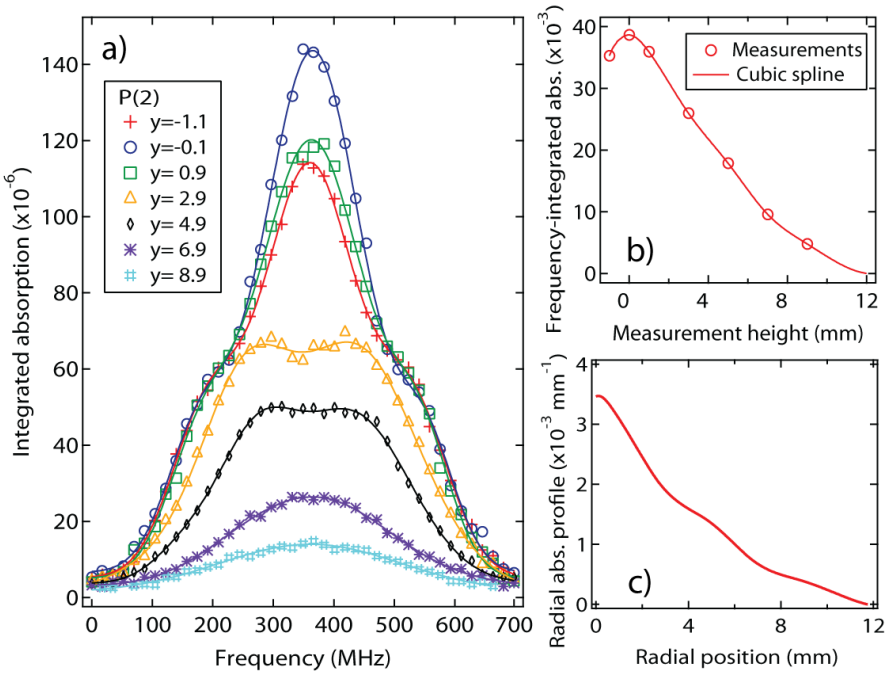


Figure 7.16: a) Integrated absorption frequency scans of the P(2) transition at a distance of z = 11 mm from the nozzle for several heights of the cavity mode with respect to the axis of the expansion. b) The data from a) are frequency-integrated and plotted versus the measurement height. A cubic spline of this data is performed in preparation for the inverse Abel transform. c) The inverse Abel transform of the cubic spline curve in b) results in a radial absorption profile.

absorption distribution $\alpha(r, \phi)$ [177].

The steps for performing tomographic reconstructions of the radial absorption distribution are shown in Fig. 7.16 using data from the P(2) transition at a nozzle distance of z = 11 mm. First, each of the integrated absorption line-shapes is fit to a sum of three Gaussians (Fig. 7.16a). This fitting function was chosen because it provided an excellent fit to every absorption line-shape that we observed. The triple Gaussian line-shape implies that the distribution of rotational ground states are populated differently in the center of the beam than in surrounding region. This is a point that will be discussed in more detail in conjunction with Fig. 7.19. Next, the fitted curves at each height were integrated along the frequency axis yielding net absorption versus height (Fig. 7.16b). The data points

in Fig. 7.16b were interpolated using a cubic spline. Finally, the spline of the integrated absorption data was converted to a radial absorption distribution using the inverse Abel transform:

$$\alpha(r) = -\frac{1}{\pi}\int_{r}^{\infty}\frac{d\alpha(y)}{dy}\frac{dy}{\sqrt{y^2 - r^2}}. \tag{7.2}$$

Here, $\alpha(y)$ represents height-dependent integrated absorption measurements (integrated along the cavity mode (x) and the optical frequency ($\nu$)), and $\alpha(r)$ is the radial absorption distribution. Since this integral has a singularity at $y = r$, direct integration of this transform results in inaccurate reconstructions of radial distribution. Consequently, there is an extensive literature concerning various algorithms that can be used to overcome the singularity issue. We have selected a discrete inverse Abel transform algorithm based on an eigenvalue approach to provide rapid and accurate tomographic reconstructions of the radial absorption profile [178]. An example MATLAB code for executing this algorithm is provided in Appendix D.

Using the above procedure, the radial absorption distributions were calculated for each R-branch rotational transition at the nozzle distance z = 11 mm as shown in Fig. 7.17a. The rotational absorption distribution at each radial position can be used to determine the molecular rotational temperature and density distributions via the relation $\alpha(\nu) = \rho S_i g(\nu)$ introduced in section 7.2. When the molecular ensemble is in thermal equilibrium, the line intensities ($S_i$) of the rotational transitions can be described by a Boltzmann distribution [148][179]

$$S_i = g_I L_i \nu C s_i, \text{ where } s_i = \frac{e^{-\frac{E_j}{k_B T_R}}}{Q_r}. \tag{7.3}$$

Here, j is the ground state rotational quantum number, $E_j$ is the ground state energy of the $j^{th}$ rotational level, $g_I$ is the nuclear spin state degeneracy (3 for odd and 1 for even rotational ground states), $k_B$ is the Boltzmann constant,

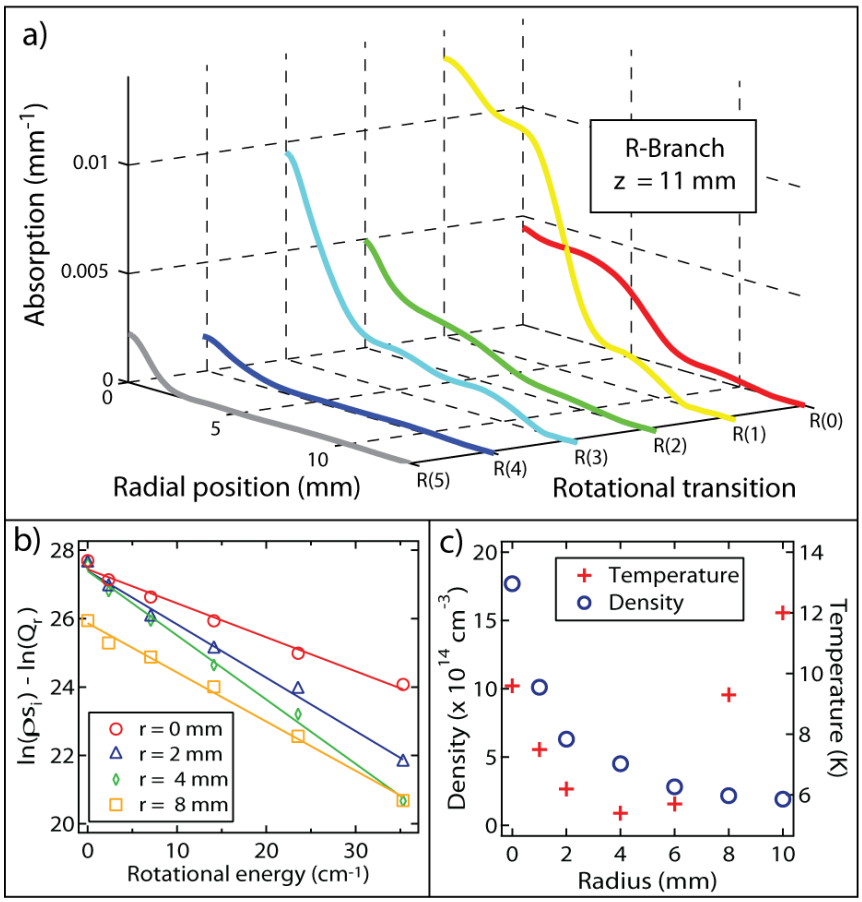


Figure 7.17: a) Tomographically reconstructed radial absorption profiles for the R-branch transitions at a distance of z = 11 mm from the nozzle. b) The density and rotational temperature of the jet are determined by fitting of the rotational absorption profile to a Boltzmann distribution at several radii from the beam axis. c) The radial density and rotational temperature distributions from the fits in b) show that the $C_2H_2$ density is largest on the beam axis with a steady decrease toward the edge of the beam. Counterintuitively, the radial temperature distribution reveals a warmer temperature of 9 K at the center of the beam that reduces to 5.5 K at r = 4 mm before warming to 12 K near the edge of the jet.

and $T_R$ is the rotational temperature of the molecular ensemble. $L_i$ is the Höln-London factor, $\nu$ is the rovibrational transition frequency, and $C$ is a constant that includes the vibrational transition dipole moment and a collection of other physical constants [148]. The quantity $Q_r$ in the denominator is the rotational

partition function and has the form

$$Q_r = \sum_j g_I(2j+1)e^{-\frac{E_j}{k_B T_R}}. \tag{7.4}$$

Equation 7.3 and the expression for $\alpha(\nu)$ are used in a fitting procedure to determine first the rotational temperature and then the density of the molecular ensemble as a function of $r$. The temperature is determined by fitting the exponential decay of each rotational transition as a function of the rotational ground state energy (Fig. 7.17b). To generate the data points in Fig. 7.17b the absorption values are divided by both the pre-factors in Equation (7.3) and the absorption line-shape $g(\nu)$, leaving only $\rho s_i$. We then take the natural logarithm of the data so the changes in rotational temperature and density can be more easily visualized as linear relationships rather than decaying exponentials. The rotational temperature at each $r$ is obtained from the slope of the linear fits. Once the rotational temperature of the ensemble has been determined, the rotational partition function can be calculated. Using the partition function, the molecular density can be determined from the the y-intercept of the fits. The fit results for seven radial positions are shown in Fig. 7.17c. As expected, the molecular density is largest on the jet axis and decreases steadily with increasing radius. More interesting is the radial dependence of the rotational temperature of the supersonic jet. The coldest rotational temperature observed does not appear at the center of jet. Instead, a temperature of 9 ± 0.9 K is observed on the jet axis, the temperature then drops to 5.5 ± 0.7 K at $r$ = 4 mm before rising to 12 ± 1.6 K at the edge of the jet (r=10 mm).

To gain a better understanding of how the jet evolves as it expands from the valve, we have performed height and frequency scans at five distances from the nozzle (z = 3.5, 6, 8.5, 11, & 13.5 mm). The procedures described in Figures 7.16 and 7.17 were used to convert the integrated absorption measurements into den-

sity and rotational temperature distributions at each measurement distance. The radial distributions calculated for each z-position were then combined into a 2D 'map' describing the rotational temperature and density distributions $(z, r)$ within the measurement volume. To generate a smooth plot of the spatial-varying rotational temperature and density, a 2D spline was used to interpolate between the five radial distribution curves. The resulting 2D density and rotational temperature maps are shown in Fig. 7.18. The data used to construct this map, acquired at a 2 Hz valve rate and without an automated system for moving the nozzle, was recorded in 28 hours of measurement time.

The density map on the right side of Fig. 7.18 shows a well collimated and high molecular density region centered on the jet axis. The collimated packet is surrounded by a lower density cloud of molecules that expands as a function of distance from the nozzle. The most prominent feature of the rotational temperature map is the well understood cooling of the rotational temperature as a function of distance from the nozzle [180]. However, the temperature map also shows a more subtle effect. The coldest rotational temperatures are not located on the jet axis. Rather, this temperature minimum exists in a ring around the jet axis. Also, the radius of this ring appears to increase with increasing distance form the nozzle. To verify the results of our tomographically reconstructed temperature map, we performed a couple of confirmation checks to make sure that what we observe does not arise from a systematic error in either our absorption measurements or our procedure for tomographic reconstruction. First, we analyzed the P-branch data and found that the tomographic reconstructions for both the density and temperature maps were in good agreement with the maps derived from the R-branch measurements. To rule out systematic error in our tomographic reconstruction procedure, we performed a two-exponential (or two-temperature) fit of the rotational distributions for the height-dependent integrated absorption

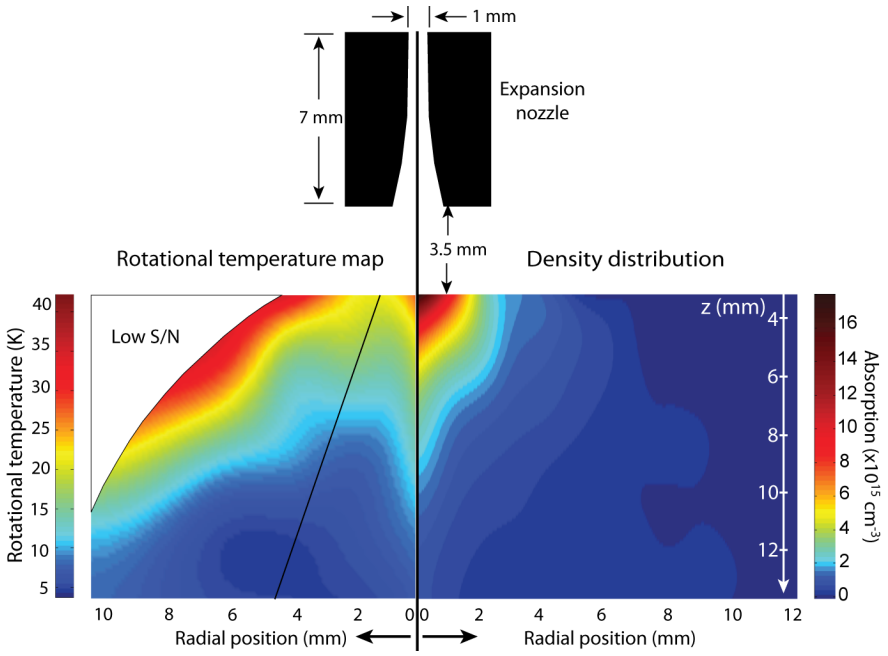


Figure 7.18: A scaled drawing of the supersonic expansion nozzle is shown above tomographically reconstructed 2D $(z, r)$ maps of the rotational temperature (left) and density (right). The temperature map reveals the typical rotational cooling as a function of distance from the nozzle. The radial temperature distribution shows that the coldest molecules in the jet reside at a radial position that increases with increasing distance from the nozzle. The diagonal black line on the temperature map defines a molecular trajectory corresponding to molecules with a transverse velocity of 230 m/s. The significance of this trajectory will be discussed in conjunction with the absorption line-shapes shown in Fig. 7.19. The density distribution shows a well collimated jet centered at r = 0 mm surrounded by an expanding cloud of lower density molecules.

measurements. These fits showed a higher rotational temperature for the y = 0 mm measurements, which then decreased as the values of y increased. Finally, the temperature indicated by the fits increased toward the edge of the jet. In short, we confirmed that the temperature map in Fig. 7.18 faithfully represents the position-dependent rotational temperature of the beam.

To gain some insight into the cause of the observed rotational temperature distribution, we turn our attention to position and rotation dependance of the integrated absorption line-shapes. The absorption line-shapes for the R-branch

transitions 0-5 measured at y = 0 mm are shown in Fig. 7.19a for nozzle distances of z = 3.5 mm to z = 16 mm. To aid in the discussion of the line-shapes in Fig. 7.19a, we have divided the frequency axis of each graph into three regions (I, II, and III) as denoted in the R(0) graph.

One interesting feature of these line-shapes is shown in Fig. 7.19b. Here we have plotted the frequency-integrated absorption signals of the R(0) and R(5) transitions as a function of distance from the nozzle. To provide some context for these curves, consider what the frequency-integrated absorption signal would look like for a collisionless expanding jet with a Gaussian velocity distribution. As the jet begins to expand, the signal changes very little until the point where the jet diameter becomes larger than the optical detection beam (cavity mode). Beyond this point, the amplitude of the absorption signal will decrease as a function of distance from the nozzle at the asymptotic rate of $z^{-1}$. Also, as the amplitude decreases, the line-shape remains constant. In contrast, the signal for R(0) decreases at the much slower rate of $z^{-0.26}$ while the signal for R(5) decreases at the much faster rate of $z^{-2.1}$. The reason for the slow reduction of the R(0) signal and the fast reduction of the R(5) signal is due to rotational cooling of the molecules in the supersonic expansion.

Another interesting feature of the absorption lines are the anomalous shapes that differ considerably from the expected Gaussian line-shape. While anomalous line-shapes have been observed in a continuous beam of $C_2H_2$/Ar, those anomalies manifest as a dip in the center of the absorption line for the lowest rotations (j = 0, 1, 2), and were attributed to $C_2H_2$ clustering occurring at regions of high density within the beam [171]. In contrast, the low rotational state molecules in our measurements always exhibit peaks at the line-center. Furthermore, due to the large nozzle aperture and low stagnation pressure in our experiment compared to [171], we suspect that the primary cause of the line-shape anomalies observed

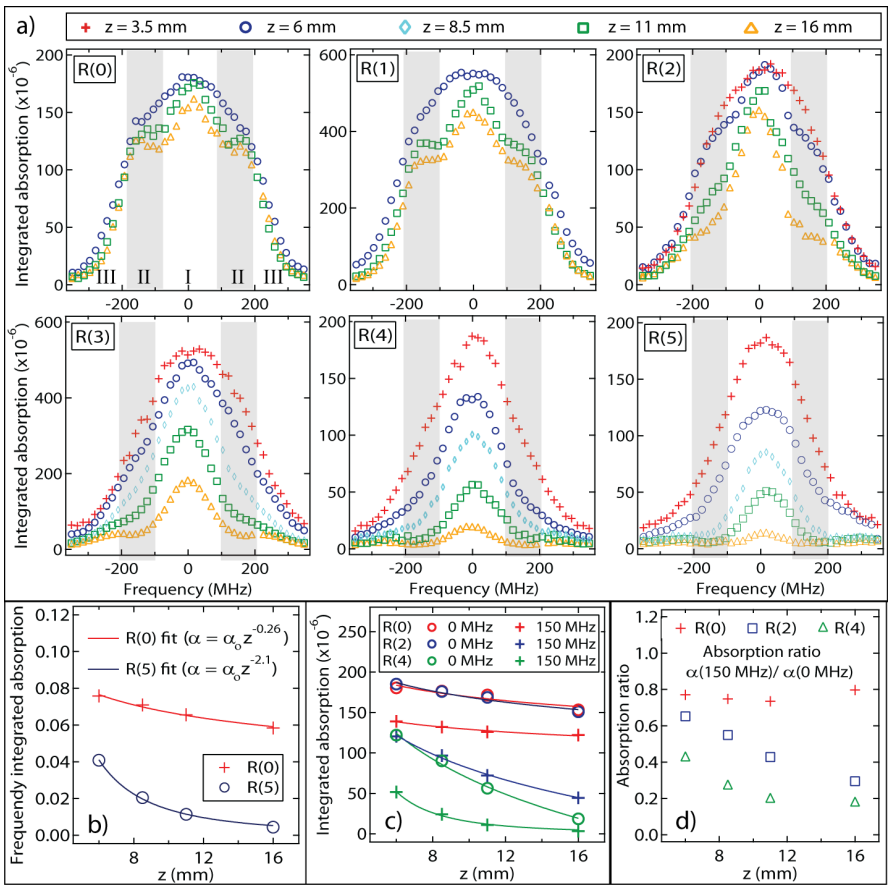


Figure 7.19: a) The absorption line-shapes for the R-branch transitions 0-5 measured through the jet axis at y = 0 mm for nozzle distances ranging from z = 3.5 mm to z = 16 mm. Each panel has been labeled with three regions of interest. The light area between the two shaded regions (I) shows the low transverse velocity behavior, the shaded regions (II) show the medium transverse velocity behavior, and the outer light regions (III) show the high transverse velocity behavior. b) The frequency-integrated absorption signals for R(0) and R(5) versus nozzle distance showing a signal decay that is slower than $z^{-1}$ for R(0) and faster for R(5). c) Frequency dependent integrated absorption signals for R(0), R(2), and R(4) at transverse velocities of 230 m/s and at 0 m/s. d) Absorption ratios of the $v_t$ = 230 m/s versus $v_t$ = 230 m/s molecules for transitions R(0), R(2), and R(4) show a faster decay of $v_t$ = 230 m/s molecules for the higher rotational levels.

here are not due to clustering [181].

The anomalies in our observations tend to occur at frequencies within the lightly shaded region II between 100 MHz and 200 MHz. In this frequency range we observe a depletion of the absorption signal for higher rotation molecules (j

= 2, 3, 4, 5) and an excess of signal for the low rotations (j = 0 and 1). The data in Fig 7.19c shows the absorption trends as a function of nozzle distance for the transitions R(0), R(2) and R(4) for the Doppler shift frequencies of 0 MHz ($v_t$ = 0 m/s) and 150 MHz ($v_t$ = 230 m/s). Since the nuclear-spin states are not changed by the rotational cooling of the supersonic expansion, the parity of the rotational ground states does not change [182]. Hence rotational cooling in the expansion proceeds in steps of $\Delta j = 2n$ where n is an integer. The data in Fig. 7.19c illustrates the transverse velocity dependence of the rotational cooling of molecules with even rotational ground states. At zero transverse velocity, the power law decay exponents of the absorption signals are -0.16, -0.2, and -1.5 for R0, R2, and R4 respectively, while at $v_t$ = 230 m/s the decay exponents are -0.14, -1, and -2.4. Comparing the two sets of decay exponents shows that the absorption signals for R(2) and R(4) decay much slower at $v_t$ = 0 m/s than at $v_t$ = 230 m/s. In contrast, the exponents for R(0) show a comparable decay of the $v_t$ = 0 m/s and $v_t$ = 230 m/s signals. This can be seen clearly in the ratios of the absorption at $v_t$ = 230 m/s versus $v_t$ = 0 m/s for each rotation (Fig. 7.19d). A further analysis of these decay exponents could be used to determine the population transfer rates between the different rotations. However, for the present work we only wish to point out that the population transfer seems to depend on the transverse velocity of the molecules within the jet.

The line-shape measurements and subsequent analysis shown in Fig. 7.19 can offer some insight into the interesting rotational temperature map of Fig. 7.18. Once again we consider the center frequency of the darkly shaded 'anomalous' regions in Fig. 7.19a ($f$ = 150 MHz), which has a transverse velocity of 230 m/s. This velocity and the average forward velocity of the jet ($v_f$ = 650 m/s), result in the trajectory illustrated by the diagonal black line in the rotational temperature map of Fig. 7.18. The interesting feature of this trajectory is that it closely

follows the minimum rotational temperature as the jet expands. Since the anomalous characteristic of this frequency range is a depletion of higher rotations and an excess of lower rotations, molecules at these velocities will exhibit a lower rotational temperature than other frequency regions. Furthermore, since this same temperature dependence is manifested in the position of the 'rotationally coldest' molecules in Fig. 7.18, it indicates that the transverse velocity of molecules in the jet are strongly correlated to their position in the jet. Again, further analysis could be implemented to determine the level of correlation between position and velocities of molecules within the jet.

The measurements presented in this section provide a general example of how CE-DFCS systems can be used to rapidly obtain highly detailed information about complex molecular ensembles. In particular, we have demonstrated how CE-DFCS is used to obtain simultaneous high sensitivity, high resolution, and broad-bandwidth spectroscopic measurements. In the jet cooled $C_2H_2$ study, the ability to rapidly record broad-bandwidth and high resolution spectra has allowed us to perform tomographic reconstructions of the density and temperature distributions of a $C_2H_2$/Ar supersonic expansion. These reconstructions reveal an interesting behavior of the position dependance of the rotational temperature distribution. Our ability to observe the absorption line-shapes of each rotational line as a function of distance from the nozzle allows us to interpret the anomalous rotational temperature distribution as resulting from a transverse-velocity dependent rotational cooling rate. Furthermore, comparing the position and line-shape data allows us to infer strong correlations between the radial velocity and the radial position of molecules in the supersonic jet.

# Chapter 8

# Conclusion

## 8.1 The state of the art

The techniques and measurements described in this thesis represent the current state of the art for cavity-enhanced direct frequency comb spectroscopy. As this is a relatively new field, the capabilities of these systems and the enabling technologies are improving rapidly. Already CE-DFCS has demonstrated detection of molecular concentrations in the low ppb range for many molecules and sub megahertz spectral resolutions. Furthermore, these detections have been performed rapidly and covering spectral ranges extending hundreds of nanometers.

Due to the preliminary successes and great potential of CE-DFCS for a wide variety of applications, we have submitted a patent application for this technology. We are currently in the final stages of the application process. After our demonstration of human breath analysis using CE-DFCS, we were approached by several companies who wanted to license our pending patent and develop CE-DFCS for applications ranging from breath analysis, to industrial process applications, to explosive and hazardous material detection. The breath analysis work has also excited many in the medical field due to the prospect of low cost and rapid medical screening. As a result, we have started several collaborations with medical researchers at institutes across the country to further advance the field of breath research. We hope that through commercial development and collaboration with

medical experts, we can eventually help CE-DFCS technology find its way into clinical applications.

The demonstration of broad bandwidth, high sensitivity, and high resolution spectroscopy of jet cooled molecules presents a different, but equally exciting direction for CE-DFCS. Here, the high resolution and broad spectral coverage are shown to beautifully tackle the challenges facing cold molecule community (i.e. the simultaneous high resolution investigation of many molecular transitions).

## 8.2 Current research and future directions

Currently, graduate student Kevin Cossel and postdoc Florian Adler are continuing to expand the trace detection applications of CE-DFCS. With my help, they have constructed a trace detection system that operates in the 1.75 $\mu$m to 2.05 $\mu$m spectral region. This system was designed to detect trace contaminants in gases that are used for producing semiconductors [12]. In particular, their system will look for traces of $H_2O$, $CO_2$, $CH_4$, $C_2H_6$, $SiH_4$, and potentially other contaminants in an atmosphere of pure $AsH_3$. If this system reaches the part per billion (ppb) level of detection for these contaminants, it would greatly benefit the semiconductor industry, since ppb level contamination of these compounds can drastically reduce the semiconductor performance.

The CE-DFCS technique has already began to spread to other groups within JILA. Eric Cornell and his student Laura Sinclair are currently designing a system to detect transitions in the poorly understood $HaF^+$ molecular ion. They have devised a clever combination of CE-DFCS and velocity modulation spectroscopy to separate the neutral molecule absorption signals from those that are due to the ions. Also, with the help of Jun and myself they will implement a scheme for coupling the comb to the cavity that combines principles of both the cavity

filtration and tight cavity locking schemes presented in Chapter 4. The goal of this spectroscopy is to identify transitions in $HaF^+$ that can be used to search for the electron electric dipole moment.

As applications of CE-DFCS systems become more demanding, the current limits of CE-DFCS systems will certainly be overcome. Directions for improving CE-DFCS performance include new broadband cavity designs such as prism cavities mentioned in Chapter 3. Such cavities would greatly increase the number of molecules that can be probed with a single CE-DFCS system by providing detection cavities with high finesse over very large spectral bandwidths. Current work with fused silica retro-reflecting prism suggests that a spectral bandwidth of 1 $\mu$m with a center wavelength of 1.5 $\mu$m can be achieved. This corresponds to a fractional frequency coverage of 75% of the center frequency.

Extending high-precision and high average power frequency comb sources to the mid-IR spectral region will also greatly enhance the capabilities of CE-DFCS systems. Mid-IR detection will enable extremely high sensitivity absorption measurements, due to the strong fundamental molecular vibration transitions, reducing the minimum detectable concentration of many molecules to the parts per trillion level. Also, hundreds of molecules have absorption signatures in the mid-IR spectral region greatly expanding the number of molecules that can be detected compared to the 1.0 to 2.0 $\mu$m spectral region. Toward this goal, we are currently developing an optical parametric oscillator (OPO) to generate up to 1 Watt of average power in the spectral range between 2.8 and 4.5 $\mu$m. The OPO will be pumped by a 5 Watt mode-locked Yb fiber laser and will provide a tunable spectrum using a fan-out type periodically poled lithium niobate crystal.

Aside from trace detection, new applications for CE-DFCS include detection and characterization of cold molecules, including their dynamics and interactions. High-resolution coherent control of atomic and molecular systems similar to work

already performed using free-space DFCS [32][183] represents another exciting possibility. Considering the progress up to this point, it is likely that future experiments and technological advances will allow CE-DFCS to be applied to many new areas of scientific inquiry and commercial application. Fortunately, the next generation of students working on these projects, Kevin and Florian, are already dreaming up the things to come.

## Bibliography


[1] T. W. Hänsch, I. S. Shahin, and A. L. Schowlow, Optical resolution of the Lamb shift in atomic hydrogen by laser saturation spectroscopy, *Nature* **235**, 63 (1972).

[2] D. J. Wineland, R. E. Drullinger, and F. L. Walls, Radiation-pressure cooling of bound resonant absorbers, *Phys. Rev. Lett.* **40**, 1639 (1978).

[3] T. W. Hänsch and B. Couillaud, Laser Frequency Stabilization By Polarization Spectroscopy of a Reflecting Reference Cavity, *Opt. Commun.* **35**, 441 (1980).

[4] R. W. P. Drever, J. L. Hall, F. V. Kowalski, J. Hough, G. M. Ford, A. J. Munley, and H. Ward, Laser Phase and Frequency Stabilization Using an Optical Resonator, *Appl. Phys. B* **31**, 97 (1983).

[5] D. Z. Anderson, J. C. Frisch, and C. S. Masser, Mirror reflectometer based on optical cavity decay time, *Appl. Opt.* **23**, 1238 (1984).

[6] A. O'Keefe and D. D. A. G., Cavity ring-down optical spectrometer for absorption measurements using pulsed laser sources, *Rev. Sci. Instrum.* **59**, 2544 (1988).

[7] M. H. Anderson, J. R. Ensher, M. R. Matthews, C. E. Wieman, and E. A. Cornell, Observation of Bose-Einstein Condensation in a Dilute Atomic Vapor, *Science* **269**, 198 (1995).

[8] M. Niering *et al.*, Measurement of the Hydrogen 1S-2S Transition Frequency by Phase Coherent Comparison with a Microwave Cesium Fountain Clock, *Phys. Rev. Lett.* **84**, 5496 (2000).

[9] M. V. Romalis, W. C. Griffith, J. P. Jacobs, and E. N. Fortson, New Limit on the Permanent Electric Dipole Moment of $^{199}$Hg, *Phys. Rev. Lett.* **86**, 2505 (2001).

[10] D. J. Wineland, C. Monroe, W. M. Itano, D. Leibfried, B. E. King, and D. M. Meekhof, Experimental Issues in Coherent Quantum-State Manipulation of Trapped Atomic Ions, *J. Res. Natl. Inst. Stand. Technol.* **103**, 259 (1998).

[11] W. Demtröder, *Laser spectroscopy*, 3 ed. (Springer-Verlag, Berlin, 2003), pp. 851–892.

[12] S. Y. Lehman, K. A. Bertness, and J. T. Hodges, Detection of trace water in phosphine with cavity ring-down spectroscopy, *J. Cryst. Growth* **250**, 262 (2003).

[13] C. S. Patterson, L. C. McMillan, C. Longbottom, G. M. Gibson, M. J. Padgett, and K. D. Skelton, Portable optical spectroscopy for accurate analysis of ethane in exhaled breath, *Meas. Sci. Technol.* **18**, 1495 (2007).

[14] S. Spuler, M. Linne, A. Sappey, and S. Snyder, Development of a cavity ring-down laser absorption spectrometer for detection of trace levels of mercury, *Appl. Opt.* **39**, 2480 (2000).

[15] M. W. Todd, R. A. Provencal, T. Owano, B. A. Paldus, A. Kachanov, K. L. Vodoyanov, M. Hunter, S. L. Coy, J. I. Steinfeld, and J. T. Arnold, Application of mid-infrared cavity-ringdown spectroscopy to trace explosives vapor detection using a broadly tunable (6-8 $\mu$m) optical parametric oscillator, *Appl. Phys. B* **75**, 367 (2002).

[16] E. H. Wahl, S. M. Tan, S. Koulikov, B. Kharlamov, C. R. Rella, and E. R. Crosson, Ultra-sensitive ethylene post-harvest monitor based on cavity ring-down spectroscopy, *Opt. Express* **14**, 1673 (2006).

[17] A. A. Kosterev, A. L. Malinovsky, F. K. Tittel, C. Gmachl, F. Capasso, D. L. Sivco, J. N. Baollargeon, A. L. Hutchinson, and A. Y. Cho, Cavity ringdown spectroscopic detection of nitric oxide with a continuous-wave quantum-cascade laser, *Appl. Opt.* **40**, 5522 (2001).

[18] D. J. Jones, S. A. Diddams, J. K. Ranka, A. Stentz, R. S. Windeler, J. L. Hall, and S. T. Cundiff, Carrier-Envelope Phase Control of Femtosecond Mode-Locked Lasers and Direct Optical Frequency Synthesis, *Science* **288**, 635 (2000).

[19] S. T. Cundiff, J. Ye, and J. L. Hall, Optical frequency synthesis based on mode-locked lasers, *Rev. Sci. Instrum.* **72**, 3749 (2001).

[20] T. Udem, J. Reichert, R. Holzwarth, and T. W. Hänsch, Accurate measurement of large optical frequency differences with a mode-locked laser, *Opt. Lett.* **24**, 881 (1999).

[21] S. A. Diddams, D. J. Jones, J. Ye, S. T. Cundiff, J. L. Hall, J. K. Ranka, R. S. Windeler, R. Holzwarth, T. Udem, and T. W. Hänsch, Direct Link between Microwave and Optical Frequencies with a 300 THz Femtosecond Laser Comb, *Phys. Rev. Lett.* **84**, 5102 (2000).

[22] S. T. Cundiff and J. Ye, *Colloquium*: Femtosecond optical frequency combs, *Rev. Mod. Phys.* **75**, 325 (2003).

[23] T. Udem, A. Huber, B. Gross, J. Reichert, M. Prevedilli, M. Weitz, and T. W. Hänsch, Phase-Coherent Measurement of the Hydrogen 1S-2S Transition Frequency with an Optical Frequency Interval Divider Chain, *Phys. Rev. Lett.* **79**, 2646 (1997).

[24] T. Udem, J. Reichert, R. Holzwarth, and T. W. Hänsch, Absolute Optical Frequency Measurement of the Cesium D1 Line with a Mode-Locked Laser, *Phys. Rev. Lett.* **82**, 3568 (1999).

[25] S. A. Diddams *et al.*, An Optical Clock Based on a Single Trapped $^{199}Hg^{+}$ Ion, *Science* **293**, 825 (2001).

[26] H. Katori, M. Takamoto, V. G. Pal'chikov, and V. D. Ovsiannikov, Ultrastable Optical Clock with Neutral Atoms in an Engineered Light Shift Trap, *Phys. Rev. Lett.* **91**, 173005 (2003).

[27] A. D. Ludlow *et al.*, Sr Lattice Clock at 1 x $10^{16}$ Fractional Uncertainty by Remote Optical Evaluation with a Ca Clock, *Science* **319**, 1805 (2008).

[28] T. Rosenband *et al.*, Frequency Ratio of $Al^{+}$ and $Hg^{+}$ Single-Ion Optical Clocks; Metrology at the 17th Decimal Place, *Science* **319**, 1808 (2008).

[29] S. Blatt *et al.*, New Limits on Coupling of Fundamental Constants to Gravity Using $^{87}Sr$ Optical Lattice Clocks, *Phys. Rev. Lett.* **100**, 140801 (2008).

[30] J. Ye, Everything under control, *Nat. Photonics* **1**, 447 (2007).

[31] Z. Jiang, C.-B. Huang, D. E. Leiard, and A. M. Weiner, Optical arbitrary waveform processing of more than 100 spectral comb lines, *Nat. Photonics* **1**, 463 (2007).

[32] M. C. Stowe, F. C. Cruz, A. Marina, and J. Ye, High Resolution Atomic Coherent Control via Spectral Phase Manipulation of an Optical Frequency Comb, *Phys. Rev. Lett.* **96**, 153001 (2006).

[33] A. Pe'er, E. A. Shapiro, M. C. Stowe, M. Shapiro, and J. Ye, Precise Control of Molecular Dynamics with a Femtosecond Frequency Comb, *Phys. Rev. Lett.* **98**, 113004 (2007).

[34] M. Hentschel, R. Kienberger, C. Spielmann, G. A. Reider, N. Milosevic, T. Brabec, P. Corkum, U. Heinzmann, M. Drescher, and F. Krausz, Attosecond metrology, *Nature* **414**, 509 (2001).

[35] A. Baltuska, T. Udem, M. Uiberacker, M. Hentschel, E. Goulielmakis, C. Gohle, R. Holzwarth, V. S. Yakovlev, T. W. Scrinzi, A. Hänsch, and F. Kraus, Attosecond control of electronic processes by intense light fields, *Nature* **421**, 611 (2003).

[36] A. Marian, M. C. Stowe, J. R. Lawall, D. Felinto, and J. Ye, United Time-Frequency Spectroscopy for Dynamics and Global Structure, *Science* **306**, 2063 (2004).

[37] M. J. Thorpe, K. D. Moll, R. J. Jones, B. Safdi, and J. Ye, Broadband Cavity Ringdown Spectroscopy for Sensitive and Rapid Molecular Detection, *Science* **311**, 1595 (2006).

[38] S. A. Diddams, L. Hollberg, and V. Mbele, Molecular fingerprinting with the resolved modes of a femtosecond laser frequency comb, *Nature* **445**, 627 (2007).

[39] F. Tauser, A. Leitenstorfer, and W. Zinth, Amplified femtosecond pulses from an Er:fiber system: Nonlinear pulse shortening and self-referencing detection of the carrier-envelope phase evolution, *Opt. Express* **11**, 594 (2003).

[40] J. K. Ranka, R. S. Windeler, and A. J. Stentz, Visible continuum generation in air-silica microstructure optical fibers with anomalous dispersion at 800 nm, *Opt. Lett.* **25**, 25 (2000).

[41] K. W. Jucks, D. G. Johnson, K. V. Chance, W. A. Traub, J. J. Margitan, G. B. Osterman, R. J. Salawitch, and Y. Sasano, Observations of OH, $HO_2$, $H_2O$, and $O_3$ in the upper stratosphere: implications for HOx photochemistry, *Geophys. Res. Lett.* **25**, 3935 (1998).

[42] J. N. Begum, Modeling of chemical tracer transport in the atmospheric environment and its impact on the global climate, *J. Quant. Spectrosc. Radiat. Transfer* **95**, 423 (2005).

[43] K. K. Lehmann, B. H. Pate, and G. Scoles, On the measurement of the rate of intermolecular vibrational energy redistribution via high resolution molecular beam optothermal spectroscopy, *Laser Chem.* **11**, 237 (1991).

[44] J. E. Gambogi, E. R. Th. Kerstel, K. K. Lehmann, and G. Scoles, Eigenstate resolved infrared/infrared double resonance spectroscopy of the $3\nu_1$ overtone band of I-propyne: Intramolecular vibrational energy redistribution into a Coriolis-coupled bath, *J. Chem. Phys.* **100**, 2612 (1994).

[45] H. R. Thorsheim, J. Weiner, and P. S. Julienne, Laser-induced photoassociation of ultracold sodium atoms, *Phys. Rev. Lett.* **58**, 2420 (1987).

[46] E. R. Hudson, C. Ticknor, B. C. Sawyer, C. A. Taatjes, H. J. Lewandowski, J. R. Bochinski, J. L. Bohn, and J. Ye, Production of cold formaldehyde molecules for study and control of chemical reaction dynamics with hydroxyl radicals, *Phys. Rev. A* **73**, 063404 (2006).

[47] J. Doyle, B. Friedrich, R. V. Krems, and F. Masnou-Seeuws, Quo vadis, cold molecules?, *Eur. J. Phys. D.* **31**, 149 (2004).

[48] C. Wang, S. T. Scherer, and D. Hossain, Measurements of Cavity Ringdown Spectroscopy of Acetone in the Ultraviolet and Near-Infrared Spectral Regions: Potential for Development of a Breath Analyzer, *Appl. Spectrosc.* **58**, 784 (2004).

[49] K.-K. Ni, S. Ospelkaus, M. H. G. de Miranda, A. Peer, J. J. Neyenhuis, B. Zirbel, S. Kotochigova, P. S. Julienne, D. S. Jin, and J. Ye, A high phase-space-density gas of ground-state polar molecules, *Science* **322**, 231 (2008).

[50] T. H. Risby and S. F. Solga, Current status of clinical breath analysis, *Appl. Phys. B* **85**, 421 (2006).

[51] H. R. Telle, G. Steinmeyer, A. E. Dunlop, J. Stenger, D. H. Sutter, and U. Keller, Carrier-envelope offset phase control: A novel concept for absolute optical frequency measurement and ultrashort pulse generation, *Appl. Phys. B* **69**, 327 (1999).

[52] T. Udem, R. Holzwarth, and T. W. Hänsch, Optical frequency metrology, *Nature* **416**, 233 (2002).

[53] J. Ye and S. T. Cundiff, *Femtosecond optical frequency comb technology: Principle, operation, and application.* (Springer, New York, 2005).

[54] R. J. Jones and J. C. Diels, Stabilization of Femtosecond Lasers for Optical Frequency Metrology and Direct Optical to Radio Frequency Synthesis, *Phys. Rev. Lett.* **86**, 3288 (2001).

[55] R. J. Jones, I. Thomann, and J. Ye, Precision stabilization of femtosecond lasers to high-finesse optical cavities, *Phys. Rev. A* **69**, 051803 (2004).

[56] S. M. Foreman, D. J. Jones, and J. Ye, Flexible and rapidly configurable femtosecond pulse generation in the mid-IR, *Opt. Lett.* **28**, 370 (2003).

[57] E. Penman, C. McGowan, P. Loza-Alvarez, D. T. Reid, M. Ebrahimzadeh, and W. Sibbett, Femtosecond optical parametric oscillators based on periodically poled lithium niobate, *J. Mod. Opt.* **45**, 1285 (1998).

[58] D. Mazzotti, P. Cancio, G. Giusfredi, P. De Natale, and M. Prevedelli, Frequency-comb-based absolute frequency measurements in the mid-infrared with a difference-frequency spectrometer, *Opt. Lett.* **30**, 997 (2005).

[59] A. Schliesser, M. Brehm, F. Keilmann, and D. W. van der Weide, Frequency-comb infrared spectrometer for rapid, remote chemical sensing, *Opt. Express* **13**, 9029 (2003).

[60] R. J. Jones, K. D. Moll, M. J. Thorpe, and J. Ye, Phase-Coherent Frequency Combs in the Vacuum Ultraviolet via High-Harmonic Generation inside a Femtosecond Enhancement Cavity, *Phys. Rev. Lett.* **94**, 193201 (2005).

[61] C. Gohle, T. Udem, M. Herrmann, J. Rauschenberger, R. Holzwarth, A. Schuessler, F. Kraus, and T. W. Hänsch, A frequency comb in the extreme ultraviolet, *Nature* **436**, 234 (2005).

[62] D. C. Yost, T. R. Schibli, and J. Ye, Efficient output coupling of intracavity high-harmonic generation, *Opt. Lett.* **33**, 1099 (2008).

[63] E. E. Eyler, D. E. Chieda, M. C. Stowe, M. J. Thorpe, T. R. Schibli, and J. Ye, Prospects for precision measurements of atomic helium using direct frequency comb spectroscopy, *Eur. Phys. J. D.* **48**, 1 (2008).

[64] T. A. Birks, W. J. Wadsworth, and P. S. J. Russel, Supercontinuum generation in tapered fibers, *Opt. Lett.* **25**, 1415 (2000).

[65] T. M. Fortier, D. J. Jones, and S. T. Cundiff, Phase stabilization of an octave-spanning Ti:sapphire laser, *Opt. Lett.* **28**, 2198 (2003).

[66] R. Ell *et al.*, Generation of 5-fs pulses and octave-spanning spectra directly from a Ti:sapphire laser, *Opt. Lett.* **26**, 373 (2001).

[67] T. M. Fortier, A. Bartels, and S. A. Diddams, Octave-spanning Ti:sapphire laser with a repetition rate $> 1$ GHz for optical frequency measurements and comparisons, *Opt. Lett.* **31**, 1011 (2006).

[68] L. E. Nelson, D. J. Jones, K. Tamura, H. A. Haus, and E. P. Ippen, Ultrashort-pulse fiber ring lasers, *Appl. Phys. B* **65**, 277 (1997).

[69] P. Pal, W. H. Knox, I. Hartl, and M. E. Fermann, Self referenced Yb-fiber-laser frequency comb using a dispersion micromanaged tapered holey fiber, *Opt. Express* **15**, 12161 (2007).

[70] P. Balling, M. Fischer, P. Kubina, and R. Holzwarth, Absolute frequency measurement of wavelength standard at 1542nm: acetylene stabilized DFB laser, *Opt. Express* **13**, 9196 (2005).

[71] B. R. Washburn, S. A. Diddams, N. R. Newbury, J. W. Nicholson, M. F. Yan, and C. G. Jorgensen, Phase-locked, erbium-fiber-laser-based frequency comb in the near infrared, *Opt. Lett.* **29**, 250 (2004).

[72] T. R. Schibli, D. C. Yost, M. J. Martin, J. Ye, I. Hartl, A. Marcinkevicius, and M. E. Fermann, Optical frequency comb with submillihertz linewidth and more than 10 W average power, *Nat. Photonics* **2**, 355 (2008).

[73] K. Moutzouris, F. Adler, F. Sotier, D. Träutlein, and A. Leitenstorfer, Multimilliwatt ultrashort pulses continuously tunable in the visible from a compact fiber source, *Opt. Lett.* **31**, 1148 (2006).

[74] C. Erny, K. Moutzouris, J. Biegert, D. Kühlke, F. Adler, and A. Leitenstorfer, Mid-infrared difference-frequency generation of ultrashort pulses tunable between 3.2 and 4.8 $\mu$m from a compact fiber source, *Opt. Lett.* **32**, 1138 (2007).

[75] M. J. Thorpe, D. D. Hudson, K. D. Moll, J. Lasri, and J. Ye, Cavity-ringdown molecular spectroscopy based on an optical frequency comb at 1.451.65 $\mu$m, *Opt. Lett.* **32**, 307 (2007).

[76] M. J. Thorpe, D. Balslev-Clausen, M. S. Kirchner, and J. Ye, Cavity-enhanced optical frequency comb spectroscopy: application to human breath analysis, *Opt. Express* **16**, 2387 (2008).

[77] I. Thomann, A. Bartels, K. L. Corwin, N. R. Newbury, L. Hollberg, S. A. Diddams, J. W. Nicholson, and M. F. Yan, 420-MHz Cr:forsterite femtosecond ring laser and continuum generation in the 12 $\mu$m range, *Opt. Lett.* **28**, 1368 (2003).

[78] A. Bartels, N. R. Newbury, I. Thomann, L. Hollberg, and S. A. Diddams, Broadband phase-coherent optical frequency synthesis with actively linked Ti:sapphire and Cr:forsterite femtosecond lasers, *Opt. Lett.* **29**, 403 (2004).

[79] R. C. Sharp, D. E. Spock, N. Pan, and J. Elliot, 190-fs passively mode-locked thulium fiber laser with a low threshold, *Opt. Lett.* **12**, 881 (1996).

[80] S. Kivistö, T. Hakulinen, M. Guina, and O. Okhotnikov, Tunable Raman Soliton Source Using Mode-Locked TmHo Fiber Laser, *IEEE Photon. Technol. Lett.* **19**, 934 (2007).

[81] M. A. Solodyankin, E. D. Obraztsova, A. S. Lobach, A. I. Cherno, A. V. Tausenev, V. I. Konov, and E. M. Dianov, Mode-locked 1.93 $\mu$m thulium fiber laser with a carbon nanotube absorber, *Opt. Lett.* **33**, 1336 (2008).

[82] I. S. Moskalev, V. V. Fedorov, and S. B. Mirov, *Conference on Lasers and Electro-Optics, 2008.* (OSA, San Jose, CA, 2008), pp. 1–2.

[83] E. Sorokin, S. Naumov, and I. T. Sorokina, Ultrabroadband Infrared Solid-State Lasers, *IEEE J. of selected topics in Quantum Electronics* **11**, 690 (2005).

[84] K. Tamura, L. E. Nelson, H. A. Haus, and E. P. Ippen, Soliton versus nonsoliton operation of fiber ring lasers, *Appl. Phys. Lett.* **64**, 149 (1994).

[85] C. R. Giles and E. Desurvire, Modeling Erbium-Doped Fiber Amplifiers, *J. Lightwave Technol.* **9**, 271 (1991).

[86] E. Desurvire, J. R. Simpson, and P. C. Becker, High-gain erbium-doped traveling-wave fiber amplifier, *Opt. Lett.* **12**, 888 (1987).

[87] M. Peroni and M. Tamburrini, Gain in erbium-doped fiber amplifiers: a simple analytical solution for the rate equations, *Opt. Lett.* **15**, 842 (1990).

[88] Miniscalco, Erbium-Doped Glasses for Fiber Amplifiers at 1500 nm, *J. Lightwave Technol.* **9**, 234 (1991).

[89] Thorlabs, http://thorlabs.com.

[90] R. W. Boyd, *Nonlinear optics*, 2 ed. (Academic Press, San Diego, 2003), pp. 1–65.

[91] J. D. Jackson, *Classical electrodynamics*, 3 ed. (Wiley, Hoboken, NJ, 1999), pp. 151–165.

[92] R. W. Boyd, *Nonlinear optics*, 2 ed. (Academic Press, San Diego, 2003), pp. 189–209.

[93] Menlo, http://www.menlosystems.com/.

[94] EM4, http://www.em4inc.com/.

[95] Bookham, http://www.bookham.com/.

[96] J. W. Lou, T. F. Carruthers, and M. Currie, Mode-Locked Multiple-Wavelength Erbium-Doped Fiber Laser in a Sigma Configuration, *IEEE Photon. Technol. Lett.* **14**, 281 (2002).

[97] D. D. Hudson, K. W. Holman, R. J. Jones, S. T. Cundiff, J. Ye, and D. J. Jones, Mode-locked fiber laser frequency-controlled with an intracavity electro-optic modulator, *Opt. Lett.* **30**, 2948 (2005).

[98] G. P. Agrawal, *Nonlinear fiber optics*, 4th ed. (Academic Press, New York, 2007), pp. 162–168.

[99] R. W. Boyd, *Nonlinear optics*, 2 ed. (Academic Press, San Diego, 2003), pp. 356–363.

[100] M. V. Klein and T. E. Furtak, in *Optics*, 2 ed., edited by J. W. Goodman (Wiley, New York, 1986), pp. 295–324.

[101] The work at JILA has greatly benefited from collborative coating runs from R. Lalezari of Advanced Thin Films.

[102] K. K. Lehmann and P. Rabinowitz, High-Finesse Optical Resonator for Cavity Ring-Down Spectroscopy based upon Brewsters Angle Prism Retroreflectors,, U. S. Patent 5973864, 1999.

[103] V. N. Kuryatov and A. L. Sokolov, Polarisation losses in a ring prism cavity, *Quantum Electron.* **30**, 125 (2000).

[104] P. S. Johnston and K. K. Lehmann, Cavity enhanced absorption spectroscopy using a broadband prism cavity and a supercontinuum source, *Opt. Express* **16**, 15013 (2008).

[105] E. Hecht, *Optics*, 4th ed. (Addison-Wesley, New York, 2002), pp. 416–421.

[106] D. Romanini and K. K. Lehmann, Ring-down cavity absorption spectroscopy of the very weak HCN overtone bands with six, seven, and eight stretching quanta, *J. Chem. Phys* **99**, 6287 (1993).

[107] J. Ye and J. L. Hall, Cavity ringdown heterodyne spectroscopy: High sensitivity with microwatt light power, *Phys. Rev. A* **61**, 061802 (2000).

[108] Y. He and B. Orr, Ringdown and cavity-enhanced absorption spectroscopy using a continuous-wave tunable diode laser and a rapidly swept optical cavity, *Chem. Phys. Lett.* **319**, 131 (2000).

[109] A. E. Siegman, in *Lasers*, edited by A. Kelly (University Science Books, Sausalito, Ca, 1986), pp. 573–576.

[110] R. G. DeVoe, C. Fabre, K. Jungmann, J. Hoffnagle, and R. G. Brewer, Precision optical-frequency-difference measurements, *Phys. Rev. A* **37**, 1802 (1988).

[111] C. J. Hood, H. J. Kimble, and J. Ye, Characterization of high-finesse mirrors: Loss, phase shifts, and mode structure in an optical cavity, *Phys. Rev. A* **64**, 033804 (2002).

[112] M. J. Thorpe, R. J. Jones, K. D. Moll, J. Ye, and R. Lalezari, Precise measurements of optical cavity dispersion and mirror coating properties via femtosecond combs, *Opt. Express* **13**, 882 (2005).

[113] A. Schliesser, C. Gohle, T. Udem, and T. W. Hänsch, Complete characterization of a broadband high-finesse cavity using an optical frequency comb, *Opt. Express* **14**, 5975 (2006).

[114] J. Ye, L. S. Ma, and J. L. Hall, Sub-Doppler optical frequency reference at 1.064 mm by means of ultrasensitive cavity-enhanced frequency modulation spectroscopy of a C2HD overtone transition, *Opt. Lett.* **21**, 1000 (1996).

[115] C. S. Gudeman, M. H. Begemann, J. Pfaff, and R. J. Saykally, Velocity-modulated infrared laser spectroscopy of molecular ions: The $\nu_1$ band of $HCO^+$, *Phys. Rev. Lett.* **50**, 727 (1983).

[116] D. J. Nesbitt, H. Petek, C. S. Gudeman, C. B. Moore, and R. J. Saykally, A study of the $\nu_1$ fundamental and bend-excited hot band of $DNN^+$ by velocity modulation absorption spectroscopy with an infrared difference frequency laser, *J. Chem. Phys.* **81**, 5281 (1984).

[117] J. T. Verdeyen, in *Laser Electronics*, 3rd ed., edited by N. J. Holonyak (Prentice Hall, Upper Saddle River, NJ, 1995), pp. 76–136.

[118] A. E. Siegman, in *Lasers*, edited by A. Kelly (University Science Books, Sausalito, Ca, 1986), pp. 786–797.

[119] MATLAB, Genetic Algorithm and Direct Search Toolbox, version R2007b, function name 'ga( )'.

[120] A. E. Siegman, in *Lasers*, edited by A. Kelly (University Science Books, Sausalito, Ca, 1986), pp. 700–770.

[121] T. Gherman and D. Romanini, Mode-locked cavity-enhanced absorption spectroscopy, *Opt. Express* **10**, 1033 (2002).

[122] C. Gohle, B. Stein, A. Schliesser, T. Udem, and T. W. Hänsch, Frequency Comb Vernier Spectroscopy for Broadband, High-Resolution, High-Sensitivity Absorption and Dispersion Spectra, *Phys. Rev. Lett.* **99**, 263902 (2007).

[123] M. J. Thorpe and J. Ye, Cavity-enhanced direct frequency comb spectroscopy, *Appl. Phys. B.* **91**, 397414 (2008).

[124] J. Ye and W. Lynn, Applications of Optical Cavities in Modern Atomic, Molecular, and Optical Physics, *Adv. At. Mol. Opt. Phys.* **49**, 1 (2003).

[125] L. Gianfrani, R. W. Fox, and L. Hollberg, Cavity-enhanced absorption spectroscopy of molecular oxygen, *J. Opt. Soc. Am. B* **16**, 2247 (1999).

[126] L. S. Ma, J. Ye, P. Dube, and J. L. Hall, Ultrasensitive frequency-modulation spectroscopy enhanced by a high-finesse optical cavity: theory and application to overtone transitions of C2H2 and C2HD, *J. Opt. Soc. Am. B* **16**, 2255 (1999).

[127] J. Poirson, F. Bretenaker, M. Vallet, and A. Le Floch, Analytical and experimental study of ringing effects in a Fabry-Perot cavity. Application to the measurement of high finesses, *J. Opt. Soc. Am. B* **14**, 2811 (1997).

[128] R. Bakowski, L. Corner, G. Hancock, R. Kotchie, R. Peverall, and G. A. D. Ritchie, Cavity-enhanced absorption spectroscopy with a rapidly swept diode laser, *Appl. Phys. B* **75**, 745 (2002).

[129] M. D. Levenson, B. A. Paldus, T. G. Spence, C. C. Harb, J. Harris, J. S., and R. N. Zare, Optical heterodyne detection in cavity ring-down spectroscopy, *Chem. Phys Lett.* **290**, 335 (1998).

[130] J. J. Scherer, J. B. Paul, A. O'Keefe, and R. J. Saykally, Cavity Ringdown Laser Absorption Spectroscopy: History, Development, and Application to Pulsed Molecular Beams, *Chem. Rev.* **97**, 25 (1997).

[131] M. V. Klein and T. E. Furtak, in *Optics*, 2 ed., edited by J. W. Goodman (Wiley, New York, 1986), pp. 280–284.

[132] M. V. Klein and T. E. Furtak, in *Optics*, 2 ed., edited by J. W. Goodman (Wiley, New York, 1986), pp. 457–465.

[133] A. M. Weiner, Femtosecond pulse shaping using spatial light modulators, *Rev. Sci. Instrum.* **71**, 1929 (2000).

[134] E. Hecht, *Optics*, 4th ed. (Addison-Wesley, New York, 2002), pp. 471–474.

[135] E. Hecht, *Optics*, 4th ed. (Addison-Wesley, New York, 2002), pp. 476–481.

[136] J. J. Scherer, Ringdown spectral photography, *Chem. Phys. Lett.* **292**, 143 (1998).

[137] J. J. Scherer, J. B. Paul, H. Jiao, and A. OKeefe, Broadband ringdown spectral photography, *Appl. Opt.* **40**, 6725 (2001).

[138] S. Xiao and A. M. Weiner, 2-D wavelength demultiplexer with potential for $\geq$ 1000 channels in the C-band, *Opt. Express* **12**, 2895 (2004).

[139] M. Shirasaki, Large angular dispersion by a virtually imaged phased array and its application to a wavelength demultiplexer, *Opt. Lett.* **21**, 366 (1996).

[140] A. Vega, A. M. Weiner, and C. Lin, Generalized grating equation for virtually-imaged phased-array spectral dispersers, *Appl. Opt.* **42**, 4152 (2003).

[141] S. Xiao, A. M. Weiner, and C. Lin, A Dispersion Law for Virtually Imaged Phased-Array Spectral Dispersers Based on Paraxial Wave Theory, *IEEE J. Quantum Electron.* **40**, 420 (2004).

[142] M. Shirasaki, A. N. Akhter, and C. Lin, Virtually Imaged Phased Array with Graded Reflectivity, *IEEE Photon. Technol. Lett.* **11**, 1443 (1999).

[143] A. Mokhtari and A. A. Shichegar, *Optical Fiber Communication and Optoelectronics Conference, 2007 Asia* (IEEE, Shanghai, 2007), pp. 514–516.

[144] E. R. Crosson, P. Haar, G. A. Marcus, H. A. Schwettman, B. A. Paldus, T. G. Spence, and R. N. Zare, Pulse-stacked cavity ring-down spectroscopy, *Rev. Sci. Instrum.* **70**, 4 (1999).

[145] A. E. Siegman, in *Lasers*, edited by A. Kelly (University Science Books, Sausalito, Ca, 1986), pp. 286–291.

[146] L. S. Rothman *et al.*, The HITRAN 2004 molecular spectroscopic database, *J. Quant. Spectrosc. Radiat. Transfer* **96**, 139 (2005).

[147] L. Lundsberg-Nielsen, F. Hegelund, and F. M. Nicolaisen, Analysis of the High-Resolution Spectrum of Ammonia ($^{14}NH_3$) in the Near-Infrared Region, 6400-6900 $cm^{-1}$, *J. Mol. Spectrosc.* **162**, 230 (1993).

[148] G. Herzberg, *Molecular spectra and Molecular structure*, 2 ed. (Krieger, Malabar, Florida, 1950), Vol. I, pp. 122–129.

[149] E. R. Crosson *et al.*, Stable Isotope Ratios Using Cavity Ring-Down Spectroscopy: Determination of $^{13}C/^{12}C$ for Carbon Dioxide in Human Breath, *Anal. Chem.* **74**, 2003 (2002).

[150] L. N. Plummer, E. Busenber, J. K. Bohlke, D. L. Nelms, R. L. Michel, and P. Schlosser, Groundwater residence times in Shenandoah National Park, *Chem. Geol.* **179**, 93 (2001).

[151] E. Mosely-Thompson, L. G. Thompson, and P. N. Lin, A multi-century ice-core perspective on 20th-century climate change with new contributions from high-Arctic and Greenland (PARCA) cores, *Ann. Glaciology* **43**, 42 (2006).

[152] W. Q. Cao and Y. X. Duan, Breath analysis: Potential for Clinical Diagnosis and Exposure Assessment, *Clin. Chem.* **52**, 800 (2006).

[153] S. Dill, J. J. Payne-James, J. J. Misiewicz, G. K. Grimble, K. McSwiggan, K. Pathak, A. J. Wood, C. M. Scrimgeour, and M. J. Rennie, Evaluation of $^{13}C$-urea breath test in the detection of Heliobacter pylori and in monitoring the effect of tripotassium dicitratobismuthate in non-ulcer dyspepsia, *Gut.* **31**, 1237 (1990).

[154] F. Di Francesco, R. Fuoco, M. G. Trivella, and A. Ceccarini, Breath analysis: trends in techniques and clinical applications, *Microchem. J.* **79**, 405 (2005).

[155] R. F. Machado *et al.*, Detection of Lung Cancer by Sensor Array Analyses of Exhaled Breath, *Am. J. Respir. Crit. Care Med.* **171**, 1286 (2005).

[156] W. L. Wood, D. J. Higbee, M. Gooldy, S. Glogowski, R. Fitzpatrick, R. J. Karalus, T. D. Wood, and D. J. Mangino, Analysis of Volatile Metabolites by Gas Chromatography-Mass Spectrometry, *Spectroscopy* **21**, 20 (2006).

[157] R. Polikar, R. Shinar, V. Honavar, L. Udpa, and M. D. Porter, Detection and Identification of Odorants Using an Electronic Nose, *in Proceedings of IEEE 26th International Conference Acoustics, Speech and Signal Processing* **5**, 3137 (2001).

[158] J. Ye, L. S. Ma, and J. L. Hall, Ultrasensitive detections in atomic and molecular physics: demonstration in molecular overtone spectroscopy, *J. Opt. Soc. Am. B* **15**, 6 (1998).

[159] P. D. Klein and D. Y. Graham, Minimum analysis requirements for the detection of Helicobacter pylori infection by the 13C-urea breath test, *Am. J. Gastroenterol.* **88**, 1865 (1993).

[160] A. J. Cunnington and P. Hombrey, Breath analysis to detect recent exposure to carbon monoxide, *Postgrad. Med. J.* **78**, 233 (2002).

[161] J. Manne, O. Sukhorukov, W. Jäger, and J. Tulip, Pulsed quantum cascade laser-based cavity ring-down spectroscopy for ammonia detection in breath, *Appl. Opt.* **45**, 9230 (2006).

[162] D. Marinoy, J. M. Rey, M. G. Muller, and M. W. Sigrist, Spectroscopic investigation of methylated amines by a cavity-ringdown-based spectrometer, *Appl. Opt.* **46**, 3981 (2007).

[163] A. André, D. Demille, J. Doyle, M. D. Lukin, S. E. Maxwell, P. Rabl, R. J. Schoelkopf, and P. Zoller, A coherent all-electrical interface between polar molecules and mesoscopic superconducting resonators, *Nat. Phys.* **2**, 636 (2006).

[164] B. C. Sawyer, B. L. Lev, E. R. Hudson, B. K. Stuhl, M. Lara, J. L. Bohn, and J. Ye, Magneto-electrostatic trapping of ground state OH molecules, *Phys. Rev. Lett.* **98**, 253002 (2007).

[165] S. Y. T. Van De Meerakker, H. L. Bethlem, and G. Meijer, Taming molecular beams, *Nat. Phys.* **4**, 595 (2008).

[166] J. G. Danzl, E. Haller, M. Gustavsson, M. J. Mark, R. Hart, N. Bouloufa, O. Dulieu, H. Ritch, and H.-C. Nägerl, Quantum gas of deeply bound ground state molecules, *Science* **321**, 1062 (2008).

[167] M. Viteau, A. Chotia, M. Allegrini, N. Bouloufa, O. Dulieu, D. Comparat, and P. Pillet, Optical Pumping and Vibrational Cooling of Molecules, *Science* **321**, 232 (2008).

[168] W. Salzmann *et al.*, Coherent Transients in the Femtosecond Photoassociation of Ultracold Molecules, *Phys. Rev. Lett.* **100**, 233003 (2008).

[169] E. A. Shapiro, A. Pe'er, J. Ye, and M. Shapiro, Piecewise Adiabatic Population Transfer in a Molecule via aWave Packet, *Phys. Rev. Lett.* **101**, 023601 (2008).

[170] G. Tejeda, B. Maté, J. M. Fernández-Sánchez, and S. Montero, Temperature and Density Mapping of Supersonic Jet Expansions Using Linear Raman Spectroscopy, *Phys. Rev. Lett.* **76**, 34 (1996).

[171] K. Didriche, C. Lauzin, P. Macko, W. J. Lafferty, R. J. Saykally, and M. Herman, On the role of clustering in an acetylene supersonic expansion, *Chem. Phys. Lett.* **463**, 345 (2007).

[172] M. Herman, K. Didriche, D. Hurtmans, B. Kizil, P. Macko, A. Rizopoulos, and P. Van Poucke, FANTASIO: a versatile experimental set-up to investigate jet-cooled molecules, *Mol. Phys.* **105**, 815 (2007).

[173] R. N. Brancewell, *Fourier transform and it's applications*, 3 ed. (McGraw-Hill, New York, 2000), pp. 351–358.

[174] A. A. Madej, A. L. Alcock, A. Czajkowski, J. E. Bernard, and S. Chepurov, Accurate absolute reference frequencies from 1511 to 1545 nm of the $\nu_1+\nu_3$ band of $^{12}C_2H_2$ determined with laser frequency comb interval measurements, *J. Opt. Soc. Am. B.* **23**, 2200 (2006).

[175] J. L. Hall, M. S. Taubman, and J. Ye, in *Handbook of Optics IV*, edited by M. Bass, J. M. Enoch, E. Van Stryland, and W. L. Wolfe (McGraw-Hill, New York, 2000).

[176] U. Valbusa, Atomic and Molecular Beam Methods, *Atomic and Molecular Beam Methods* **1**, 443 (1988).

[177] S. R. Deans, *The Radon Transform and Some of Its Applications* (Wiley, New York, 1983).

[178] E. W. Hansen and A. Jablokow, State Variable Representation of a Class of Linear Shift-Variant Systems, *IEEE. Trans. Acous. Speech Sig. Proc.* **30**, 874 (1982).

[179] G. Herzberg, *Molecular spectra and Molecular structure* (Krieger, Malabar, Florida, 1945), Vol. II, pp. 18, 382.

[180] D. R. Miller, Atomic and Molecular Beam Methods, *Atomic and Molecular Beam Methods* **1**, 14 (1988).

[181] W. R. Gentry, Atomic and Molecular Beam Methods, *Atomic and Molecular Beam Methods* **1**, 70 (1988).

[182] M. D. Duncan, P. Osterlin, and R. L. Byer, Pulsed supersonic molecular-beam coherent anti-Stokes Raman spectroscopy of $C_2H_2$, *Opt. Lett.* **6**, 90 (1981).

[183] M. C. Stowe, A. Pe'er, and J. Ye, Control of Four-Level Quantum Coherence via Discrete Spectral Shaping of an Optical Frequency Comb, *Phys. Rev. Lett.* **100**, 203001 (2008).

# Appendix A

## MATLAB genetic algorithm code for mode-matching

The following MATLAB code uses a genetic algorithm to find a suitable two lens telescope for mode-matching a laser beam having q-parameter (ql) at location (zl) to a cavity with eigenmode q-parameter (qc) at location (zc). For simplicity, this notebook assumes that both ql and qc correspond to a beam waist and are therefore purely imaginary quantities. Note, all distances are expressed in millimeters. The output vector (x) specifies the focal lengths and positions of the telescope lenses with respect to the position of the laser beam waist according to x = [f1 f2 z1 z2]. For best performance, use a high resolution discretization of the lens positions (i.e. $\leq 100$ $\mu$m steps) and no more than 5 cm steps for the focal length discretization. Since this is a genetic algorithm, it does not arrive at the same answer each time you run the program. Therefore, it can be useful to run the program several times in hopes of finding a telescope that can be made from lenses that you already have in the lab. If increased precision of (x) is desired, the population size and number of generations for the genetic algorithm can be increased. The precision of the telescope (x) for matching the laser beam mode to the cavity mode is given by output variable (fval).

```
%------------Input parameters------------%
ql = 200;     %Rayleigh range of laser beam waist
```

```
zl = 0;       %location of laser beam waist
qc = 500;     %Rayleigh range of cavity focus
zc = 2000;    %location of cavity beam waist
%If coupling to the cavity through a curved mirror, set flag == 1, and
%specify input mirror location and radius of curvature.  Otherwise,
%set flag == 0.
flag = 0;
Rm = 0;          %Radius of curvature of the input mirror
nm = 1.5;        %Index of refraction of input mirror
fm = -Rm/(nm-1); %transmission focal length of input mirror
zm = 1700;       %location of the input mirror
zmin = 300;      %minimum z-value where a lens can be positioned
zmax = 1600;     %maximum z-value where a lens can be positioned
fmax = 2000;     %maximum available focal length
fmin = 100;      %minimum available focal length
pd = 10;         %position discretization (10 = 100um, 1 = 1mm, etc.)
fd = 0.02;       %available focal length discetization
              %(0.1 = 1 cm, 0.02 = 5cm, etc.)
%--------Define input vectors for search algorithm-----------%
Z = [zl zc zm zmin zmax fm]*pd; % Vector of locations
q = [ql qc];     % Vector of q-parametes and input mirror ROC
dv = [fd fd pd pd];    % Discretization vector
%--------Use genetic algorithm to find f1, f2, z1, z2---------%
%Set intital population bounds
NumVar = 4;      %Number of variables for the genetic algorithm
LB = [fmin*fd fmin*fd Z(4) Z(4)];   %Bounds on lens focal lengths and locations
UB = [fmax*fd fmax*fd Z(5) Z(5)];
```

```
IniValBounds = [LB; UB];
A = [0 0 1 -1];              %Constraint requiring lens 2 be located
b = 0;                       %after lens 1 (i.e. zl2 > zl1)
% Execute the Genetic algorithm
FitnessFunction = @(x) fitFunction(x,q,Z,dv,flag);
options = gaoptimset('CreationFcn', @int_pop,'MutationFcn',...
 @int_mutation, 'Generations',500,'PopulationSize',250,'TolFun',1e-2,...
'PopInitRange',IniValBounds,'CrossoverFraction',.8,'EliteCount',7);
[x fval] = ga(FitnessFunction, NumVar, options);
x = x./dv;
x      % focal lengths and locations for telescope lenses [f1 f2 z1 z2]
fval   %value of the fitness function at x
```

The fitness function used by the genetic algorithm is given below.

```
function scores = fitFunction(x,q,Z,dv,flag)
if flag == 1
    Mc = [[1 0]' [(Z(2)-Z(3))/dv(3) 1]']*[[1 -dv(3)/Z(5)]' [0 1]']*...
    [[1 0]' [(Z(3)-x(4))/dv(3) 1]']*[[1 -dv(2)/x(2)]' [0 1]']*...
    [[1 0]' [(x(4)-x(3))/dv(3) 1]']*[[1 -dv(2)/x(1)]' [0 1]']*...
    [[1 0]' [(x(3)-Z(1))/dv(3) 1]'];
else
    Mc = [[1 0]' [(Z(2)-x(4))/dv(3) 1]']*[[1 -dv(2)/x(2)]' [0 1]']*...
    [[1 0]' [(x(4)-x(3))/dv(3) 1]']*[[1 -dv(2)/x(1)]' [0 1]']*...
    [[1 0]' [(x(3)-Z(1))/dv(3) 1]'];
end
    AA = Mc(1,1);
```

```
    BB = Mc(1,2);
    CC = Mc(2,1);
    DD = Mc(2,2);
qprop = (AA*1i*q(1)+BB)/(CC*1i*q(1)+DD);
if x(3) > x(4)
    scores = 100*((real(qprop-1i*q(2)))^2+imag(qprop-1i*q(2))^2)^(1/2);
else
    scores = ((real(qprop-1i*q(2)))^2+imag(qprop-1i*q(2))^2)^(1/2);
end
```

The functions that define the populations and mutations of the populations used in the genetic algorithm are written such that the vector variable (x) is an element of a discrete rather than continuous number set. The benefit of this approach is that the answers given for the lens focal lengths correspond to values that can be purchased from actual companies like Thorlabs. The functions that define the populations and mutations based on integer variables are given below.

```
function Population = int_pop(GenomeLength,FitnessFcn,options)

totalpopulation = sum(options.PopulationSize);
range = options.PopInitRange;
lower= range(1,:);
span = range(2,:) - lower;
% The use of ROUND function will make sure that individuals are integers.
Population = round(repmat(lower,totalpopulation,1) +  ...
    repmat(span,totalpopulation,1) .* rand(totalpopulation,GenomeLength));
% End of creation function
```

```
% Mutation function to generate children satisfying the range and integer
% constraints on decision variables.
function mutationChildren = int_mutation(parents,options,GenomeLength, ...
    FitnessFcn,state,thisScore,thisPopulation)
shrink = .01;
scale = 1;
scale = scale - shrink * scale * state.Generation/options.Generations;
range = options.PopInitRange;
lower = range(1,:);
upper = range(2,:);
scale = scale * (upper - lower);
mutationPop =  length(parents);
% The use of ROUND function will make sure that children are integers.
mutationChildren =  round(repmat(lower,mutationPop,1) +  ...
    repmat(scale,mutationPop,1) .* rand(mutationPop,GenomeLength));
% End of mutation function
```

All of these functions should be saved a separate m-files with names that are identical to their function names. For instance, the population generation function should be named int_pop.m. Finally, all files should be saved in the same folder so that they can be found by MATLAB when you run the genetic algorithm. Good luck!

# Appendix B

## Derivation of the cavity ringdown and cavity enhanced absorption equations

### B.1 Cavity ringdown spectroscopy derivation

Begin with a two mirror cavity with length L, mirror reflectivity R, intra-cavity power $P_o$. Let the cavity contain a uniformly distributed and frequency dependent intra-cavity absorber $\alpha(\omega)$. The time rate of change of power inside this cavity can be written as

$$\frac{dP(\omega)}{dt} = -P_o \frac{c}{2L}(1 - R^2 e^{-2\alpha(\omega)L}). \tag{B.1}$$

This rate equation can be integrated to yield the power in the cavity as a function of time.

$$P(\omega, t) = P_o e^{(-\frac{t}{\tau(\omega)})} + C \tag{B.2}$$

where the decay constant $\tau$ takes the form

$$\tau(\omega) = \frac{2L}{c(1 - R^2 e^{-2\alpha(\omega)L})} = \frac{1}{FSR(1 - R^2 e^{-2\alpha(\omega)L})}. \tag{B.3}$$

In the low absorption limit, where the approximation $e^{-2\alpha(\omega)L} \approx (1 - 2\alpha L)$ is valid, the change in the ringdown due to absorption is

$$\frac{\delta\tau(\omega)}{\tau(\omega)} = 1 - \frac{1 - R^2}{(1 - R^2(1 - 2\alpha(\omega)L))} = 1 - \frac{1}{1 + \frac{2\alpha(\omega)L}{1-R^2}}. \tag{B.4}$$

We can then Taylor expand this result for the case of $2\alpha(\omega)L \ll 1 - R^2$ which gives

$$\frac{\delta\tau(\omega)}{\tau(\omega)} \approx \frac{2\alpha(\omega)L}{1-R^2}. \tag{B.5}$$

Finally, we use the approximations $1 - R^2 \approx 2(1 - R)$ and $\mathcal{F} \approx \pi/(1 - R)$ to arrive at the final result

$$\frac{\delta\tau(\omega)}{\tau(\omega)} \approx \frac{\mathcal{F}\alpha(\omega)L}{\pi}. \tag{B.6}$$

Equation B.6 shows the enhancement of the intra-cavity absorption signal provided by cavity ringdown spectroscopy in the low absorption limit.

## B.2 Steady-state cavity enhanced absorption spectroscopy derivation

Once again we'll begin with a two mirror cavity of length L with mirror transmission $T = |t|^2$ and reflectivity $R = |r|^2$, where $t$ and $r$ are the electric field transmission and reflectivity coefficients. However, this time there will initially be no intra-cavity power. Instead, we imagine a Gaussian beam that is perfectly mode-matched to the cavity mode incident on one of the cavity mirrors. Let this beam have electric field amplitude $E_o$ and propagation vector $\vec{k}$. As before, let the cavity contain a uniformly distributed and frequency dependent intra-cavity absorber $\alpha(\omega)$ with electric field absorption coefficient $\kappa = \frac{\alpha}{2}$. At the instant that the incident field is turned on, a portion of the field is coupled into the cavity. After each round trip that the Gaussian beam makes inside the intra-cavity electric field is given by

$$\begin{aligned}
E_0 &= tE_o \\
E_1 &= tE_o + tr^2E_oe^{2L(i|\vec{k}|-\kappa)} \\
E_2 &= tE_o + tr^2E_oe^{2L(i|\vec{k}|-\kappa)} + tr^4E_oe^{4L(i|\vec{k}|-\kappa)} \\
E_n &= tE_o + tr^2E_oe^{2L(i|\vec{k}|-\kappa)} + \ldots + tr^{2n}E_oe^{2nL(i|\vec{k}|-\kappa)}.
\end{aligned}$$

Note that though we have not included any phase terms associated with the cavity mirrors it is easy to add a wavelength dependent phase to the mirror reflectivity if necessary. The steady state intracavity field is found by letting $n \to \infty$.

$$E_i = tE_o \sum_{n=0}^{\infty} r^{2n} e^{2nL(i|\vec{k}|-\kappa)} = \frac{tE_o}{1 - r^2 e^{2L(i|\vec{k}|-\kappa)}} \tag{B.7}$$

From Eq. B.7 it is easy to calculate the cavity transmitted field.

$$E_t = \frac{t^2 E_o e^{L(i|\vec{k}|-\kappa)}}{1 - r^2 e^{2L(i|\vec{k}|-\kappa)}} \tag{B.8}$$

The intracavity absorption will be detected by measuring the cavity transmitted intensity

$$I_t = \frac{T^2 I_o e^{\alpha(\omega)L}}{\left|1 - Re^{(2i|\vec{k}|L - \alpha(\omega)L)}\right|^2}. \tag{B.9}$$

For the remainder of this derivation, we'll assume that the incident electric field is resonant with the cavity such that the phase factor in the denominator of the Eq. B.9 is a multiple of $2\pi$.

$$I_t = \frac{T^2 I_o e^{\alpha(\omega)L}}{\left|1 - Re^{-\alpha(\omega)L}\right|^2}. \tag{B.10}$$

The change in cavity transmitted intensity due to absorption in the low absorption limit ($2\alpha L \ll 1 - R$) is

$$\frac{\delta I_t}{I_t} = 1 - \frac{1 - \alpha(\omega)L}{\left|1 + \frac{\alpha(\omega)LR}{1-R}\right|^2} \approx 1 - \left(1 - \frac{2\alpha(\omega)L}{1-R}\right). \tag{B.11}$$

$$\frac{\delta I}{I_t} \approx \frac{2\mathcal{F}\alpha(\omega)L}{\pi}. \tag{B.12}$$

Equation B.12 shows that in the low absorption limit, steady-state cavity-enhanced absorption spectroscopy provides twice the signal enhancement compared to cavity ringdown spectroscopy.

## B.3 Transient cavity-enhanced absorption spectroscopy derivation

The transient CEAS derivation is carried out using the same procedure as in the steady-state case with the exception that the for the transient case, a linear frequency sweep is applied to the incident laser frequency. The time-dependent frequency of one of the frequency comb teeth is given by

$$\nu(t) = \nu_o + \beta t. \tag{B.13}$$

The time variable in this equation can be discretized according to the cavity round-trip time such that

$$\nu(t_n) = \nu_o + 2n\beta\frac{L}{c}. \tag{B.14}$$

Using this definition for the frequency of the incident beam, the intra-cavity electric field measured at the output coupler after $n$ round-trips is given by

$$\begin{aligned} E_{out}(t_n) = t^2 E_o e^{2\pi i \nu(t_n)\frac{L}{c}} e^{-\frac{\alpha L}{2}} + \\ t^2 r^2 E_o e^{2\pi i(\nu(t_n) - 2\beta\frac{L}{c})\frac{3L}{c}} e^{-\frac{3\alpha L}{2}} + \\ t^2 r^4 E_o e^{2\pi i(\nu(t_n) - 4\beta\frac{L}{c})\frac{5L}{c}} e^{-\frac{5\alpha L}{2}} + \ldots \\ + t^2 r^{2n} E_o e^{2\pi i(\nu(t_n) - 2(n-1)\beta\frac{L}{c})\frac{(2n-1)L}{c}} e^{-\frac{(2n-1)\alpha L}{2}}. \end{aligned}$$

Here, the variable $t$ in $\nu(t)$ is defined as the time at the moment that the measurement is made. Once again, we let $n \to \infty$ the and sum the geometric series. Also, we note that since the cavity transmitted field is the one that will be measured, each term in the geometric sum has been multiplied by a factor of $e^{2\pi i\beta\frac{L}{c}}$. The resulting expression for the cavity transmitted field is

$$E_t = TE_o \sum_{n=1}^{n_f} R^{n-1} e^{-(2n-1)\alpha\frac{L}{2}} e^{2\pi i\phi(t_{n_f})}, \tag{B.15}$$

where the phase term is given by

$$\phi(t_{n_f}) = (2n-1)(\nu(t_{n_f})\frac{L}{c} - 2(n-1)\beta\frac{L^2}{c^2}). \tag{B.16}$$

Unfortunately, the complexity of the arguments of the exponentials in the Eq. B.15 make direct summation of this expression impossible. Instead, this sum can be carried out numerically to reveal that the enhancement of absorption signals for transient CEAS depends on the sweep speed $\beta$ and the cavity linewidth $\Delta\nu$ as shown in Fig.5.1.

# Appendix C

## Algorithm for finding the fringes in a VIPA interference image

The following MATLAB function locates the fringe pattern on a VIPA interference image, and converts intensity of each fringe into a column vector to create a matrix that contains the normalized change in cavity transmitted intensity at each frequency. This matrix has dimensions $n \times m$, where $n$ is the number of pixels in the vertical direction along the detector array, and $n$ is the number of fringes. After this step, the reference and absorption intensity matrices are combined according to $(I_{ref} - I_{abs})/I_{ref}$ and then unwrapped yielding a traditional 1D absorption spectrum. The low-pass filtering and background subtraction routines in this code are used to improve the accuracy of the absorption measurements extracted from the VIPA images and reduce the noise contained in the resulting spectrum. Care must be taken when setting the parameters for these routines such that absorption information is not 'subtracted' from or 'filtered' out of the absorption spectrum.

```
function collectFringesCM
%----- input from LabVIEW ------%
global pic;           %Absorption picture (pic)
global bckg;          %Reference picture  (bckg)
global freqCut;       %LowPass filter frequency
```

```
global thresh;        %Threshold for fringe finder
global ba;            %Ratio of ref to abs image intensities
global reflambda;     %Wavelenght at bottom left of
                      %VIPA image
%----- output to LabVIEW -----%
global out;

% Find baseline intensity of the (bckg) and (pic) images using a
%'min_finder' algorithm.
baseline = bckg;
bckgSize = size(bckg);
number_of_iterations=100;
ssize = length(baseline(:));
temp1 = baseline(:);
temp2 = baseline(:);
for k = 1:number_of_iterations
    for l = (1+k):(ssize-k)
        temp2(l) = min(temp1(l),(temp1(l+k)+temp1(l-k))/2);
    end
    temp1 = temp2;
end
baseline = reshape(temp1,bckgSize);

baseline1 = pic;
picSize = size(pic);
number_of_iterations=100;
ssize = length(baseline1(:));
```

```
temp1 = baseline1(:);
temp2 = baseline1(:);
for k = 1:number_of_iterations
    for l = (1+k):(ssize-k)
        temp2(l) = min(temp1(l),(temp1(l+k)+temp1(l-k))/2);
    end
    temp1 = temp2;
end
baseline1 = reshape(temp1,picSize);

%This routine determines the number of fringes and their locations. It
%collects the (bckg) and (pic) fringes into column vectors.  Note that
%iidx will automaticly become the second minimum.
rmax = size(pic,1);
rmid = floor(rmax/2);
fringeProfile =  sum(Ref((rmid-5):(rmid+5),:),1)/11;
if istest, plot(fringeProfile),pause;close; end
fringeDiff = fringeProfile - thresh;
poss = find(fringeDiff >= 0);
idx = 1;
fringeN = 1;
while idx < length(poss)-10
    for k = 1:2
        while poss(idx)+1 == poss(idx+1)
            idx = idx + 1;
        end
        idx = idx + 1;
```

```
    if k == 1; iidx = poss(idx); oldidx = idx; end
end
fidx = poss(idx-1);
[maxI,midx] = max(Ref(129, iidx:fidx));
w = floor((fidx-iidx)/3);
midx = iidx + midx+1;
for ridx = 129:256;
    [maxI,midx] = max(Ref(ridx, (midx-w):(midx+w)));
    midx = iidx + midx+1;
    picBasev(ridx,fringeN) = sum(baseline1(ridx, ...
        (midx-w):(midx+w)),2)/(2*w+1);
    bckgv(ridx,fringeN) = sum(bckg(ridx, ...
        (midx-w):(midx+w)),2)/(2*w+1);
    picv(ridx,fringeN) = sum(pic(ridx, ...
        (midx-w):(midx+w)),2)/(2*w+1);
    bckgBasev(ridx,fringeN) = sum(baseline(ridx, ...
        (midx-w):(midx+w)),2)/(2*w+1);
end
[maxI,midx] = max(Ref(128,iidx:fidx));
midx = iidx + midx+1;
for ridx = 128:-1:1;
    [maxI,midx] = max(Ref(ridx, (midx-w):(midx+w)));
    midx = iidx + midx+1;
    picBasev(ridx,fringeN) = sum(baseline1(ridx, ...
        (midx-w):(midx+w)),2)/(2*w+1);
    bckgv(ridx,fringeN) = sum(bckg(ridx, ...
        (midx-w):(midx+w)),2)/(2*w+1);
```

```
        picv(ridx,fringeN) = sum(pic(ridx, ...
            (midx-w):(midx+w)),2)/(2*w+1);
        bckgBasev(ridx,fringeN) = sum(baseline(ridx, ...
            (midx-w):(midx+w)),2)/(2*w+1);
    end
    fringeN = fringeN + 1;
    idx = oldidx;
end

%Lowpass filter picv, bckgv and basev before calculating the normalized
%changes in the cavity transmitted light due to absorption.
fringeSize=size(picv);
[b,a]=butter(2,freqCut);
butter_pic=filtfilt(b,a,picv(:));
butter_bckg=filtfilt(b,a,bckgv(:));
butter_picBasev=filtfilt(b,a,picBasev(:));
butter_bckgBasev=filtfilt(b,a,bckgBasev(:));
picv = reshape(butter_pic,fringeSize);
bckgv = reshape(butter_bckg,fringeSize);
pBasev = reshape(butter_picBasev,fringeSize);
bBasev = reshape(butter_bckgBasev,fringeSize);

%Calculate the normalized change in cavity transmission due to
%absorption at all points along the fringes of the VIPA image.
fringes = (bckgv-picv/ba)./(bckgv-bBasev);
fringes = fringes(:,end:-1:1);
```

```
%Find values closest to zero near top and bottom of adjacent fringes
%and connects them with a straight line.  This step is in preparation
%the background subtraction that occurs in the next code block.
for index = 2:fringeN-1
      aFringes = abs(fringes);
      [minTop,indTop] = min(aFringes(10:40,index-1));
      [minBot,indBot] = min(aFringes(216:246,index));
      iTop = 10+indTop;
      iBot = 210+indBot;
      deltaI = (256-210+indBot)+(10+indTop);
      deltaV = fringes(iTop,index-1)-fringes(iBot,index);
      fringes(iBot:256,index) = fringes(iBot,index)+...
          deltaV/deltaI*(1:(256-iBot+1));
      fringes(iTop:-1:1,index-1) = fringes(iTop,index-1)...
          -deltaV/deltaI*(1:(iTop));
end

% Remove non-zero relative intensity baselines that arise from
%differences in the reference and absorption images intensities.
%This should only be done for spectra containing only sharp
%absorption features.
fringeSize = size(fringes);
for n = 1:fringeN-1
    spectrum = fringes(:,n);
    number_of_iterations=19;
    ssize = length(spectrum(:));
    temp1 = spectrum(:);
```

```
    temp2 = spectrum(:);
    for k = 1:number_of_iterations
        for l = (1+k):(ssize-k)
            temp2(l) = min(temp1(l),(temp1(l+k)+temp1(l-k))/2);
        end
        temp1 = temp2;
    end
    fringes(:,n) = spectrum(:)-temp1(:);
end

%Reshape the normalized changes in cavity transmission array and write
%this array to the output variable.
[fringeL,fringeN] = size(fringes);
out = fringes(fringeL:-1:1,:);
```

# Appendix D

## MATLAB code for a discrete inverse Abel transform

The following MATLAB function calculates the inverse Abel transform for a data vector '$V$'. Each value of the vector is the line-integral of a density distribution measured at different distances '$y$' from the axis of the radial distribution. The distance interval between adjacent line-integral measurements is '$dy$'. This algorithm was taken from Ref. [178].

```
function out = AbelTransform(V, dy)
%--------------Initialize the variables-----------------%
la = length[V];
gPrime = zeros(1,la-1);
xk = zeros(9,la);
f = zeros(1,la);
%----------Compute spatial derivatives of input Matrix-----------%
    gPrime(1,:) = diff(V(1,:))/dy;
%------EigenVectors for computing the inverse Abel transform-------%
h = [.318 .19 .35 .82 1.8 3.9 8.3 19.6 48.3];
lam = [0 -2.1 -6.2 -22.4 -92.5 -414.5 -1889.4 -8990.9 -47391.1];
C = [1 1 1 1 1 1 1 1 1];
%-----------Execute the inverse Abel transform alogorithm----------%
```

```
for j = la-1:-1:2
    Phi(1,:) = (j/(j-1)).^lam(1,:);
    Gamma(1,1) = h(1,1)*(-log(j/(j-1)));
    Gamma(1,2:9) = h(1,2:9)./lam(1,2:9).*(1-(j/(j-1)).^lam(1,2:9));
    for i = 1:9
        a(1,i) = Phi(1,i).*xk(i,j);
    end
    xk(:,j-1) = a(1,:) + Gamma(1,:)*gPrime(1,j);
    f(1,j-1) = dot(C,xk(:,j-1));
    end
end
out = f;
```